

Dissertation  
submitted to the  
Combined Faculties for Natural Sciences and Mathematics  
of the Ruperto-Carola University of Heidelberg, Germany  
for the Degree of  
Doctor of Natural Sciences

presented by  
MSc Physics Nataliya Rebrova  
born in Gelendzhik, Russia  
Oral examination: May 28th, 2014



# Development of a non-depolarizing neutron guide for PERC

Referees:

Priv. Doz. Dr. Ulrich Schmidt  
Prof. Dr. Norbert Herrmann

## Abstract

The cold neutron beam station PERC (Proton Electron Radiation Channel) [1] is developed for measurements of angular correlation coefficients in  $\beta$ -decay of free polarized neutrons with a precision of  $10^{-4}$ . Inside PERC the neutron beam is confined laterally by the guide equipped with a supermirror. The neutron guide within PERC (where the “active decay volume” lies) has to be non-depolarizing at the same precision level of  $10^{-4}$ . The depolarization may take place during reflection of neutrons from the guide walls with supermirror magnetic coatings placed in a strong magnetic field. In this thesis the feasibility of using supermirrors based on diamagnetic Cu and paramagnetic Ti instead of the traditionally used non-ferromagnetic Ni(Mo) or Ni(V) alloys and Ti is investigated. Development and production of the Cu/Ti supermirror coating are performed at Heidelberg University and described in this thesis.

The first depolarization test of the Cu/Ti multilayer covering,  $m=1.2$ , was done at the reflectometer of polarized neutrons at a reactor of the Institute Laue-Langevin, France. The reflectometer was based on the Opaque Test Bench [2], a tool for investigation neutron depolarization with high accuracy. The second depolarization test of the Cu/Ti multilayer samples,  $m=1.55$  and  $m=1.7$ , and Ni(Mo)/Ti sample,  $m=1.5$ , was performed at the research reactor Munich II, Germany. The special reflectometer of polarized neutrons was built and optimized for the measurement of small neutron depolarization. The accuracy of this measurement was limited to  $5 \cdot 10^{-3}$  at the region of our interest. We suffer from the neutron depolarization caused by the specificity of used polarizer and analyzer in geometry of the experiment. No depolarization effect was observed in both experiments at the level of precision of the measurements.

## Kurzfassung

Das Instrument PERC (Proton Electron Radiation Channel) [1] wurde entwickelt, um in Messungen die Winkel-Korrelations-Koeffizienten des  $\beta$ -Zerfalls von kalten freien polarisierten Neutronen mit einer Präzision von  $10^{-4}$  zu bestimmen. In PERC wird der Neutronenstrahl lateral durch einen Leiter begrenzt, der mit Superspiegeln beschichtet ist. Damit diese Genauigkeit erreicht werden kann, darf der Neutronenleiter die Polarisation der Neutronen auf demselben Niveau von  $10^{-4}$  nicht ändern. Eine solche Depolarisation könnte durch Reflexion der Neutronen an magnetischen Superspiegelschichten in einem starken Magnetfeld verursacht werden. Im Rahmen dieser Arbeit wurde die Anwendbarkeit von Superspiegeln, die aus diamagnetischem Kupfer (Cu) und paramagnetischem Titan (Ti) anstelle von herkömmlichen nicht ferromagnetischen Ni(Mo) oder Ni(V) Legierungen und Titan bestehen, untersucht. An der Universität Heidelberg wurden die Cu/Ti Superspiegelbeschichtungen entwickelt und produziert. Der erste Depolarisationstest an Cu/Ti,  $m=1.2$  Vielschichten wurde mithilfe eines Reflektometers am Institut Laue-Langevin in Frankreich durchgeführt. Diese "Opaque Test Bench" ist ein Instrument, um die Depolarisation von Neutronen mit hoher Genauigkeit zu analysieren [2]. Der zweite Test an Cu/Ti,  $m=1.55$  und  $m=1.7$  und an Ni(Mo)/Ti,  $m=1.5$  Vielfachschichten wurde am Forschungsreaktor München II in Deutschland durchgeführt. Ein Reflektometer wurde speziell für diese Messung kleiner Neutronendepolarisation gebaut und optimiert. Die Genauigkeit dieser Messungen war auf  $5 \cdot 10^{-3}$  beschränkt. Beobachtete Depolarisationseffekte sind auf die speziellen Eigenschaften von Polarisator und Analysator in dieser Geometrie zurückzuführen. Im Rahmen beider Experimente wurden auf dem Beobachtungsniveau keine Depolarisationseffekte gemessen, die auf die Beschichtungen zurückzuführen sind.

# Table of Contents

<b>Chapter 1</b>	<b>Introduction</b>	<b>1</b>
<b>Chapter 2</b>	<b>Theory</b>	<b>3</b>
2.1	Interaction of slow neutrons with matter	3
2.1.1	Slow neutrons and types of their interaction with matter	3
2.1.2	Neutron scattering from a single nucleus. Neutron scattering from a collective of nuclei. Fermi potential	5
2.1.3	Index of refraction. Mirror reflection	6
2.1.4	Regime of supermirror reflection	9
2.1.5	Magnetic scattering of neutron	10
<b>Chapter 3</b>	<b>Experiment</b>	<b>13</b>
3.1	Development and production of a non-depolarising supermirror coating	13
3.1.1	Radio frequency magnetron sputtering method	14
3.1.2	Sputtering conditions for deposition of copper and titanium layers	16
3.1.3	Investigation of copper and titanium monolayers with x-rays	16
3.1.4	Investigation of copper and titanium multilayer structures with x-rays	19
3.1.5	Model for the growth of roughness for Cu/Ti pair	22
3.1.6	Optimization procedure of thicknesses of copper titanium layer sequence	23
3.1.7	Production of Cu/Ti supermirrors with $m = 1.2$	27
3.1.8	Production of Cu/Ti supermirrors with $m = 1.6$ and $m = 1.8$	28
3.2	First depolarization measurement at ILL	31
3.2.1	Beam station PF1B at ILL	32
3.2.2	Experimental setup at PF1B	32
3.2.3	Neutron velocity selector	33

3.2.4	Opaque Test Bench . . . . .	35
3.2.5	Depolarization for Cu/Ti multilayer sample with $m=1.2$ . . . . .	37
3.3	Second depolarization measurement at FRM II . . . . .	39
3.3.1	Experimental setup at Mephisto . . . . .	40
3.3.2	Beam station Mephisto at FRM II . . . . .	41
3.3.3	Neutron chopper. Realization of measurement by time of flight method . . . . .	44
3.3.4	Wavelength copper filter . . . . .	47
3.3.5	Supermirror Co/Ti polarizer and analyzer . . . . .	48
3.3.6	Adiabatic spin flipper . . . . .	52
3.3.7	Guiding magnetic field . . . . .	54
3.3.8	Electromagnet, sample holder . . . . .	54
3.3.9	Neutron detector . . . . .	56
3.4	Data analysis . . . . .	56
3.4.1	Neutron beam divergence . . . . .	56
3.4.2	Neutron polarization . . . . .	58
3.4.3	Neutron polarization of the direct beam . . . . .	60
3.4.4	Depolarization measurements with Cu/Ti samples . . . . .	64
3.4.5	Depolarization measurement with Ni(Mo)/Ti sample . . . . .	65
<b>Chapter 4</b>	<b>Summary . . . . .</b>	<b>70</b>
<b>Bibliography</b>	<b>. . . . .</b>	<b>73</b>
<b>Appendix A</b>	<b>Method for the reflectivity and transmittivity calculation of neutrons and x-rays passing multilayer structures. . . . .</b>	<b>76</b>
<b>Appendix B</b>	<b>Sputtering conditions for the Cu/Ti multilayer samples. . . . .</b>	<b>79</b>
<b>Appendix C</b>	<b>The optimization procedure of the layer thicknesses. . . . .</b>	<b>80</b>

Appendix D	The optimal layer sequence to get the maximum reflectivity for the Fe/Si supermirror with $m=2$ , 129 layers.	81
Appendix E	The optimal layer sequence to get the maximum reflectivity for the Fe/Si supermirror with $m=2$ , 109 layers.	83
Appendix F	Sputtering conditions for the Cu/Ti multilayer samples with $m=1.2$ .	85
Appendix G	Sputtering conditions for the Cu/Ti multilayer samples with $m=1.8$ and $m=1.6$ .	86
Appendix H	Experimental polarization spectra obtained during beam time at Mephisto station, FRM II	92
Appendix I	Sputtering conditions for deposition of soft iron layers	95

# Chapter 1

## Introduction

High precision low energy experiments studying  $\beta$ -decay of a free polarized neutron can give a significant contribution to the understanding of the properties of weak interaction. By measuring weak interaction characteristics of the neutron decay (the neutron lifetime  $\tau_n$ , electron-antineutrino correlation coefficient  $a$ , electron asymmetry  $A$ , antineutrino asymmetry  $B$ , proton asymmetry  $C$ ) it is possible to get access to the parameters of the Standard Model of the elementary particles, the Kobayashi-Maskawa matrix element  $V_{ud}$  and the ratio of the axial vector to vector coupling constant  $\lambda = g_A/g_V$ . PERC (Proton Electron Radiation Channel ) belongs to the new generation of spectrometers designed to improve the accuracy of the measurement of angular correlations in the  $\beta$ -decay of free neutrons by one order of magnitude. According to the Particle Data Group [3], the present average values of the asymmetry parameters are limited to an accuracy of  $10^{-3}$ . PERC is “in-beam” neutron decay station: flying neutrons decay inside the neutron guide and the charged neutron-decay products (protons and electrons) are magnetically guided to the suitable place for detection. The inner walls of the neutron guide are equipped with a supermirror. Supermirror coating is a artificial sequence of layers composed of two materials with high scattering contrast. The supermirror covering provides wider angular range compare with a thin layer of natural nickel for the total reflection. Thus a significant neutron flux gain can be achieved with supermirror guide. Because of the location of the neutron guide in a strong magnetic field, the supermirror coating has to be non-magnetic to avoid depolarization caused by neutron reflection from the guide walls. Conventionally, a non-depolarizing covering in the form of Ni(Mo)/Ti or Ni(V)/Ti multilayer are used. But unfortunately, a high precision depolarization test of polarized neutrons which were reflected from these coatings placed in a strong magnetic field has not been performed.

The aim of this work is to develop the supermirror coating based on the non-magnetic materials, Cu and Ti. Neutron guide from these materials could be an alternative to the traditionally used ones. The development of the coating included the searching for the method of optimization of layer thicknesses of a multilayer to get maximum reflectivity for given number of layers; sputtering and investigation with x-rays the multilayer Cu/Ti structures to get a roughness growth law for Cu/Ti pair and finally the sputtering of the Cu/Ti samples with  $m=1.55$  and  $m=1.7$ . Also we performed the high precision depolarization tests of the Cu/Ti multilayers and the Ni(Mo)/Ti multilayer. In this thesis after a short theoretical basis on elastic scattering of neutrons by matter (Chapter 2), the extensive experimental part of the thesis (Chapter 3) describes the development of Cu/Ti supermirror and the two depolarization tests of Cu/Ti and Ni(Mo)/Ti samples performed at the reflectometers of polarized neutrons. The experimental results obtained in both depolarization tests and conclusions about feasibility to use Cu/Ti guide for PERC are presented in the final part of the thesis (Chapter 4).

## Chapter 2

### Theory

#### 2.1 Interaction of slow neutrons with matter

Neutrons with energies a few electron volts or smaller are referred to as slow neutrons. The region of slow neutrons includes the region of thermal neutrons with energies  $10^{-1} - 10^{-2}$  eV and the region of cold neutrons with energies less than  $10^{-2}$  eV.<sup>1</sup> De Broglie wavelength of slow neutrons ( $\lambda = 2\pi/|\vec{k}|$ , where  $\vec{k}$  is the wave vector of a neutron with energy  $E = \hbar\omega$ ) is larger than  $10^{-11}$  m, which is much more than the size of an atomic nucleus and comparable to the interatomic distances in matter. These properties of slow neutrons determine the character of their interaction with matter. Interaction depends on the atomic structure and thermal motion of the atoms of matter.

Physics of slow neutrons is called neutron optics because slow neutrons compared with fast neutrons exhibit stronger wave nature during their passing through matter. The following theoretical sections is a compilation basically from the textbooks [4, 5, 6, 7]. They are about the scattering of slow neutrons from a single nucleus and a collection of nuclei, the reflection of slow neutrons from and transmission through multilayer structures, and the analogy between scattering of slow neutrons by nuclei and x-rays by atoms.

##### 2.1.1 Slow neutrons and types of their interaction with matter

Neutrons are affected by all known types of fundamental interactions: gravitational, electromagnetic, strong and weak interactions. The gravitational interaction of neutrons (of mass  $m_n = 1.674927351 \cdot 10^{-27}$  kg [8]) with the Earth is characterized by

---

<sup>1</sup>Different determinations of neutrons intervals depending on the neutron energy may be found in literature. Given here determination of terminology is taken from textbook “Physics of Low Energy Neutrons” by I. I. Gurevich and L. V. Tarasov.

the potential energy of a neutron in the gravitational field depending on the height  $h$ :

$$V_g = m_n g h \approx 102.5 \cdot 10^{-9} \text{eV} m^{-1} \cdot h[m]. \quad (2.1)$$

Thus neutrons of energy about 100 neV, which corresponds to the kinetic energy of ultracold neutrons, can significantly increase their energy by falling through the distance of 1 m in the gravitational potential. The interesting novel experiments on investigation of the quantum states of neutrons trapped between the Earth's gravitational field and the optical Fermi potential of a mirror were performed at the Institute Laue-Langevin, France [9, 10].

The weak interaction manifests itself mainly in the fact that a free neutron is not stable and decays into a proton, an electron and an electron antineutrino:

$$n \rightarrow p + e^- + \bar{\nu}_e, \quad (2.2)$$

with a decay time  $\tau_n = 885.7 \pm 0.8$  seconds [11]. In 1956 T. D. Lee and C. N. Yang hypothesized parity nonconservation in weak  $\beta$ -interactions [12]. They proposed the possible experiment with oriented  $^{60}\text{Co}$  which might test parity conservation. Already in 1957 C. S. Wu with colleagues performed the experiment and observed an asymmetry in the angular distribution of electrons coming from polarized  $^{60}\text{Co}$  between  $\theta$  and  $(180^\circ - \theta)$  ( $\theta$  is the angle between the orientation of the polarized  $^{60}\text{Co}$  and the momentum of the electron) that demonstrates the parity violation [13]. The problem of parity nonconservation in weak  $\beta$ -interactions stimulated many interesting experiments with slow polarized neutrons. The large number of measurable parameters of weak interactions were derived in these experiments. The correlation coefficients in the  $\beta$ -decay of a free neutron were investigated on the following spectrometers [1]: PERKEO II, PERKEO III for the measurement of the neutron  $\beta$ -asymmetry  $A$  (the angular correlation between the neutron spin and the electron momentum), the antineutrino asymmetry  $B$  (the angular correlation between the neutron spin and the antineutrino momentum) and the proton asymmetry  $C$  (the angular correlation between the neutron spin and the proton momentum) [14, 15, 16, 17]; aSPECT for the measurement of the neutrino-electron angular correlation coefficient  $a$  [18]. These parameter will be also measured in the PERC experiment with increased precision.

For this work nuclear interaction of neutrons with atomic nuclei of matter and

electromagnetic interaction of neutrons with magnetic field produced by atomic electrons of matter are of particular interest. The electromagnetic interaction of the electrically neutral neutron caused by the fact that a neutron with spin  $\frac{1}{2}\hbar$  possesses a magnetic dipole moment  $\vec{\mu}_n$ . The potential energy of a neutron magnetic moment in a magnetic field  $\vec{B}$  is:

$$V_m = -\vec{\mu}_n \cdot \vec{B}. \quad (2.3)$$

The relative direction of a magnetic moment and a magnetic field is determined the sign of the equation.

The strong interaction is responsible for the interaction of a neutron with atomic nuclei. Elastic scattering of a slow neutron by nuclei will be considered in further detail.

### 2.1.2 Neutron scattering from a single nucleus. Neutron scattering from a collective of nuclei. Fermi potential

Within a quantum mechanics picture of scattering of a slow neutron by a free nucleus, the neutron wavefunction at some distance from the scattering nucleus can be represented as a sum of the primary plane wave  $e^{ikx}$  and the scattered spherical wave  $f(\theta)e^{ikr}/r$ . The scattering amplitude,  $f(\theta)$ , is determined by interaction potential of a neutron and a nucleus and this is the basic characteristic of scattering. The neutron scattering cross section is determined by the equation  $\sigma = 4\pi|f(\theta)|^2$ . For slow neutrons the scattering is spherically symmetrical with good approximation and does not depend on the scattering angle  $\theta$ . The scattering amplitude is a constant  $f(\theta) = -a$  (the coefficient  $a$  was first written with minus sign by E. Fermi and L. Marshall in 1947 for reasons of convenience). The parameter  $a$  is called the “scattering length” and has the dimensions of length (the order of magnitude of  $10^{-12}$  cm) [19]. The scattering length  $a$  for most nuclei is positive but few nuclei are known for which scattering length is negative (H, Li, Ti, Mn, Sm). If  $a$  is positive, a neutron wave function is “pushed away” from the region of action of the potential, if  $a$  is negative, a wave function is “attract into” the region of interaction.

In general, the scattering amplitude is a complex number:  $Re(f(\theta)) = -a$ , the imaginary part of  $f(\theta)$  describes the probability of the neutron absorption by the nucleus,  $Im(f(\theta)) = \frac{(\Gamma_n/2k)}{(E-E_0)+i\Gamma/2}$ , where  $\Gamma_n$  and  $\Gamma$  are the neutron and total width of

the neutron resonance with energy  $E_0$  and  $E$  is the neutron energy [5].

If the scattering nucleus has a nonzero spin  $I$ , the scattering length may take on two values,  $a^+$  or  $a^-$ , depending on the total spin of the neutron and nucleus ( $I + \frac{1}{2}$  or  $I - \frac{1}{2}$ ).

In interaction of neutrons with condensed matter the scattering nuclei are chemically bonded. Incident slow neutron interacts with the collection of nuclei. In 1936 E. Fermi showed that interaction of slow neutrons with bound nuclei can be considered within the Born approximation if to use the interaction potential of slow neutron with bound nucleus  $i$  in the form (the so-called Fermi pseudopotential):

$$V_i = \frac{2\pi\hbar^2}{m} b\delta(\vec{r} - \vec{r}_i), \quad (2.4)$$

where  $\vec{r}$  and  $\vec{r}_i$  are the radius vectors of the neutron and the collection of nuclei (molecule or crystal),  $m$  is the mass of the neutron and  $b = \frac{m}{\mu}a$  is the coherent scattering length (“bound nucleus scattering length”) with  $\mu$  - reduced mass of the neutron and the collection of nuclei. The Fermi pseudopotential describes the interaction of the neutron with the nucleus as a point interaction and it is possible to use perturbation theory to calculate the neutron wave function (and therefore the scattering cross section) outside the region of interaction. The effective potential, volume averaged of the Fermi potentials Eq. 2.4, describes the interaction of slow neutrons incident on a solid (or liquid) surface:

$$V = \frac{\hbar^2}{2m} 4\pi b N, \quad (2.5)$$

where  $N$  is the density of atoms in the scattering material.

The coherent scattering lengths  $b$  have been determined experimentally for a large number of nuclei. For example, the neutron coherent scattering lengths and cross sections are collected in the Neutron Data Booklet of ILL [20].

### 2.1.3 Index of refraction. Mirror reflection

Interference of neutron waves which are coherently scattered by nuclei of matter defines a number of optical phenomena, including neutron refraction and neutron reflection on a surface. In 1946 E. Fermi and W. H. Zinn observed the total reflection of non-monochromatized thermal neutrons on mirrors [21]. The total reflection of

slow neutrons on mirrors with positive scattering length occurs at small glancing angles. The index of refraction of the neutron wave at a vacuum-medium boundary in the form which was used by E. Fermi is given by:

$$n = 1 - \lambda^2 Nb/2\pi, \quad (2.6)$$

where  $b$  is the coherent scattering length on the bound nucleus,  $N$  is the density of atoms in the medium, and  $\lambda$  is the neutron wavelength. This formula takes into account just the nuclear interaction of a neutron with medium. It is possible to get the index of refraction in the form Eq. 2.6 by using the effective potential Eq. 2.5, which acts on the neutron in the medium, for example as it was done in [22]. The index of refraction of neutron waves is defined by the neutron speed in a vacuum,  $v_0$ , and in a medium,  $v$ :

$$n = \frac{v}{v_0}. \quad (2.7)$$

The total energy of a neutron in a vacuum is equal to its kinetic energy,  $E_0 = mv_0^2/2$ . During penetration into the medium the total energy of a neutron does not change, but its kinetic energy changes by an amount given by the potential energy (energy of interaction of a neutron with a medium),  $V = \frac{2\pi\hbar^2}{m}bN$ . In the case of positive effective potential ( $b > 0$ ), the speed of a neutron in the medium becomes less than in vacuum, corresponding to  $n < 1$ .

$$\frac{mv^2}{2} = E_0 - V \Rightarrow n^2 = 1 - \frac{V}{E_0}. \quad (2.8)$$

Because of the small value of  $V/E_0$  ( $V \sim 10^{-7}eV$ ), for slow neutrons using Taylor expansion we can find out the expression:

$$n = 1 - \frac{V}{2E_0}. \quad (2.9)$$

Considering that  $\lambda = h/mv$ , for the index of refraction we get the expression:

$$n = 1 - \lambda^2 Nb/2\pi. \quad (2.10)$$

There is a maximum glancing angle,  $\theta_{cr}$ , for which the total reflection of neutrons on mirrors occurs,  $\theta_{cr}$  is determined by:

$$\cos\theta_{cr} = n. \quad (2.11)$$

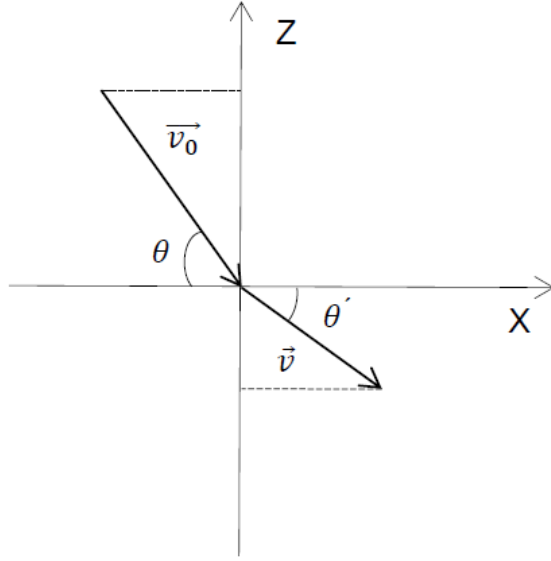


Figure 2.1: Refraction of neutrons at the boundary of vacuum-medium.

The expression Eq. 2.11 is obtained from following consideration. The neutron with speed  $\vec{v}_0$  is incident on the mirror with a positive effective potential ( $n < 1$ ) at the angle  $\theta$ , Fig. 2.1. The neutron penetrating the medium travels with speed  $\vec{v}$  at angle  $\theta'$  to the boundary between two media. The force acted on the neutron is perpendicular to the surface, which is why just the normal component of the neutron speed changes and the parallel component of the speed does not change  $|\vec{v}_0|\cos\theta = |\vec{v}|\cos\theta'$ . Thus,

$$n = \frac{v}{v_0} = \frac{\cos\theta}{\cos\theta'}. \quad (2.12)$$

Classically total reflection of the incident neutrons occurs if the normal component of the speed,  $\vec{v}_0$ , is less than the value for which neutrons can overcome the potential barrier  $V$ .<sup>2</sup> For the case of the total reflection  $\theta' = 0$ ,  $\cos\theta' = 1$ , the glancing angle  $\theta$  is called critical, thus  $\cos\theta_{cr} = n$  and finally, the critical angle for the total neutron reflection on the mirror is given by:

$$\theta_{cr} = \lambda \sqrt{\frac{nb}{\pi}}. \quad (2.13)$$

For instance, the  $\theta_{cr}$  for neutrons with energy of 1 Å incident on the mirror produced from natural Ni is 1.7 mrad ( $N_{Ni} = 9.131 \cdot 10^{28} \text{ m}^{-3}$ ,  $b_{Ni} = 10.3 \text{ fm}$ ). The neutrons

<sup>2</sup>In quantum mechanics, the neutron with  $E_o^\perp < V$  will be also reflected but there is nonzero probability of penetrating the barrier.

which impinge on the Ni surface at the angles  $\theta < \theta_{cr}$  undergo the total reflection. Natural Ni has one of the maximum values of the scattering length (and hence the critical angle for the total reflection) and historically it was chosen as a standard. The mirrors with a critical angle 1.7 mrad for the total reflection of neutrons with energy 1 Å is characterized by factor  $m=1$ . The device, a neutron guide, is based on the phenomenon of total neutron reflection. The neutrons, by multiple reflections from the well-polished walls of a neutron guide with a rectangular cross section, can be transported over a distance of tens of meters from the reactor core to the region of low background from fast neutrons and gamma radiation. The neutron guides can be bent and the radius of curvature determines the critical wavelength of the neutrons which can be transported. Initially, natural Ni was used for production of neutron guides, but later the mirror coatings from  $^{58}\text{Ni}$  started to be used which increased the critical angle compare with the critical angle of natural Ni for the total reflection by a factor  $m=1.2$  ( $b(^{58}\text{Ni}) = 14.4 \text{ fm}$ ).

#### 2.1.4 Regime of supermirror reflection

The studies of neutron scattering on sciatic nerve fibers by B. P. Schoenborn, A. C. Nunes and R. Nathans (1970) and by D. A. Kirschner and D. L. D. Caspar (1972) in  $D_2O$  suggested “that a few repeats of relatively thick layers with alternative positive and negative scattering density should produce efficient monochromators”. In 1973 B. P. Schoenborn, D. L. D. Caspar and O. F. Kammerer presented a “Novel Neutron Monochromator” [23]. The covering from alternating layers of two metals, Mn ( $b_{Mn} = -3.6 \text{ fm}$ ) and Ge ( $b_{Ge} = 8.2 \text{ fm}$ ), was evaporated on an optical flat surface. The reflectivity of this multilayer was 30% at  $1^\circ$  for the neutrons with the wavelength of 4 Å. The authors noticed that “the scattering from such multilayers cannot be expressed in terms of simple Bragg diffraction theory but the scattering factor should be proportional to the difference in the unit-volume scattering lengths of the two materials used. If the bilayer is composed of two equally thick layers, then the even-order reflections will be absent since the scattering transforms will vanish for these reflections. The higher odd orders will be absent if a sinusoidally varying scattering profile can be produced”. The multilayer in the form of Ni/Al was used by

D. Marx in 1971 to guide the thermal and subthermal neutrons along bent trajectories [24]. About 100 sandwiches of alternate Ni (thickness 55 nm) and Al (thickness 320 nm,  $b_{Al} = 3.449 fm$ ) layers were evaporated. During reflectivity measurements the neutrons with wavelength 2 Å and greater have been reflected up to 4°, which corresponds to about 20 times the critical angle of total reflection. Maxima of neutron intensity were observed at 1.35°, 2.38° and 4.42°.

After a series of investigations of simple multilayer structure with the same thickness of layers F. Mezei proposed a new interference optical device for neutrons, the neutron supermirror. It artificially increases the critical angle for total reflection and provides high reflectivity among the whole region of the supermirror reflection. He proposed the method for a supermirror layer design based on Bragg reflection of the incident neutrons from the system of double layers with gradually changing thicknesses of the layers. In this approach the supermirror represents an artificial crystal lattice with varying period such that neutrons with different wavelength (less than  $\lambda_{cr}$ ) can “find” the appropriate period for total reflection. Later, using the spin dependence of the neutron scattering length of the ferromagnetics, F. Mezei proposed supermirror polarizers [25].

In this thesis we were developing the supermirror covering with  $m$  value of about 2 to gain in neutron density in the guide inside PERC. We worked with Cu ( $b_{Cu} = 7.718 fm$ ) and Ti ( $b_{Ti} = -3.438 fm$ ).

### 2.1.5 Magnetic scattering of neutron

The magnetic dipole moment of a neutron  $\vec{\mu}_n$  interacts with an externally applied magnetic field and with an internal field of magnetic atoms. The internal magnetic field is determined by the two components, the orbital and spin angular momenta. The orbital component is connected with the movement of an electron in an atomic orbit (“orbital current”) and the spin component is connected with the electron spin (“spin current”). In most cases the orbital component does not play a role: it equals zero (for s-state) or it is quenched. The spin component is induced by the electrons of an atom with the uncompensated spins. This spin dependent magnetic interaction gives a contribution to the effective potential and to the index of refraction:

$$V = \frac{\hbar^2}{2m} 4\pi b N \pm \mu_n B, \quad (2.14)$$

$$n = 1 - \lambda^2 \left( \frac{Nb}{2\pi} \pm \frac{m}{4\pi^2 \hbar^2} \mu_n B \right). \quad (2.15)$$

The “+” sign corresponds to the interaction with neutron spin pointing along the field  $\vec{B}$ , the “-” sign corresponds to the opposite direction.

The amplitudes of the magnetic scattering of neutrons on polarized and nonpolarized atoms are calculated in [5]. Cases of the polarized and unpolarized incident neutron beams and scattering with and without flipping of the neutron spin are considered. The general expression for the magnetic scattering amplitude of a slow neutron by a free atom is (without including of the effect of “orbital currents”):

$$f_{s'm'|sm} = 2r_0\gamma P(\vec{k}_0 - \vec{k}) \langle s'm' | (\vec{S}\vec{s}_n) - (\vec{e}\vec{s}_n)(\vec{S}\vec{e}) | sm \rangle, \quad (2.16)$$

where  $s$ ,  $m$ ,  $\vec{k}_0$  are the spin quantum number of the neutron, the spin quantum number of an atom, the neutron wave vector of the initial state of the system and  $s'$ ,  $m'$ ,  $\vec{k}$  are characteristics of the final state of the system (after scattering).  $r_0$  is the classical electron radius,  $\gamma$  is the magnitude of the neutron magnetic moment expressed in nuclear magneton  $\mu_N$ ,  $\vec{S}$ ,  $\vec{s}_n$  are the spins of an atom and a neutron,  $\vec{e} = \frac{\vec{k}_0 - \vec{k}}{|\vec{k}_0 - \vec{k}|}$  is the unit vector of scattering.  $P(\vec{k}_0 - \vec{k})$  is the magnetic form factor of the atom determined by the distribution of electrons with uncompensated spins in the atom. In general, the scattering of a slow neutron on an atom is described by amplitude:

$$f = f_n \pm |f_m|, \quad (2.17)$$

where  $f_n$  (see Section 2.1.2) and  $f_m$  are amplitudes of the nuclear and magnetic scattering. Values of nuclear and magnetic amplitudes for magnetic materials have the same order of magnitudes. The differential cross section is:

$$\frac{d\sigma}{d\Omega} = f_n^2 + f_m^2 \pm 2f_n|f_m|. \quad (2.18)$$

The sign of the interference term  $2f_n|f_m|$  is positive if the neutron spin and the magnetization vector (magnetic induction  $\vec{B}$ ) are parallel, and negative if the neutron spin and the magnetization vector are antiparallel. The interference term is absent for the case of nonpolarized neutrons or nonpolarized atoms (paramagnetic state).

Depolarization of slow neutrons passing through a ferromagnetic sample placed in a weak magnetic field ( $D = P/P_0$ , where  $P_0$  is the polarization of the incident neutrons,  $P$  is the polarization of the transmitted neutrons) was theoretically investigated

in detail by O. Halpern and T. Holstein [26]. They showed that for weakly magnetized ferromagnet, in which the number of domains are large and magnetization  $\vec{M}$  is directed to different sides, the neutron spin is rotated around  $\vec{B}$  through a certain angle and after passing a quite long sample the neutron beam is depolarized. Theoretical investigation of the depolarization of neutrons passing through a ferromagnet in the saturated state was performed by S. V. Maleev and V. A. Ruban in [27]. This is the case of a strong external magnetic field: there are no domains in the material but “the ferromagnet still contains random magnetic fields due to the thermal motion of the spins. Obviously, the action of these random fields on the polarized neutrons should lead to a certain depolarization of the transmitted beam”. If neutron polarization and external magnetic field  $\vec{B}$  are parallel, depolarization is caused by the transverse fluctuations of the induction  $\vec{B}$  within the sample. S. V. Maleev and V. A. Ruban noted that the depolarization of saturated magnetic materials due to the thermal motion is small and in the roughest approximation is mainly proportional to the temperature. Authors also showed that depolarization connected with the scattering from nuclei with a spin is very small and is determined by incoherent nuclear scattering due to spins.

## Chapter 3

### Experiment

#### 3.1 Development and production of a non-depolarising supermirror coating

The aim of this thesis was to demonstrate feasibility of production of the supermirror non-depolarizing neutron guide from the diamagnetic material Cu and the paramagnetic material Ti. Such neutron guide could be an alternative to the traditionally used non-magnetic neutron guide based on the non-ferromagnetic alloy Ni(Mo) and Ti. A Ni(Mo)/Ti non-magnetic neutron guide was developed and produced by a magnetron sputtering method in PNPI (Petersburg Nuclear Physics Institute), Russia [28]. The test of Ni(Mo)/Ti supermirror coatings at polarized neutron reflectometer showed the coincidence of reflectivity curves for both neutron spin components  $N_+$  and  $N_-$  within statistics. The statistical error was at  $10^{-3}$  level. The incident neutron beam was polarized to  $P \geq 0.97$ . The magnetic field during measurement was varied (up to 450  $Oe$ ).

In 1994 the supermirror with 20 pairs of Cu/Ti coating had been thermally evaporated by the same group from PNPI. The samples were used for the study of roughness and interdiffusion in thin-film structures [29]. The statistical roughness growth low was found, the dependency of the growth rate from materials and deposition techniques was observed. The roughness growth rate for a thermally evaporated Cu/Ti pair was found to be quite large. But the new method developed for the supermirror thickness sequence law, which takes into account the roughness growth rate, did not give the high reflectivity for the Cu/Ti pair.

This chapter is intended to describe the process of development and production of Cu/Ti supermirror coating performed by our group at Heidelberg University. First of all, the development process included the creation of a method for calculation of the optimal sequence of the thicknesses for the supermirror reflection of the pair materials. Then the adjustment and calibration of the sputtering machine were performed.

Studying the surface roughness and interlayer diffusion was done. And finally, the samples were produced.

### 3.1.1 Radio frequency magnetron sputtering method

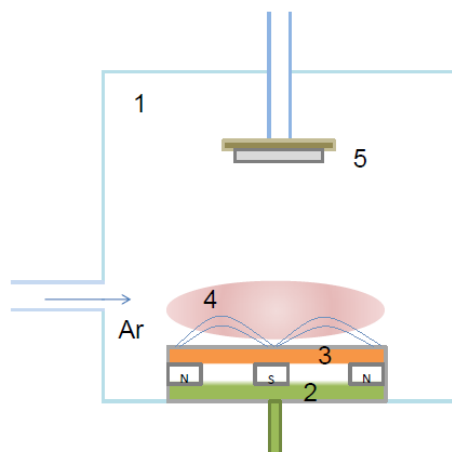
The radio frequency (RF) magnetron sputtering is the process for wide range thin film deposition onto a surface. The RF magnetron deposition method has been developed rapidly in the eighties of the 20th century [30]. The schematic representation and photo of the vacuum chamber for the magnetron deposition are given in Fig. 3.1. Normally the chamber (1) is evacuated to  $10^{-7} mbar$ . The low pressure in the chamber aids to minimize contaminations in the films. After reaching of the satisfactory pressure, the working gas, usually argon, is introduced to the chamber to a pressure  $10^{-2} mbar$ . Then, in the case of the RF magnetron deposition, the alternating voltage of a radio frequency (usually  $13.56 MHz$ ) is applied to the sputtering target (3) and the substrate-holder (5) in order to ignite the plasma (4). The electrons accelerated in the space between the target and the substrate ionize argon atoms. The electrons are more mobile than the positive argon ions, so more electrons reached the target during the positive semi-cycle than the positive ions during negative semi-cycle.<sup>1</sup> The target becomes a negatively charged cathode, which makes the deposition process possible. The argon ions ( $Ar^+$ ) bombard the cathode-target and remove target atoms which may condense on a substrate as a thin film. The system of permanent magnets (2) placed behind the target (one pole placed at the central axis of the target, second pole is made into a ring along the outer edge of the target) traps the electrons in the target region.

From the one side these electrons cannot hit and damage the substrate, from the other side the trapping electrons increases the argon ionization probability and the deposition rate. In Fig. 3.2 a) it is seen the typical recess of the ring shape in the place of the maximum electron density above the target. Fig. 3.2 b)<sup>2</sup> shows a burning plasma above a triangular target. You can find more information about the magnetron sputtering for example in this review [31] or in [32].

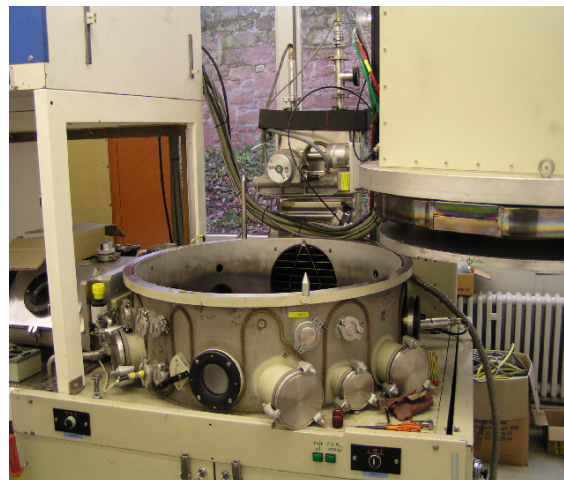
---

<sup>1</sup>Taken from the sputtering machine user's manual.

<sup>2</sup>All photos are made by Thorsten Lauer.

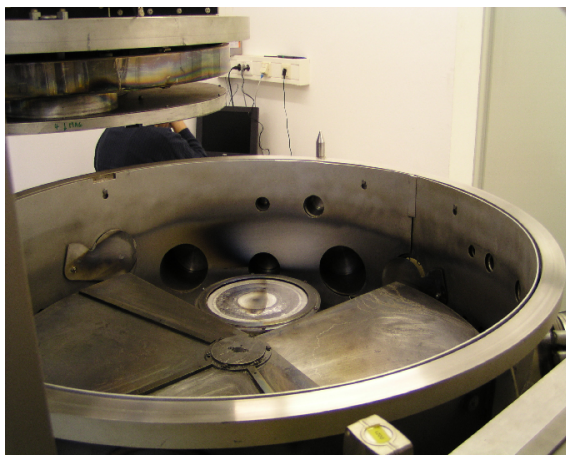


a)

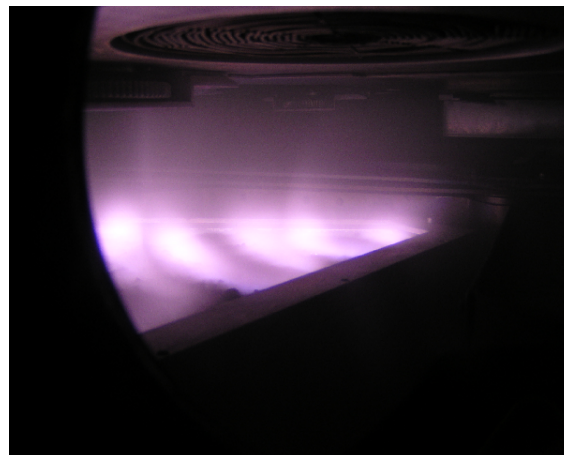


b)

Figure 3.1: Vacuum chamber for the RF magnetron sputtering: a) schematic representation, where (2) is the system of permanent magnets, (3) is the sputtering target, (4) is the plasma, (5) is the substrate-holder ; b) photo.



a)



b)

Figure 3.2: Vacuum chamber for the RF magnetron sputtering: a) photo of a target; b) burning plasma.

### 3.1.2 Sputtering conditions for deposition of copper and titanium layers

Heidelberg University has a sputtering machine for the direct current and the radio frequency diode, magnetron or triode sputtering. The used machine was purchased from the company Alcatel and was assembled by the university employees. Historically, the machine has been operated in the RF magnetron sputtering mode. The pumping assembly of the sputtering machine is designed to maintain a stable pressure in the chamber up to  $5 \cdot 10^{-8}$  mbar, but due to the leaks in the vacuum chamber only a minimum pressure of  $4 \cdot 10^{-6}$  mbar was achieved.

The substrate-holder may be rotational with variable speed and movable in a vertical direction. The larger the rotation speed of the substrate-holder, the thinner the layer will be deposited and the more homogeneous. The chamber is equipped with motor-driven double shutter. The shutter opens the desired target during the sputtering. Before sputtering we repaired and properly adjusted the substrate-holder disk and the shutter system that allowed us to have reproducibility of the layer thickness from cycle to cycle. Before plasma ignition, the substrate is fixed at the side opposite from the open target. And the substrate-holder disk starts the rotation after the plasma parameters adjustment.

To remove the oxidation layer and other contaminants from the target surface after opening of the vacuum chamber or after a long inactivity of the machine, the titanium and copper targets had been burned 10 – 20 minutes. The machine parameters were: RF generator power – 500 W; working pressure (obtained by chamber pumping system and Ar gas introduction) in the chamber  $\approx 3 \cdot 10^{-3}$  mbar.

In order to eliminate contamination of mineral type from the surface of a substrate we performed ionic cleaning. The substrate undergoes ionic bombardment by plasma about 10 minutes. The machine parameters for the ionic cleaning were: RF generator power – 200 W; working pressure  $\approx 6 \cdot 10^{-3}$  mbar. The Cu and Ti layers were deposited at the generator power of 500 W at three different working pressures:  $1 \cdot 10^{-3}$  mbar,  $2.7 \cdot 10^{-3}$  mbar,  $5 \cdot 10^{-3}$  mbar.

### 3.1.3 Investigation of copper and titanium monolayers with x-rays

The wavelength and scattering cross section of slow neutrons and x-rays are comparable. The general properties of interference for neutrons and x-rays are similar. X-ray

reflection from a surface provides a method for the studying of certain surface properties of condensed matter. Most of our samples has been studied by x-ray reflection for the determination of the interaction potentials of x-rays with layer materials, the layer thickness, and roughness.

The Cu and Ti monolayers at different working pressures were produced in order to calibrate (to determine which thickness of the material is deposited at given parameters: generator power, working pressure, rotation speed of the substrate-holder and the number of the turns of the substrate-holder) and to check the thickness reproducibility of the sputtering machine. As it is mentioned in the previous section Cu and Ti samples were deposited by the RF magnetron sputtering technique. The films were sputtered onto a glass substrate of 1 *mm* thick. The Cu layers were covered with 5 *nm* of Ti to prevent oxidation. In this section I will describe the two monolayer Cu and Ti samples. The Cu sample was produced in October 2011 at the working pressure  $2.7 \cdot 10^{-3}$  *mbar*. The substrate-holder was rotated by 5 turns above the Cu target with a speed setting of 500 (corresponding to 1 turn of the substrate-holder per 1 minute) and 1 turn above the Ti target with a speed setting of 500. The Ti sample was produced in October 2012 at the working pressure  $1 \cdot 10^{-3}$  *mbar*. The substrate-holder was rotated by 10 turns above the Ti target with a speed setting of 500. The samples were investigated at an x-ray diffractometer in the Mainz University and at the S-DH company, Heidelberg. The basic scheme of an x-ray diffractometer (see Fig. 3.3) includes a monochromatic source of x-rays (for our case we have characteristic wavelength of 1.54 Å,  $CuK_{\alpha_1}$ ) and an x-ray detector. The intensity of the x-rays reflected from the studied samples is measured as a function of x-ray incident angle. The incident x-rays hit the sample at angle  $\theta$ . The reflected intensity is registered at the same angle from the surface sample, but at an angle  $2\theta$  from the transmitted x-ray beam through the sample. The typical x-ray reflectivity spectra (here and further not normalized) obtained with Cu and Ti monolayers are shown in Fig. 3.4. The x-rays undergo total external reflection (up to  $0.75^\circ$  for the Cu covering, up to  $0.30^\circ$  for the Ti covering) at incident angles smaller than the critical angle for a given material and for a given x-ray wavelength. The position and shape of the edge of total reflection region is determined by the electron density of the film material and the surface roughness of the film. At incident angles larger than the critical angle,

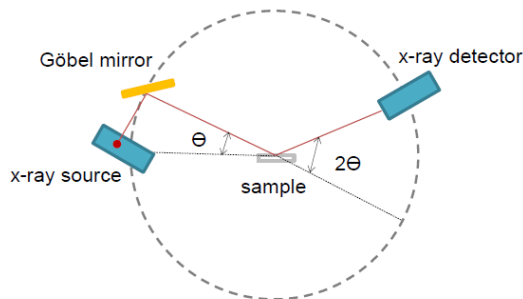


Figure 3.3: The scheme of an X-ray diffractometer.

x-rays start to penetrate the surface and the reflectivity curve drops extremely. The fringes at this region are the result of the interference between the x-rays partially reflected from the air-film and the film-substrate interfaces. The fringes are called the Kiessig fringes, named after the man who observed them at the first time [33]. The distance between the two neighboring maxima (or minima) of the Kiessig fringes (see Fig. 3.4) are determined by the film thickness. The amplitude of the fringes is determined by the interlayer roughness. Thus the main layer characteristics can be determined from the x-ray reflectivity curve.

The red curves shown in Fig. 3.4 are the fitting curves obtained by using the program Supermref (by Ulrich Schmidt) to calculate the reflectivity and transmittivity of neutrons and x-rays passing the multilayer system with interface roughness. The program is based on the method in which the multilayer is presented as one-dimensional square-well potential. The plane waves (x-ray or neutron radiation) entering the multilayer structure undergo multiple partial reflection and transmission at the layer interfaces and the resulting reflectivity and transmittivity are determined by the interference of all reflected and transmitted waves. The consideration of this method and expressions for the reflectivity and the transmittivity of x-rays and neutrons are presented in the Appendix A .

The layer parameters obtained by the fitting procedure are as follows. The thickness of the Cu layer (Fig. 3.4 a)) is  $56.6 \pm 0.3 \text{ nm}$ , the roughness of the surface is  $1.7 \pm 0.1 \text{ nm}$ . The thickness of the Ti layer (Fig. 3.4 b)) is  $51.6 \pm 0.3 \text{ nm}$ , the roughness of the surface is  $1.9 \pm 0.1 \text{ nm}$ . The surfaces of the films are rather rough due

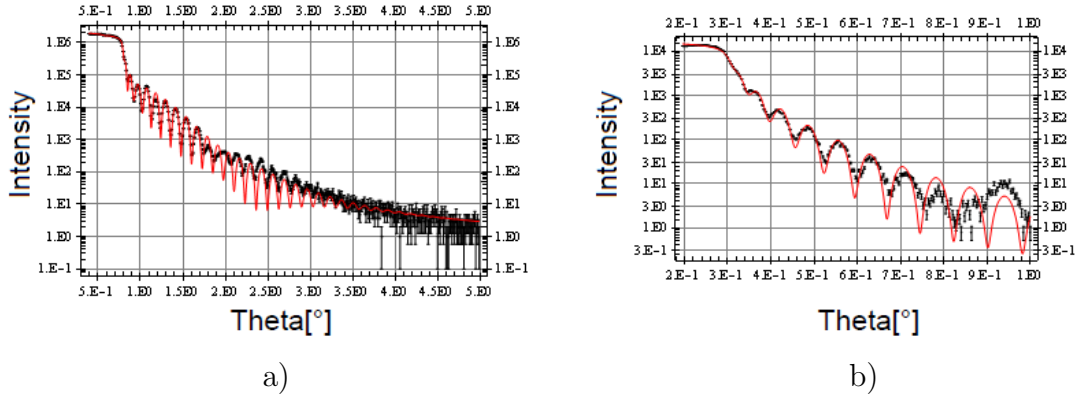


Figure 3.4: X-ray reflectivity spectra obtained with: a) Cu monolayer with the thickness of 57 nm; b) Ti monolayer with the thickness of 52 nm. Black - experimental data, red - simulation.

to the oxidation of the top layer. The roughness of the glass substrate was fixed to the reasonable value of 0.5 nm. This is the typical value of roughness for the float glass. Some amount of water accumulates on the rough surface of the samples. Better agreement of the experimental x-ray reflectivity with the theory was obtained by adding a top water layer with thickness around 0.5 nm to the layer sequence.

### 3.1.4 Investigation of copper and titanium multilayer structures with x-rays

The Cu/Ti multilayer structures of three, five, eleven, thirty-one and sixty-one layers were sputtered to investigate interface roughness of the samples, confirm the reproducibility of the thickness of the deposited metals and check the working stability of the machine. The multilayer structures were composed by Cu and Ti layers with the same thickness except for few samples with doubled thickness of the Cu layer. Such samples give a clear and vivid picture of the x-ray reflectivity curve. In Fig. 3.5 one can see the experimental x-ray reflectivity curves for the three (layer composition is Ti(20 nm)/Cu(40 nm)/Ti(20 nm)) and five (layer composition is Ti(20 nm)/Cu(20 nm)/Ti(20 nm)/Cu(20 nm)/Ti(20 nm)) layer Cu/Ti samples. The sputtering conditions such as generator power, working pressure, number of rounds of the substrate-holder and speed of the substrate holder used during the samples preparation are presented in Tables B.1 and B.2 in Appendix B. The fitting procedure (red curves in

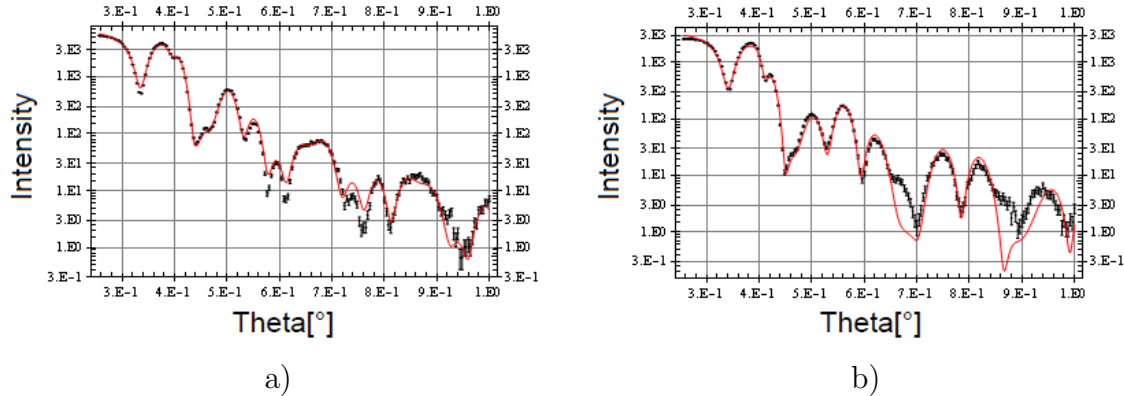


Figure 3.5: X-ray reflectivity spectra obtained with: a) Cu/Ti multilayer sample with layer composition Ti(20 nm)/Cu(20 nm)/Ti(20 nm)/Cu(20 nm)/Ti(20 nm); b) Cu/Ti multilayer sample with layer composition Ti(20 nm)/Cu(40 nm)/Ti(20 nm);

the Fig. 3.5) performed with the Supermref program gives for the three layer sample: thickness of the Ti layer is  $17.9 \pm 0.3 \text{ nm}$ , thickness of the Cu layer is  $39.2 \pm 0.3 \text{ nm}$ , roughness of the top layer is  $1.4 \pm 0.1 \text{ nm}$ ; for the five layer sample: thickness of the Ti layer is  $18.4 \pm 0.3 \text{ nm}$ , thickness of the Cu layer is  $20.4 \pm 0.3 \text{ nm}$ , roughness of the top layer is  $1.5 \pm 0.1 \text{ nm}$ . The roughness of the interfaces is about the same for both samples and for all interfaces,  $0.5 - 0.7 \text{ nm}$ , that is comparable with the roughness of the glass substrate,  $0.5 \text{ nm}$ .

The series of the thirty-one layer samples at three different deposition pressures were produced for determination of the optimal conditions to get minimal layer roughness. Sputtering at low deposition pressure produces films with the smaller atomic density and larger mobility of the surface atoms. Thus we expected to observe the minimal film roughness for the sample sputtered at low working pressure. This was demonstrated with x-ray reflectivities obtained for the three thirty-one layer samples sputtered at the working pressures:  $1 \cdot 10^{-3} \text{ mbar}$ ,  $2.7 \cdot 10^{-3} \text{ mbar}$ ,  $5 \cdot 10^{-3} \text{ mbar}$ , Fig. 3.6. The thickness of each Cu and Ti layer was supposed to be about 20 nm. For all samples the peaks of higher order of Bragg reflection are well defined but better agreement between the experimental x-ray reflectivity data and the theoretical curve (see Fig. 3.6) was observed for the sample produced at low deposition pressure,  $1 \cdot 10^{-3} \text{ mbar}$ . The layer thicknesses obtained by the fitting procedure for this sample are: Ti layer -  $15.8 \pm 0.3 \text{ nm}$ , Cu layer -  $21.3 \pm 0.3 \text{ nm}$ . The model for the roughness growth rate determined from the analysis of this samples will be presented in the next

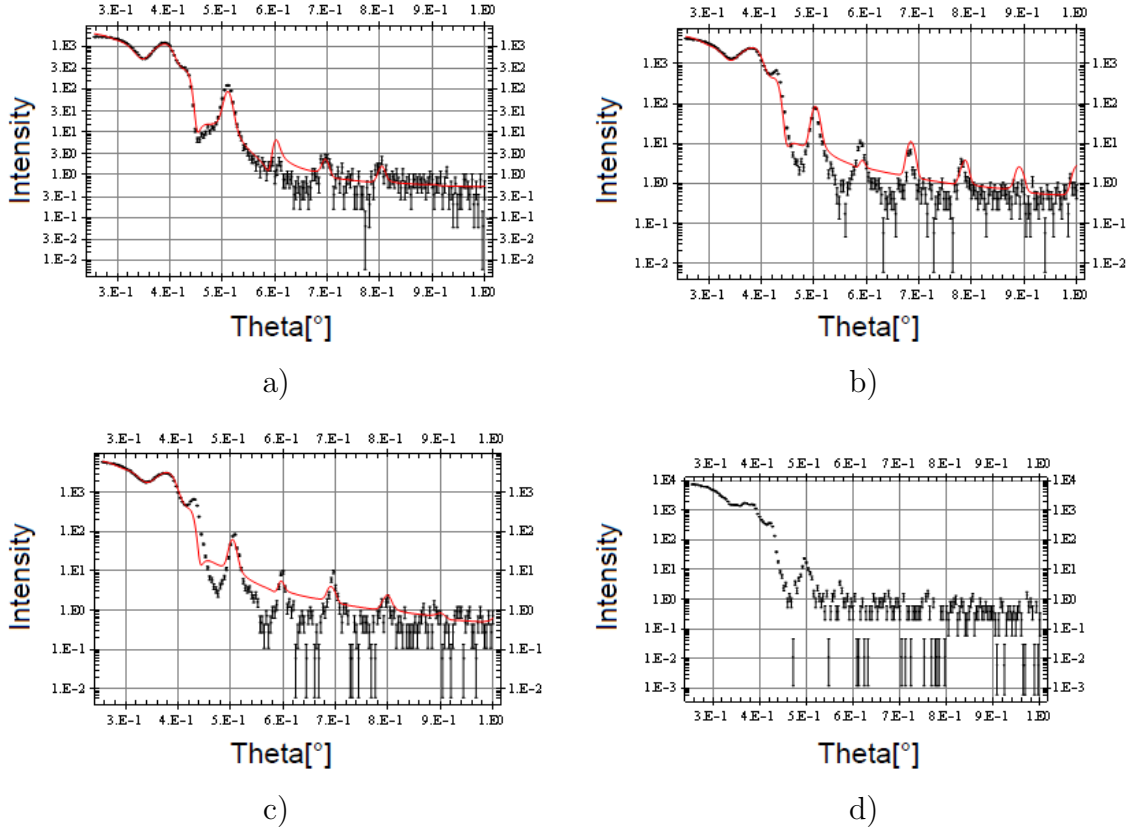


Figure 3.6: X-ray reflectivity spectra obtained with the Cu/Ti multilayer samples (layer number - 31, thickness of each layer 20 nm) at the different working pressure: a)  $1 \cdot 10^{-3}$  mbar; b)  $2.7 \cdot 10^{-3}$  mbar; c)  $5 \cdot 10^{-3}$  mbar; d) x-ray reflectivity spectrum obtained with the Cu/Ti multilayer samples (layer number - 61, thickness of each layer 20 nm) at the working pressure  $1 \cdot 10^{-3}$  mbar.

section.

The total thickness of Cu/Ti samples with  $m=1.8$  or  $m=1.6$  is approximately  $1.2 \mu\text{m}$  and the roughness is function of the layer thickness. This is why the sixty-one layer sample (each Cu and Ti layer per 20 nm) with the total thickness  $1.22 \mu\text{m}$  was sputtered and investigated. The experimental x-ray reflectivity curve for this sample is shown in Fig. 3.6 d). Unfortunately good agreement between the experimental and theoretical reflectivity curves was not obtained.

The two eleven layers samples were sputtered to find out if it is possible to make night break during sputtering of the main sample with 119 layers (sputtering of 119 layer sample takes about 20 hours). The samples were sputtered at a working pressure of  $2.7 \cdot 10^{-3}$  mbar. Second eleven layers sample after sputtering of the five layers was

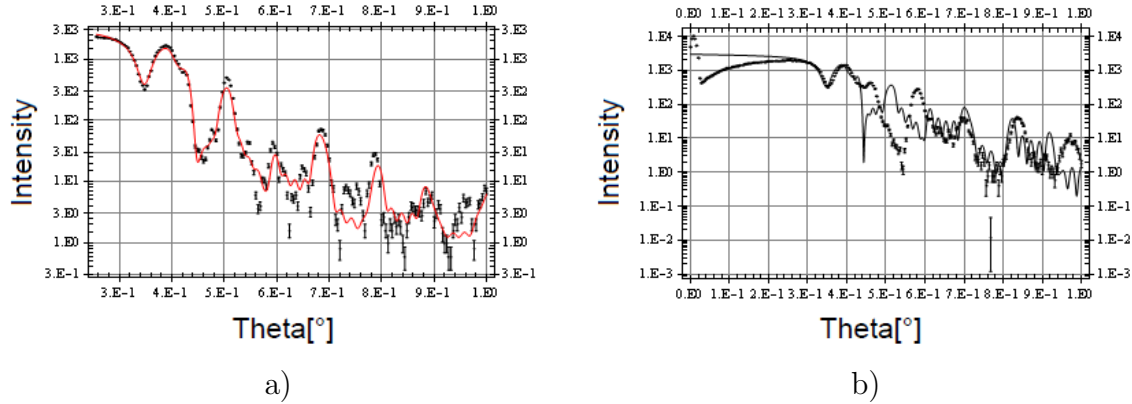


Figure 3.7: X-ray reflectivity spectra obtained with the Cu/Ti multilayer samples (layer number - 11, thickness of each layer 20 nm) at the working pressure  $2.7 \cdot 10^{-3}$  mbar: a) without break during the deposition; b) with the 20 hours break during the deposition.

left in the vacuum chamber for the night break at a pressure  $1 \cdot 10^{-5}$  mbar. Comparison of the x-ray reflectivity curves obtained for the samples produced without night break (Fig. 3.7 a)) and with night break (Fig. 3.7 b)) shows a big difference of the two curves (most likely due to the strong surface oxidation of the layer on which the deposition break was) so it is impossible to make long pauses in the deposition process. Thus, after production and investigation of many Cu/Ti multilayer samples with x-ray we found out the correct model for the roughness growth rate of the Cu/Ti pair. We studied the working stability of the machine and confirmed very good reproducibility of layer thickness of the sputtered materials.

### 3.1.5 Model for the growth of roughness for Cu/Ti pair

The reflectivity of multilayers strongly depends on their interlayers. In practice, the interlayers are rough, and diffusion processes in the multilayer materials take place. To model the changing roughness from layer to layer in a supermirror is a complicated physical problem. For modeling of the roughness growth of Cu/Ti pair we used the same model which was applied to Ni/Ti pair during development of the Ni/Ti supermirror neutron guide. The roughness of  $j$ th layer is:

$$r_j = par_1 + par_2 \cdot \left(\frac{d_j}{d_{tot}}\right)^{par_3}, \quad (3.1)$$

where  $par_1$  is the roughness of substrate (in our case the glass roughness is 0.5 nm),  $par_2$  is the accretion of roughness (roughness of the top layer minus the substrate roughness, for the covering about 1.2  $\mu\text{m}$  thick  $par_2 = 3.8$  nm),  $par_3$  is the power of the growth curve of roughness ( $par_3 = 0.5$  corresponds to the purely statistical aggregation),  $d_j$  and  $d_{tot}$  are the thicknesses of the  $j$ th layer and all layers below the  $j$ th layer respectively. It was found that for Ni/Ti the power of the growth curve of roughness is 0.8. Thus we assumed that for Cu/Ti the roughness grows from layer to layer (roughness is function of thickness) according to the “0.8 power law”. The growing of the surface during the sputtering can be represented as snow falling randomly on a landscape, this case corresponds to the power 0.5 of the growth curve of roughness. But the changing of the position of the sputtered atoms after sticking to the surface caused by interaction between atoms influences the power of the growth curve of roughness. During the analysis of the thirty-one layer Cu/Ti samples (section 3.1.4), better agreement between the experimental and the theoretical x-ray curves was obtained for  $par_3 = 0.75 \pm 0.18$ .

### 3.1.6 Optimization procedure of thicknesses of copper titanium layer sequence

The concept of the regime of the supermirror reflection for neutrons was explained in section 2.1.4. The devices, increasing the critical angles for the total external reflection, represent thin layer structures of two materials alternatively deposited on a substrate. The materials have high (positive) and low (negative) optical potentials. As usual, the thicknesses of the layers gradually increase from the substrate to the top layer.

One of the tasks in the supermirrors development is reaching maximum reflectivity for the smallest possible number of layers. Different methods for the optimization of the layer design to get the maximum reflectivity are described in [34, 35, 36, 37]. But in practice it is difficult to implement all the nuances of the method from publications. Thus, Ulrich Schmidt proposed to develop our own method for optimization the layer design.

The optimization algorithm is based on the program Supermref used for the calculation of neutron (x-rays) reflectivity and transmittivity of the multilayer structures

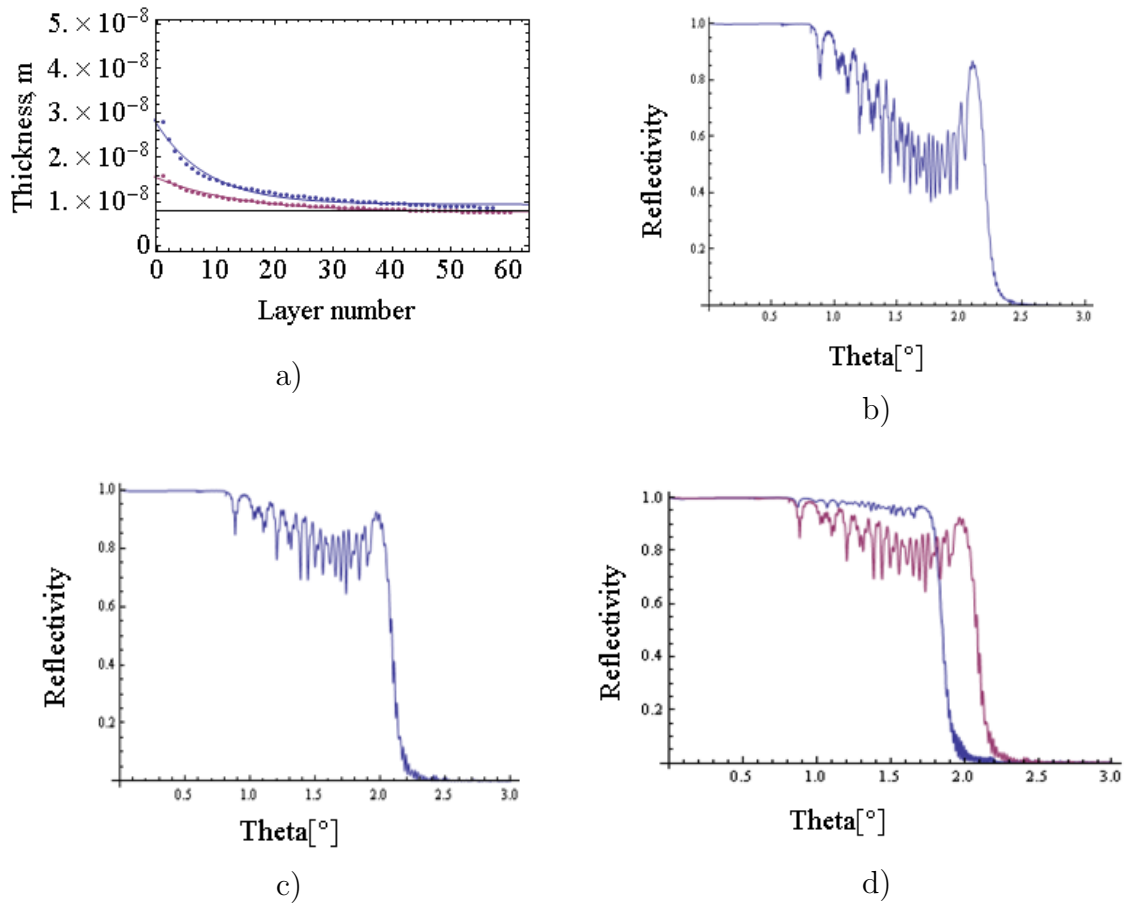


Figure 3.8: a) Layer thicknesses, Cu (blue points) and Ti (red points), calculated with Mezei and Dagleish formulas. Calculated neutron reflectivity for the Cu/Ti 119 multilayer sample: b) with layer design based on the F. Mezei and P. A. Dagleish formalism; c) with layer design based on the F. Mezei and P. A. Dagleish formalism and on the O. Schaerpf empirical improvement; d) with layer design based on the F. Mezei and P. A. Dagleish formalism, O. Schaerpf empirical improvement and the optimization procedure (blue) and layer design based on the F. Mezei and P. A. Dagleish formalism plus O. Schaerpf empirical improvement (red);

with rough interlayers. The optimization procedure (the procedure for the optimization of layer design of the Cu/Ti 119 layer sample with  $m=1.8$  is presented in Appendix C) searches for a maximum in a reflectivity function of several variables. The variables in the reflectivity function describe the sequence of layers. Exponential functions,  $d_{Cu}(x) = c_1 + c_2 \text{Exp}[-c_3 x]$  and  $d_{Ti}(x) = t_1 + t_2 \text{Exp}[-t_3 x]$ , were used to describe the sequence of Cu and Ti layers in a supermirror. The  $d_{Cu}(x)$  and  $d_{Ti}(x)$  are thicknesses of the Cu and Ti layers,  $x$  - the ordinal number of layer. We determined the initial parameters of variables for the starting searches for optimal parameters from F. Mezei and P. A. Dagleish formulas [25] proposed for Ni and Ti pair. The thicknesses of the Cu layer  $j$  and Ti layer  $j$  in a supermirror from  $N$  layers are:

$$d_{Cu}(j) = \frac{d(j)}{\sqrt{1 - \left(4 \frac{d(j)}{\lambda_{crit}(Cu)}\right)^2}}, \quad (3.2)$$

$$d_{Ti}(j) = \frac{d(j)}{\sqrt{1 - \left(4 \frac{d(j)}{\lambda_{crit}(Ti)}\right)^2}}, \quad (3.3)$$

$$d(j) = \frac{\lambda_c}{4 \sqrt[4]{\frac{N-j}{2}}}, \quad (3.4)$$

$$\lambda_c = \frac{1}{\sqrt{\frac{1}{\lambda_{crit}^2(Cu)} - \frac{1}{\lambda_{crit}^2(Ti)}}}. \quad (3.5)$$

The  $\lambda_{crit}(Cu)$  and the  $\lambda_{crit}(Ti)$  can be calculated by the following formulas (see Appendix A):

$$\lambda_{crit}^2(Cu) = \frac{\pi}{Pot_{re}(Cu)}, \quad (3.6)$$

$$\lambda_{crit}^2(Ti) = \frac{\pi}{Pot_{re}(Ti)}, \quad (3.7)$$

where  $Pot_{re}(Cu)$  and  $Pot_{re}(Ti)$  are the real parts of the optical potentials for Cu and Ti. In Fig. 3.8 a) one can see the Cu and Ti thicknesses calculated following F. Mezei and P. A. Dagleish formalism and the exponential curves described the layers behavior. The thicknesses of the top two Cu layers are too high and are badly described by the exponential curves. So two additional parameters were taken in the optimization procedure for these layers. The next pictures in Fig. 3.8 illustrate intermediate steps in the optimization procedure. Calculations performed for neutrons with wavelength 10 Å. The reflectivity curve calculated for the Cu/Ti supermirror with 119 layers

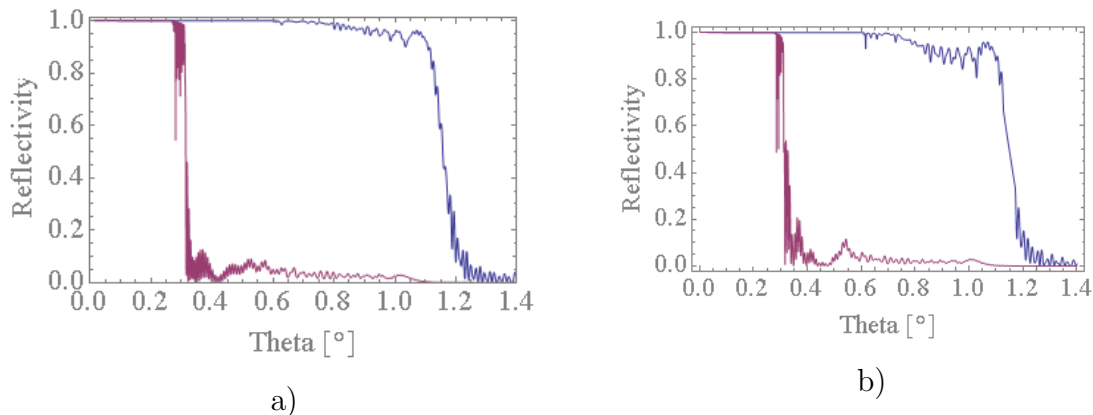


Figure 3.9: Calculated reflectivity curves for spin-up neutrons (blue) and for spin-down neutrons (red) of Fe/Si supermirrors with  $m = 2$  as function of angle, neutron wavelength is  $5.3 \text{ \AA}$ : a) 129 Fe/Si layers; b) 109 Fe/Si layers;

using the layer design of F. Mezei and P. A. Dagleish is presented in Fig. 3.8 b). During development of supermirror coatings O. Schaerpf observed that if  $\lambda_c$  is higher than it is determined by formula 3.5, the reflectivity curve will be better [38], see Fig. 3.8 c). It was found out that for Ni/Ti pair  $\lambda_c = 668 \text{ \AA}$  instead of the calculated  $526 \text{ \AA}$ . We found out that for Cu/Ti pair we need to take  $\lambda_c = 820 \text{ \AA}$  instead of the calculated  $617 \text{ \AA}$ . Finally, the blue curve in Fig. 3.8 d) represent reflectivity obtained by applying the optimization procedure to the empirically improved layer thickness of F. Mezei and P. A. Dagleish.

The optimization procedure was also applied to get maximum reflectivity for the Fe/Si multilayer samples with  $m=2$ . It was supposed to use Fe/Si polarizer during the experiment at FRM II. The calculated reflectivity curves for the two spin components are shown in Fig. 3.9. The first Fe/Si supermirror consists of 129 Fe and Si layers and the second sample consist of 109 layers, the lists with the optimal layer thicknesses are given in Appendix D and Appendix E. The supermirror sample with 109 Fe/Si layers has the smaller reflectivity for the region of Bragg reflection but larger thickness of the layers (during sputtering it is easier to control the thickness of thick layers). The roughness for Fe/Si pair was not investigated. It was assumed for the optimization procedure that roughness of the top Si layer is  $3.5 \text{ nm}$ . Thorsten Lauer produced Fe/Si supermirror with 109 layers. The experimental curves measured at TREFF reflectometer for the neutron wavelength  $4.78 \text{ \AA}$  in Munich for the two spin states show a good agreement with the calculated curves, Fig. 3.10. The dip of the reflected

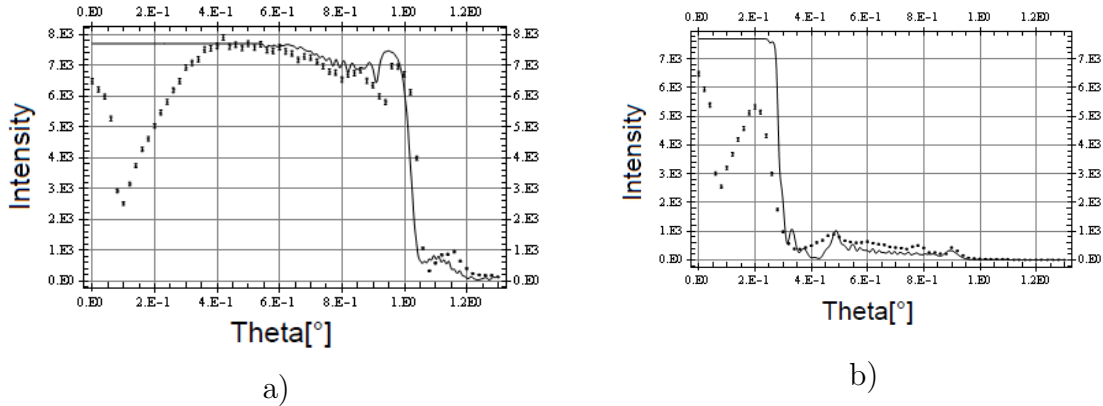


Figure 3.10: Experimental data and calculated reflectivity curves for spin-up a) and for spin-down b) neutrons obtained with Fe/Si supermirrors with  $m = 2$  (with 109 layers) as function of angle, neutron wavelengths is 4.78 Å.

intensity for incident angles less than  $0.4^\circ$  is typical for small angles and explained by bad alignment of the reflectometer.

### 3.1.7 Production of Cu/Ti supermirrors with $m = 1.2$

Chronologically, the Cu/Ti sample with  $m=1.2$  was produced before the time period when the multilayer Cu/Ti structures were investigated in order to define the inter-layer roughness and define the optimal sputtering conditions for Cu/Ti pair. We got opportunity to measure a sample at the reflectometer of polarized neutrons at Grenoble and decided to produce the sample (perhaps with not good reflectivity curve for neutrons) for the determination of the magnetic properties of the Cu/Ti multilayer covering. Sputtering conditions and layer composition for production of the Cu/Ti sample with  $m=1.2$  is presented in Table F.1 of Appendix F. I will describe in the section 3.2 the depolarization measurement with this sample, performed in November 2011. The reflectivity curve of the Cu/Ti ( $m=1.2$ ) sample was measured by Thierry Bigault at the reflectometer of the Neutron Optics lab, Grenoble. The wavelength of the incident neutron beam was 7.5 Å. As we expected the experimental reflectivity curve in Fig. 3.11 b) was not consistent with the calculated reflectivity curve in Fig. 3.11 a). Only the critical angles for the total external reflection matched. The experimental reflectivity was not higher than 80% for the region of total reflection and for the region of supermirror reflection.

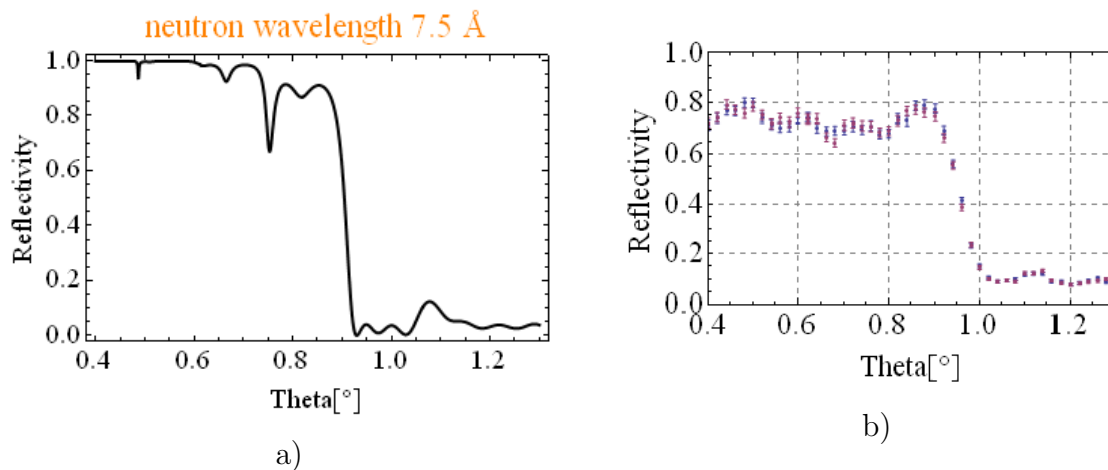


Figure 3.11: Reflectivity curve for the Cu/Ti multilayer sample with  $m=1.2$ : a) calculated for the neutron wavelength 7.5 Å; b) measured for the two spin states at the neutron wavelength 7.5 Å.

### 3.1.8 Production of Cu/Ti supermirrors with $m = 1.6$ and $m = 1.8$

The supermirror Cu/Ti covering with  $m=1.8$  and  $m=1.6$  were produced by the RF magnetron sputtering method at Heidelberg University. The coatings were deposited at the lowest possible working pressure,  $1 \cdot 10^{-3}$  mbar, that guarantees the less surface roughness. These samples were tested during the second depolarization measurement at FRM II (see section 3.3).

The optimal layer design of the Cu/Ti multilayers with  $m=1.8$  and  $m=1.6$  to get maximum reflectivity was done by using the optimization procedure. The optimized reflectivity curve for the neutron wavelength 5.3 Å are presented in Fig. 3.12. The list of the layer thicknesses and the sputtering conditions for the samples is given in Appendix G. After some time, checking everything what was done, I found a mistake in the thickness calibration of the sputtering machine for the last two samples with  $m=1.8$  and  $m=1.6$ . I deposited each copper layer 20% thicker than what was needed. The new reflectivity curves recalculated for the 20% thicker copper layers are shown in Fig. 3.13. For the new curves the reflectivity is slightly higher for the region of the supermirror reflection which is understandable because the roughness plays more powerful role (attenuates reflectivity) in the case of the thinner layers [39]. The systematic change in the thicknesses of the all Cu layers caused a decrease in the supermirror critical angle (such effect also explainable [40]). Thus the supermirror

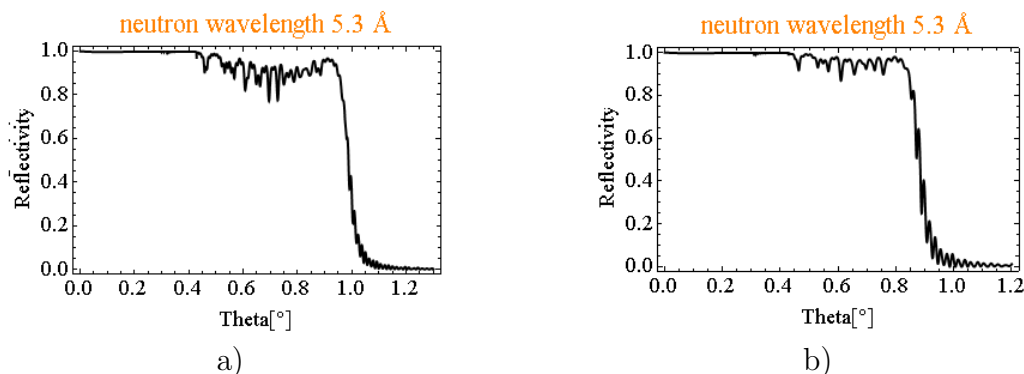


Figure 3.12: Optimized reflectivity curves for the neutron wavelength 5.3 Å: a) Cu/Ti multilayer,  $m=1.8$ ; b) Cu/Ti multilayer,  $m=1.6$ ;

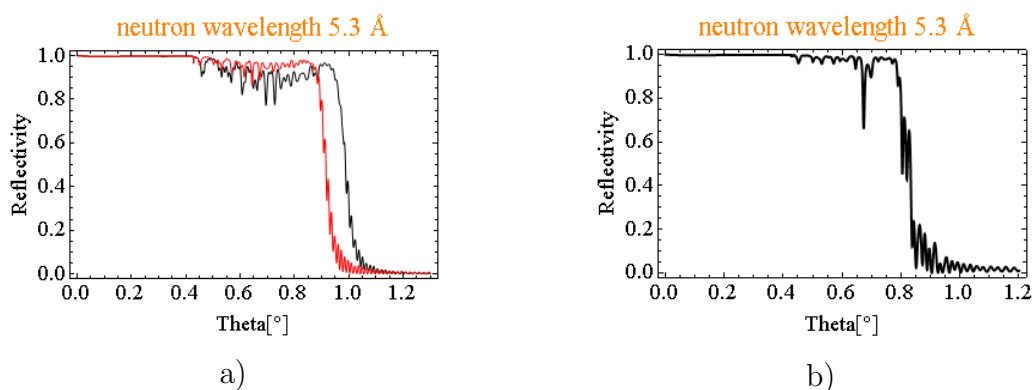


Figure 3.13: Optimized reflectivity curves for the neutron wavelength 5.3 Å: a) Cu/Ti multilayer,  $m=1.8$  (black curve); Cu/Ti multilayer,  $m=1.7$  (red curve), all Cu layers 20% thicker, than in multilayer characterized by black curve; b) Cu/Ti multilayer,  $m=1.6$ , all Cu layers 20% thicker, than it was planned. The fact, that the Ti target was partially open during deposition of the 45th layer is taken into account.

factor  $m$  for the sample with 119 Cu/Ti layers is 1.7 (instead of  $m=1.8$ ) and for the sample with 73 Cu/Ti layers  $m$  is 1.55 (instead of 1.6). During production of the Cu/Ti multilayer with 73 layers the Ti target was partially open for the deposition of the 45th layer. The reflectivity curve recalculated assuming that the layer 45 is one-half less than as calculated shown in Fig. 3.13 b). The dip of the reflectivity curve at the region of  $0.7^\circ$  is explained by this fact. Photos of the just sputtered Cu/Ti samples with  $m=1.7$  are shown in Fig. 3.14. These are glass plates with size of  $200\text{ mm} \times 40\text{ mm} \times 10\text{ mm}$  covered with the  $1.2\text{ }\mu\text{m}$  thick Cu/Ti composition. The reflectivity curves of the Cu/Ti samples ( $m=1.7$ ,  $m=1.55$ ) were measured at the TREFF reflectometer, FRM II, seven months after their deposition. The wavelength

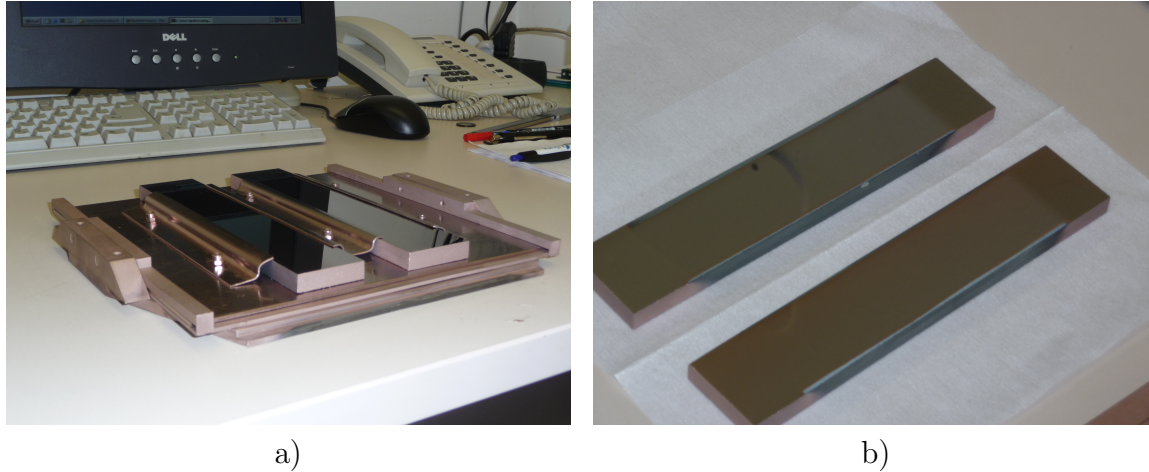


Figure 3.14: Photos of the sputtered Cu/Ti samples with  $m=1.7$ : a) fixed in the substrate-holder; b) on the table.

of the incident neutron beam was  $4.78 \text{ \AA}$ . The experimental curve for the sample with  $m=1.55$  is shown in Fig. 3.15 a) and the calculated reflectivity curve is shown in Fig. 3.15 b). As can be seen from the figure, the experimental and calculated curves significantly differ. The critical angles for total external reflection roughly coincide but reflectivity of the experimental curve for the region of Bragg reflection is low; it seems not only because of the error in the deposition of the 45th layer. The

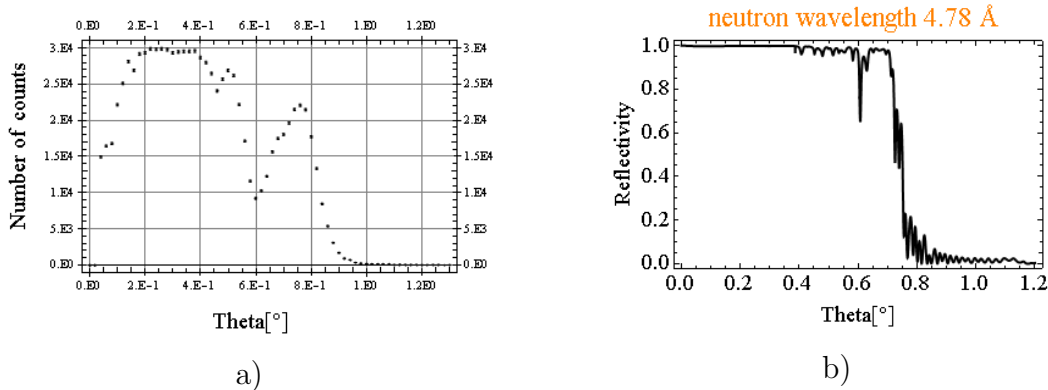


Figure 3.15: Reflectivity curves for the Cu/Ti multilayer sample with  $m=1.55$ : a) measured at TREFF reflectometer for the neutron wavelength  $4.78 \text{ \AA}$ ; b) calculated for the neutron wavelength  $4.78 \text{ \AA}$ .

measured reflectivity curves for the sample with  $m=1.7$  and Cu monolayer sample are presented together in Fig. 3.16 a) to demonstrate the gain in the critical angle for total external reflection achieved due to the multilayer structure (the critical angle for the

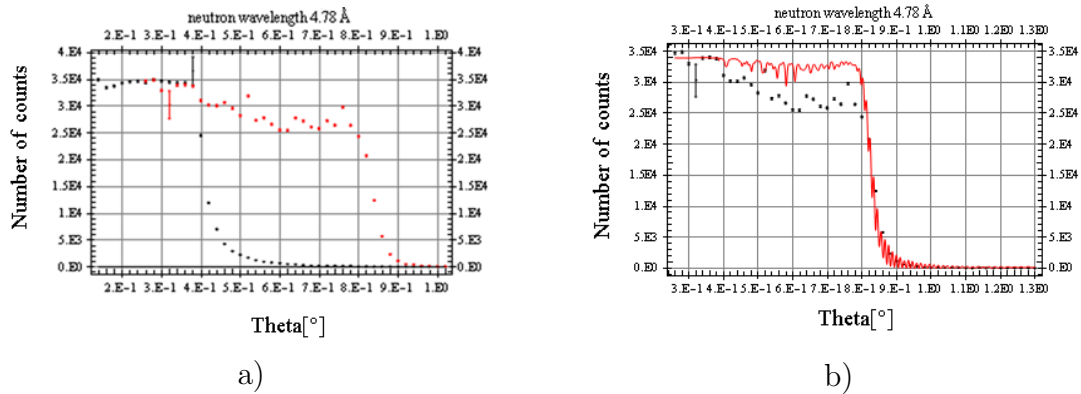


Figure 3.16: Reflectivity curves for the Cu/Ti multilayer sample with  $m=1.7$  and Cu monolayer sample measured at TREFF reflectometer for the neutron wavelength  $4.78 \text{ \AA}$ : a) Cu monolayer (black points), Cu/Ti multilayer (red points); b) experimental curve for the Cu/Ti sample with  $m=1.7$  (black points), calculated for the Cu/Ti sample with  $m=1.7$  (red curve).

Cu monolayer is  $0.4^\circ$ , the critical angle for the Cu/Ti 119 layers multilayer is  $0.85^\circ$  for the given neutron wavelength). The experimental reflectivity for the region of Bragg reflection is 20% below the calculated reflectivity curve which can be explained by the large interlayer roughness. Probably the interdiffusion plays a role here because Cu and Ti tend to interdiffuse. We did not investigate the interdiffusion process in the Cu/Ti multilayers. Usually for such studies the reflectivity curves are measured after annealing the samples at temperatures of hundreds of degrees. Upon analyzing the reflectivity curves of the samples annealed at different temperatures and different times, it is possible to get information about diffusion rate and diffusion depth. The common practices for preventing the interdiffusion in Ni/Ti supermirrors is to add C to the Ni layers. And, for further optimization, introduce nitrogen and oxygen into the Ni layers and alloy Ti with V (see overview [41] and the references cited therein [42, 43, 44]). It is clear that additional research on diffusion and roughness of Cu/Ti multilayers is required to get smoother and flatter layers for good reflectivity.

### 3.2 First depolarization measurement at ILL

The first depolarization measurement of the Cu/Ti multilayer sample with  $m=1.2$  was done in collaboration with our colleagues from the ILL (Institut Laue-Langevin)

in the autumn of 2011 at the PF1B instrument of the ILL high-flux reactor. The experiment was performed to investigate of neutron depolarization due to reflection off the polarizing Co/Ti and Fe/Si supermirrors [45]. The Cu/Ti sample had been measured with the same setup. The experimental setup is described in this chapter. The obtained depolarization values are shown and discussed.

### 3.2.1 Beam station PF1B at ILL

The international research reactor at the Institut Laue-Langevin provides the highest neutron flux on earth. The neutron source feeds about 40 state-of-the-art instruments. The PF1B instrument is mainly an experimental area for the installation of the spectrometers for the particle and nuclear physics experiments. The layout of PF1B is shown in Fig. 3.18.<sup>3</sup> The neutron guide shown on this figure is the first ballistic supermirror neutron guide H113 (m=2) that delivers neutrons from the liquid-deuterium filled vertical cold neutron source to the facility. The H113 of 72 m length was fabricated from Ni and Ti. The neutron capture flux density of H113 at its  $20 \times 6 \text{ cm}^2$  exit window is  $\Phi_C = 2 \cdot 10^{10} \text{ cm}^{-2} \text{ s}^{-1}$ . The maximum beam intensity is at the wavelength about 5 Å (Fig. 3.17) [46].

### 3.2.2 Experimental setup at PF1B

The reflectometer for the depolarization measurement of neutrons due to reflection of supermirror polarizers was built at the PF1B station. The velocity selector and collimating neutron guide are placed at the casemate of the PF1B. The rest of the setup is at the experimental zone of the PF1B. The experimental setup is based on the Opaque Test Bench. The Opaque Test Bench consist of two magic boxes which provide a homogeneous magnetic environment for polarized  $^3\text{He}$  cells. The schematic diagram and photos of the setup are shown in Fig. 3.19 and Fig. 3.20. The cold neutron beam of PF1B instrument was separated by the velocity selector (1) to a 5.3 Å. After passing the neutron guide (2) neutrons were polarized by the first  $^3\text{He}$  cell (4) and analyzed by the similar second  $^3\text{He}$  cell (6). The spin of the polarizing and analyzing  $^3\text{He}$  cell can be flipped via the fast adiabatic passage flipper. So by flipping the spin of the analyzing  $^3\text{He}$  cell the neutrons in the opposite spin state,

---

<sup>3</sup>From <http://www.ill.eu/>

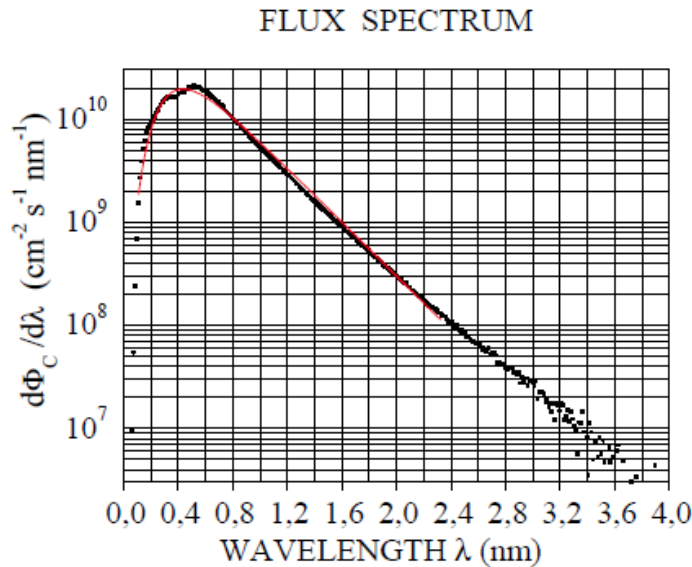


Figure 3.17: Experimental neutron spectrum (dots) and modeled (red line) of the H113 neutron guide at the PF1B instrument.

$N_-$ , to the state of the neutrons after the polarizer,  $N_+$ , can be transmitted. The resulting polarization is  $P = (N_+ - N_-)/(N_+ + N_-)$ . The neutrons were registered by movable  ${}^3\text{He}$  detector (7). The sample was adjusted at a half of its critical angle,  $\theta_{cr}/2$ , and placed inside the strong magnetic field  $0.8\text{ T}$  of the electromagnet (5). The background measurement we performed with the closed shutter (3). The adiabatic conditions for the transport of certain neutron spin state along the neutron flight pass were fulfilled. The next sections describe the basic elements of the setup.

### 3.2.3 Neutron velocity selector

The depolarization measurement of Cu/Ti sample was performed with the monochromatic neutron beam of wavelength  $5.3\text{ \AA}$ . The neutron spectrum of the PF1B instrument (Fig. 3.17) was selected to the desired wavelength by Dornier velocity selector (Astrium GmbH (formerly Dornier), a company of the Daimler Group).

A velocity selector is a rotating cylinder with the helical slots. The surface of the helical slots covered with neutron absorbing material  ${}^{10}\text{B}$ . By varying the rotation frequency of the selector we can choose the wavelength of the neutrons which pass

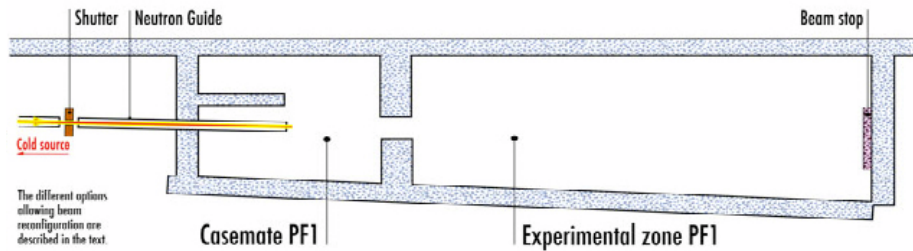


Figure 3.18: The layout of PF1B instrument at the ILL, Grenoble.

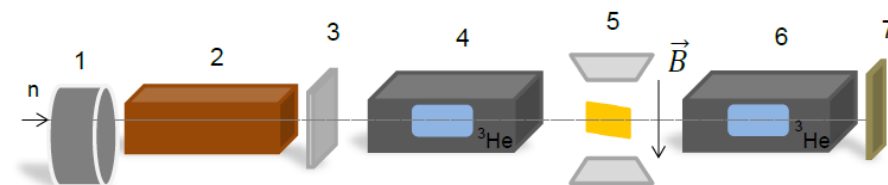


Figure 3.19: Schematic diagram of the setup at PF1B instrument, ILL. (1) Velocity selector, (2) neutron guide, (3) shutter, (4) first magic box with  $^3\text{He}$  cell - polarizer, (5) sample inside the electromagnet, (6) second magic box with  $^3\text{He}$  cell - analyzer, (7) detector.

the helical way. The neutrons that are too fast or too slow will be absorbed by boron. The rotor of the selector and the neutron wavelength resolution after selector are shown in Fig. 3.21. Some characteristics of the velocity selector are listed below <sup>4</sup>:

- rotor diameter: 290 mm;
- rotor length: 250 mm;
- number of the blades: 72;
- selector speed range: 3000 – 28300 rpm;
- speed constancy: 0.2%
- neutron wavelength transmitted region: 0.45 – 4.3 nm;

<sup>4</sup>Characteristics and pictures are taken from <http://www.sii.co.jp>.

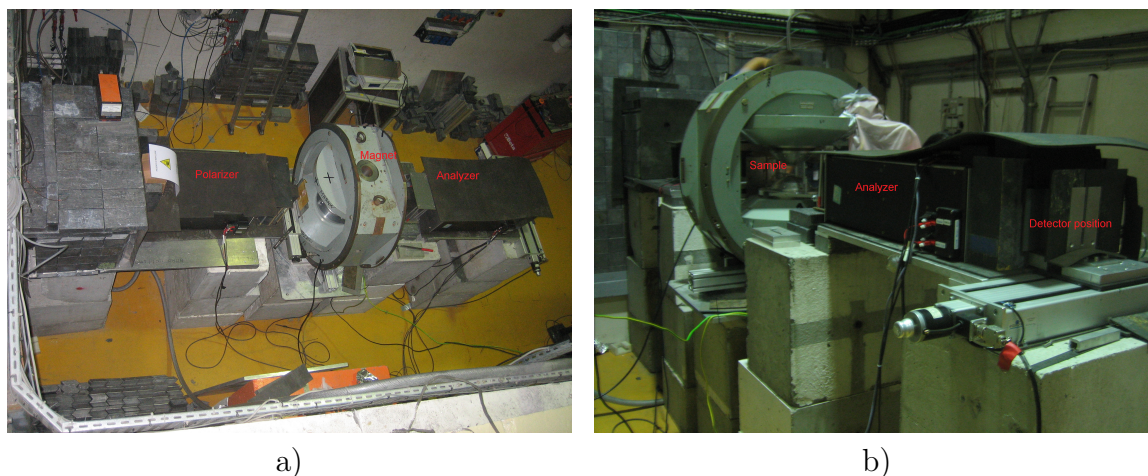


Figure 3.20: Photos of the setup at the PF1B instrument, ILL: a) from the top; b) from the detector side.

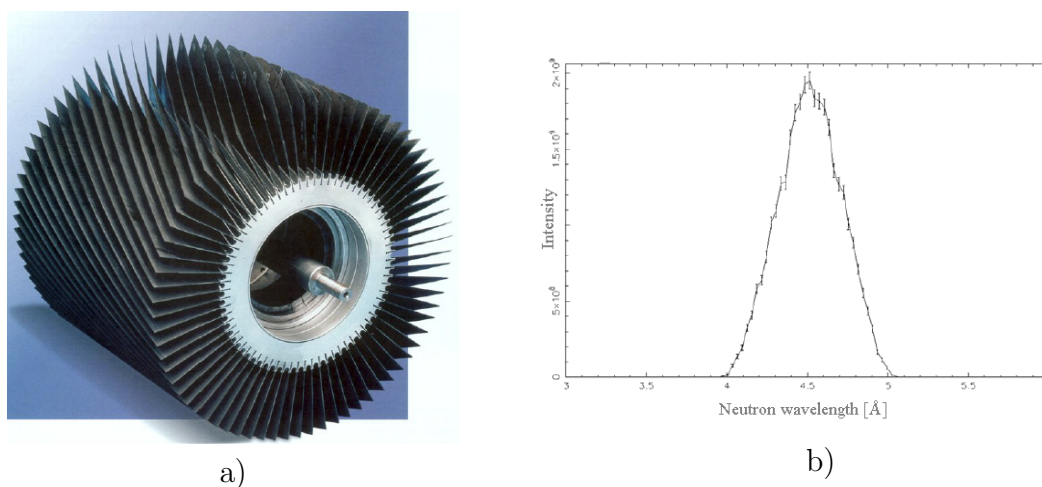


Figure 3.21: Dornier velocity selector: a) selector turbine, the blades covered with  $^{10}\text{B}$ ; b) neutron wavelength resolution after selector.

- neutron wavelength resolution:  $\Delta\lambda/\lambda \sim 10\%$ .

### 3.2.4 Opaque Test Bench

The basic element of the reflectometer at the PF1B beam station is the Opaque Test Bench [2]. The Opaque Test Bench is a tool for the neutron polarization analysis with precision  $10^{-4}$ . The Test Bench consist of two  $^3\text{He}$  cells. The  $^3\text{He}$  cells polarize and analyze neutrons over the wide spectrum from cold to hot neutrons. The polarized  $^3\text{He}$  with high probability absorbs the oppositely polarized neutrons of the incident

beam and transmits the collinearly polarized neutrons with moderate attenuation. The transmission  $T$  through the polarized helium cell of length  $l$  for the neutron spin component parallel “+” and antiparallel “-” to the  ${}^3\text{He}$  spin is:

$$T_{\pm} = \frac{1}{2} \exp(-N_{\text{He}} l \sigma_0 (1 \mp P_{\text{He}})), \quad (3.8)$$

where  $N_{\text{He}}$  is the  ${}^3\text{He}$  number density,  $P_{\text{He}}$  is the helium polarization, and the total unpolarized capture cross section  $\sigma_0$  is given by  $\sigma_0[b] \simeq 3000 \cdot \lambda [\text{\AA}]$ . The resulting polarization  $P_n$  of the neutrons with wavelength  $\lambda$  passing the helium cell is defined by:

$$P_n(\lambda) = \frac{T_+ - T_-}{T_+ + T_-} = \tanh(OP_{\text{He}}), \quad (3.9)$$

where  $O(\lambda) = N_{\text{He}} l \sigma_0(\lambda)$  is a filter opacity and for gaseous  ${}^3\text{He}$  may be expressed by  $O = 0.0733 \cdot O'$  with  $O' = p[\text{bar}]l[\text{cm}]\lambda[\text{\AA}]$ , and  $p$  is the  ${}^3\text{He}$  gas pressure at  $20^\circ\text{C}$  [47]. The polarization of the helium atoms is reached by the direct optical pumping technique up to the final  ${}^3\text{He}$  polarization of 70 – 75 % at about 1 *mbar* pressure. Then the gas is compressed up to a pressure of several bars. The initial polarization of helium atoms  $P_0$  exponentially decreases with a time constant  $T_1$ :

$$P_{\text{He}}(t) = P_0 \exp(-t/T_1). \quad (3.10)$$

The cell “He03” ( $T_1 = 242$  h) and the cell “D22” ( $T_1 = 140$  h) with the pressure of 1.7 *bar* and the initial helium spin polarization 75 % were used for the measurements of the Cu/Ti sample at the PF1B. To minimize the helium polarization loss due to the magnetic field inhomogeneity and to moderate stray fields the  ${}^3\text{He}$  cell is placed in the magnetostatic cavity, “Magic box”. The “Magic box” is a magnet which generates a weak magnetic field of around 10 *G* in a large volume of the helium cell with no saturation in the magnetic circuit. In Fig. 3.22 the concept of the “Magic box” is shown. The left and right walls of the box are made from soft iron and are surrounded by DC coils dedicated for the magnetic field generation. The top and bottom walls are made from  $\mu$ -metal and serve to provide a homogeneous magnetic field  $\vec{B}$ . The  ${}^3\text{He}$  cell is installed to the center of the magnetostatic cavity. The picture of the “Magic box” and some information on it are taken from [48]. The flip of the helium polarization in the cell happens in the “Magic box” via adiabatic fast passage flippers. In these flippers weak oscillating RF magnetic field is applied at the right angle with

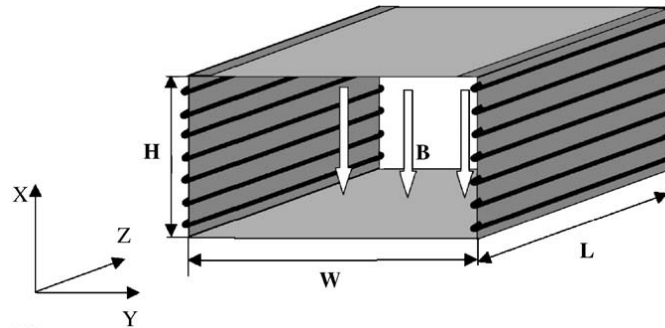


Figure 3.22: The “Magic box” concept.

the guiding magnetic field. The frequency of the RF field is chosen match the Larmor frequency of neutron precession in the guiding field. Such method works effectively for the stable guiding magnetic field and for the monochromatic neutron beam.

### 3.2.5 Depolarization for Cu/Ti multilayer sample with $m=1.2$

We performed the polarization measurement of the neutron beam which was reflected from the magnetized Cu/Ti sample ( $m=1.2$ ). The magnetizing field was varied from  $0.02 T$  to  $0.82 T$ . To determine depolarization effect due to reflection off the magnetized mirror we compared the measurement with a sample and the direct beam polarization measurement. The neutron incident angle on the sample was adjusted to about  $0.3^\circ$  that is 50% of the respective critical angle for Cu/Ti sample with  $m = 1.2$ . During measurement we first made a scan with the helium detector along the axis perpendicular to the neutron pass in order to find the position of the beam reflected and passed through the sample. Fig. 3.23 shows such scans with the different width of the detector aperture and step. Intensity in the region of 230 – 235 mm of the first scan corresponds to the neutrons passed through the sample and through the sides of it. Intensity in the region of 240 – 250 mm corresponds to the neutrons reflected from the sample. The distortion of the shape of the reflected peak in Fig. 3.23 a) is due to the bending of the investigated sample in the sample holder. After detecting the peaks, the detector with the aperture of 11 mm width was fixed at the position of the reflected peak. Measurements were taken in the following regime: 1) the helium polarization in the both cells are parallel and the detector registers the neutrons which polarized collinear to the first cell ( $N_+$  neutrons); 2) the helium polarization

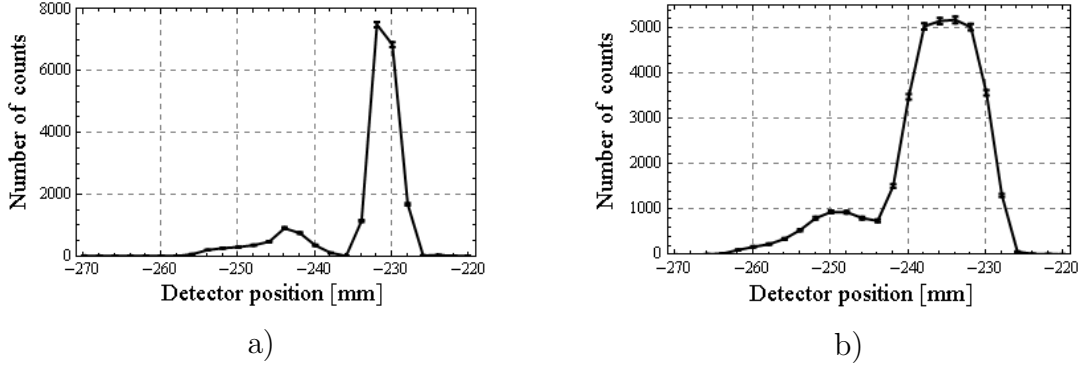


Figure 3.23: Measurement with Cu/Ti multilayer sample ( $m=1.2$ ): a) scan with the 2 mm detector aperture, in step 2.5 mm; b) scan with the 11 mm detector aperture, in step 2 mm;

in the both cells are anti-parallel and the neutrons polarized non-collinear to the first cell are detected ( $N_-$  neutrons). Polarization of the neutrons passing via system is a product of the polarizing power  $P$  and the analyzing power  $A$  in the measurement with the sample  $S$ :

$$A \cdot S \cdot P = \frac{(N_+ - N_+^{bgr}) - (N_- - N_-^{bgr})}{(N_+ - N_+^{bgr}) + (N_- - N_-^{bgr})}. \quad (3.11)$$

In the polarization measurement without a sample the detector was fixed at the position of the direct beam. The polarization of the direct beam, product of the polarizing power  $P$  and the analyzing power  $A$ , is determined in the same way:

$$A \cdot P = \frac{(N_+ - N_+^{bgr}) - (N_- - N_-^{bgr})}{(N_+ - N_+^{bgr}) + (N_- - N_-^{bgr})}. \quad (3.12)$$

The background neutrons  $N_+^{bgr}$  and  $N_-^{bgr}$  were registered with the closed shutter, see Fig. 3.19. The direct beam polarization values ( $A \cdot P$ ), the polarizations measured with the sample ( $A \cdot S \cdot P$ ), the ratios between these measurements at different magnetic field strength are shown in Table 3.1 and Table 3.2. The same polarization data is represented in Fig. 3.24. As it is visible from the polarization data obtained with and without the sample, there is no depolarization effect at  $10^{-4}$  level caused by reflection of the polarized neutrons with the energy around  $5.3 \text{ \AA}$  from magnetized Cu/Ti multilayer sample ( $m=1.2$ ).

Table 3.1: Polarization measured with the direct beam and with the Ci/Ti sample ( $m=1.2$ ),  ${}^3\text{He}$  cells after 20 hours from their installation.

Magnetic field, T	AP value (without sample)	ASP value (with sample)	Ratio ASP/AP
0.02	$0.99973 \pm 0.00003$	$0.99956 \pm 0.00008$	$0.99983 \pm 0.00011$
0.53		$0.99967 \pm 0.00007$	$0.99994 \pm 0.00009$
0.82		$0.99975 \pm 0.00006$	$1.00002 \pm 0.00008$

Table 3.2: Polarization measured with the direct beam and with the Ci/Ti sample ( $m=1.2$ ),  ${}^3\text{He}$  cells right after their installation.

Magnetic field, T	AP value (without sample)	ASP value (with sample)	Ratio ASP/AP
0.02	$0.99988 \pm 0.00001$	$0.99980 \pm 0.00003$	$0.99993 \pm 0.00004$
0.53		$0.99979 \pm 0.00003$	$0.99992 \pm 0.00004$
0.82		$0.99982 \pm 0.00003$	$0.99994 \pm 0.00004$

### 3.3 Second depolarization measurement at FRM II

As it was described in the previous part, in the first depolarization measurement we observed no depolarization effect (with a limit below  $10^{-4}$ ) during reflection of the polarized neutrons from the magnetized multilayer Cu/Ti sample ( $m = 1.2$ ). To investigate Cu/Ti samples with  $m = 1.55$ ,  $m = 1.7$  and Ni(Mo)/Ti sample with  $m = 1.5$  we performed the second depolarization measurement at the FRM II (Forschungs-Neutronenquelle Heinz Maier-Leibnitz). The experiment was done in the spring of 2013 year Mephisto beam station.

In this chapter I will describe the second depolarization test of the non-magnetic Cu/Ti and the non-magnetic Ni(Mo)/Ti multilayer coverings performed at the reflectometer of polarized neutrons. I will present the depolarization values for both samples, Cu/Ti and Ni(Mo)/Ti. I will discuss the advantages and disadvantages of the coatings and will draw conclusions about the feasibility of using the alternative Cu/Ti non-magnetic coating instead the traditional Ni(Mo)/Ti.

To determine depolarization due to the reflection from the magnetized sample we measured the polarization of the neutron beam, which passed the spectrometer with

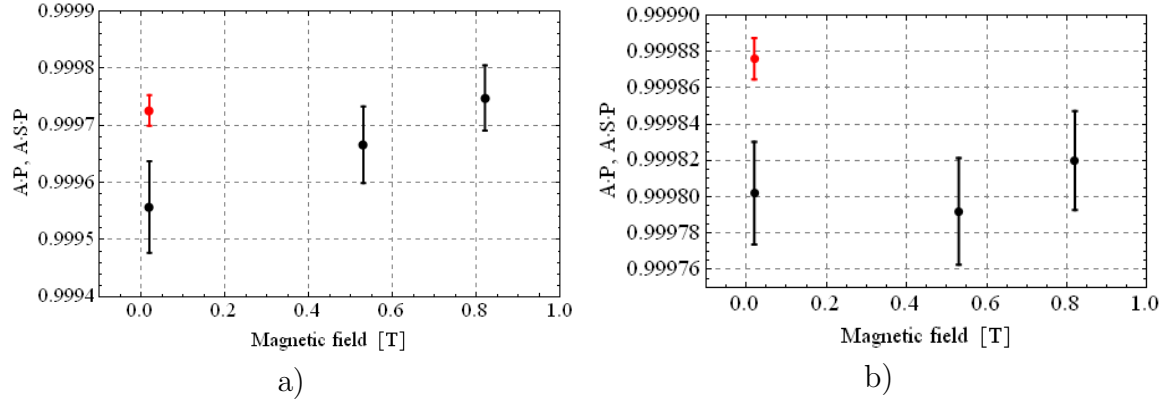


Figure 3.24: Polarization measurements of the direct beam (red) and the Cu/Ti multilayer sample with  $m=1.2$  (black): a)  ${}^3\text{He}$  cells after 20 hours from their installation; b)  ${}^3\text{He}$  cells right after their installation;

and without reflection from the investigated sample. The polarization values of the direct beam and the reflected beam were obtained using measurements of the neutron intensities for the two spin flipper states, “flipper on” and “flipper off”.

### 3.3.1 Experimental setup at Mephisto

Before description of the setup on which we performed the measurement I want to note that originally, the experiment was planned with the superconducting magnet PERKINO. The magnet generates a longitudinal magnetic field up to 2 T. The diameter of the channel for a sample loading is 6 cm, and the length is 40 cm. Such dimensions would allow us to have the neutron beam reflected twice from the magnetized mirror and keep the analyzer angle the same as in the measurement of the direct beam (without reflection from the investigated sample). The analyzing power of the supermirror analyzer strongly depends on the wavelength and the incident neutron angles at the analyzer. Thus a tiny shift of the analyzer angle can cause artificial depolarization of the neutron beam. You can see the scheme of the planned experiment in the Fig. 3.25 a). Unfortunately during the first test at the beam site the superconducting magnet was broken. Because of the limited beam time and the difficulty to get a new superconducting magnet it was decided to use the available electromagnet with the transverse magnetic field up to 1.3 T. The diameter of the region inside the electromagnet with the desired magnetic field was around 5 cm which is not enough to have the two reflections off the sample in the strong magnetic field.

Thus it was agreed to carry out the experiment with one reflection from the sample and try as best as possible to reproduce the analyzer settings for all measurements.

So the special reflectometer was built and optimized for measuring the small depolarization ( $10^{-4}$ ). During measurement the samples were placed in the strong magnetic field  $1.3 T$  and fixed at the certain angle to the incident beam. The wavelength of the neutron beam was  $3 - 8 \text{ \AA}$ . The neutron intensity was registered depending on the neutron wavelength by the time of flight (TOF) method. The schematic diagram of the TOF reflectometer and the neutron pass within the spectrometer is given in Fig. 3.25 b). Photos of the experimental setup are shown in Fig. 3.26 and Fig. 3.27.<sup>5</sup> The neutrons, coming from the neutron guide, with wavelength larger than  $8 \text{ \AA}$  are filtered out from the incident beam by a Cu filter. The neutron chopper for transforming the continuous neutron beam to a pulsed one is located directly behind the Cu filter. All of the main measurements were done at a chopper frequency of  $40 \text{ Hz}$ . The unpolarized neutrons hit the polarizing supermirror, placed in the transverse magnetic field, after passing the neutron chopper. Only the neutrons polarized along the external magnetic field are reflected from the polarizer and transmitted further. A similar supermirror, magnetized in the same direction as the polarizer, was used for analysis of these neutrons. The analyzing supermirror (analyzer) reflects neutrons with the polarization parallel to the external magnetic field. For determination of the neutron polarization  $P = (N_+ - N_-)/(N_+ + N_-)$  it is required to know the number of neutrons polarized along the magnetic field  $N_+$  and opposite to the magnetic field  $N_-$ . The neutrons with polarization antiparallel to the external magnetic field should reverse their polarization behind the polarizer to be registered. Therefore the  $N_+$  neutrons we detect during the spin “flipper off” mode. The  $N_-$  neutrons is registered during the spin “flipper on” mode. In the measurements of the polarization of neutrons, reflected by the studied sample, the sample was placed in the electromagnet. The following sections describe the elements of the installation.

### 3.3.2 Beam station Mephisto at FRM II

The FRM II is a German research neutron source. It is located at Garching research campus (18 km in the north of Munich). FRM II belongs to Technische Universität

---

<sup>5</sup>All photos are made by Jens Klenke.

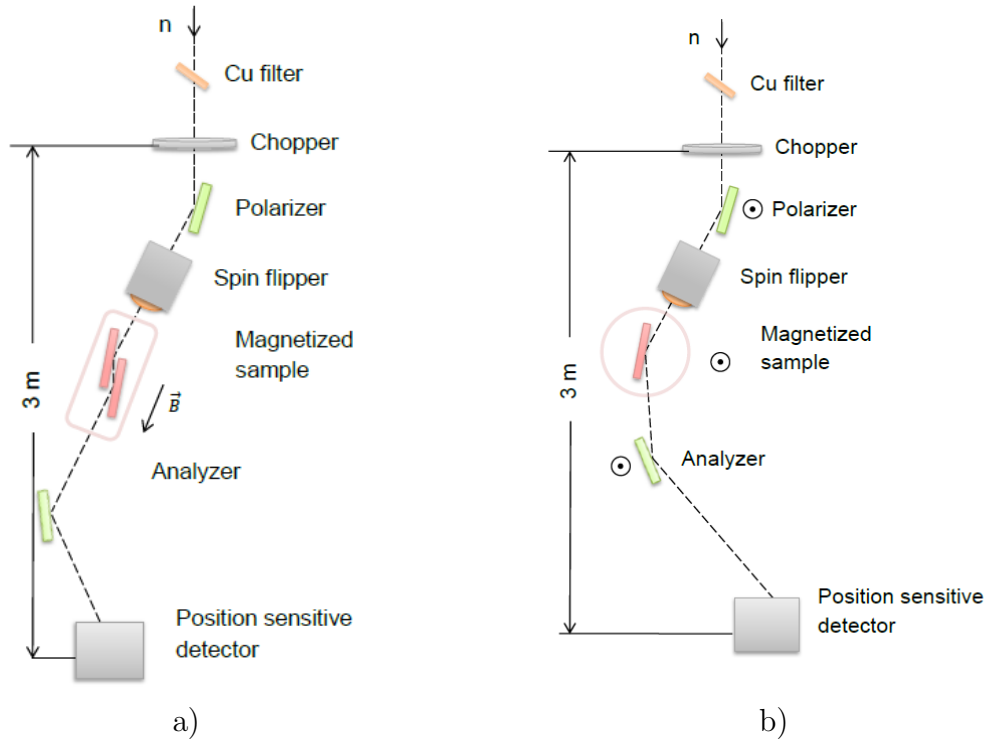


Figure 3.25: Schematic diagram of the TOF reflectometer of the polarized neutrons at Mephisto, FRM II: a) originally planned setup; b) realized setup.

München (TUM). It is operated five cycles per year. The cycle length is about 50 days. The nominal thermal power of the reactor core is 20 MW.<sup>6</sup>

The compact reactor core contains a single cylindrical fuel element, which installed in the centre of a moderator tank (2.5 m in diameter and 2.5 m high) filled with heavy water. The moderator tank is placed in the reactor pool (internal diameter about 5 m) with light water for cooling. The maximum thermal neutron flux density (undisturbed  $8 \cdot 10^{14} \text{ cm}^{-2} \text{ s}^{-1}$ ) is at a distance of 12 cm from the surface of the fuel element. This neutron flux is utilized for experiments by a series of beam tubes and various vertical irradiation channels. The experimental stations are located in the experimental hall and on neutron guides in the neutron guide hall.

Mephisto is the measuring facility for particle physics with cold neutrons. It was located at the cold neutron guide NL-1 in the Neutron Guide Hall West of FRM II. Fig. 3.28 shows experimental neutron spectrum of the NL-1 at Mephisto.

Recently the experimental area Mephisto was moved from the Neutron Guide Hall

<sup>6</sup>From [http://en.wikipedia.org/wiki/Forschungsreaktor\\_München\\_II](http://en.wikipedia.org/wiki/Forschungsreaktor_München_II)

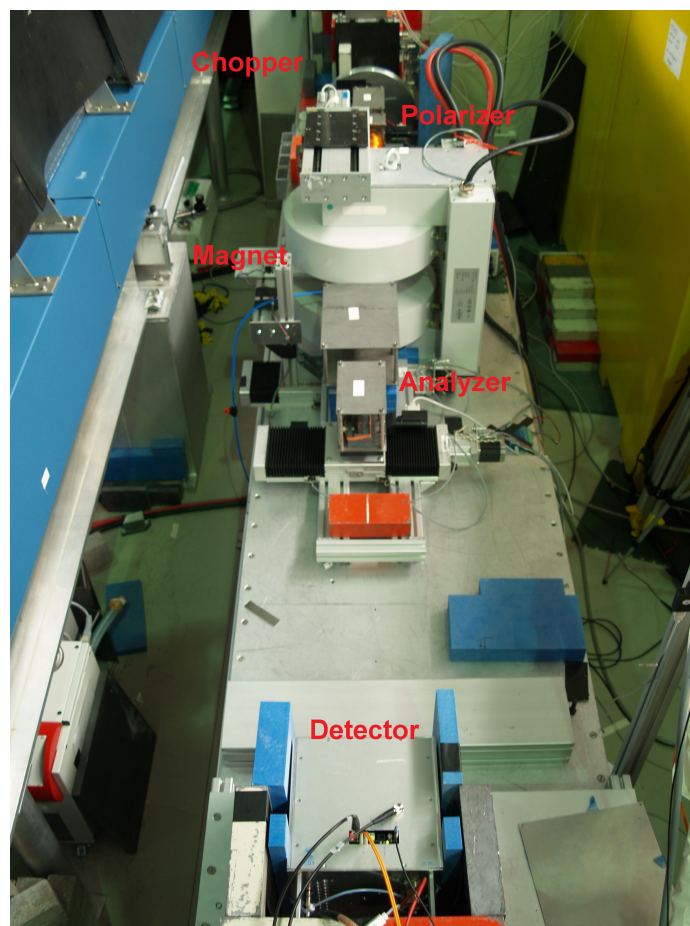


Figure 3.26: Photo of the TOF reflectometer of the polarized neutrons at Mephisto, FRM II.

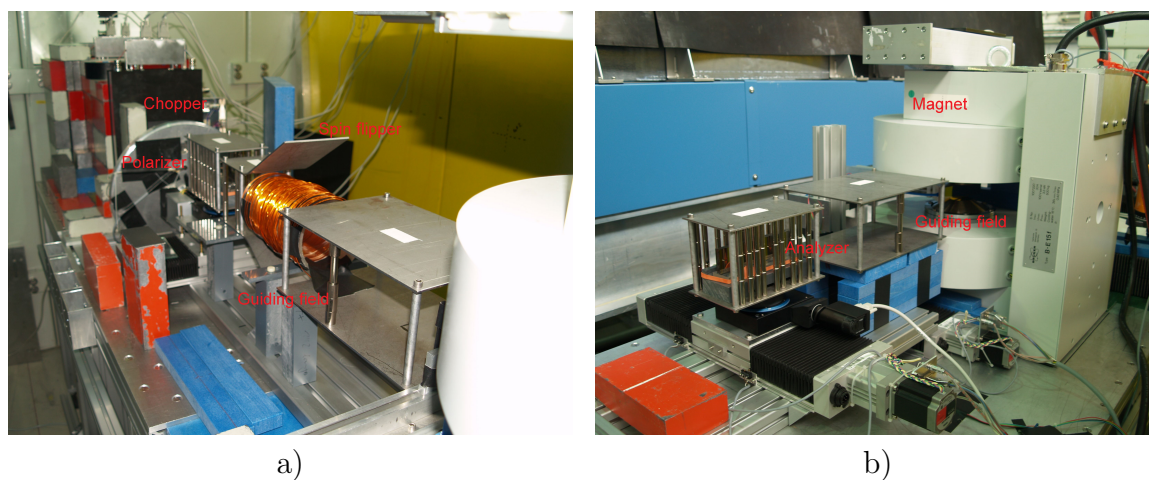


Figure 3.27: Photos of the TOF reflectometer of the polarized neutrons at Mephisto: a) from the detector side; b) from the beam side.

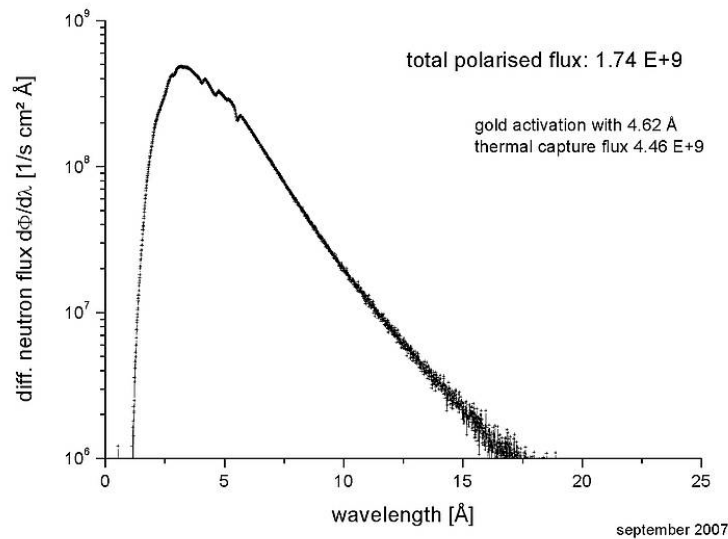


Figure 3.28: Experimental neutron spectrum of the NL-1 neutron guide at the Mephisto beam station.

West to the Neutron Guide Hall East. It is planned to set up the instrument PERC at the Mephisto beam station during the first years of operation.<sup>7</sup>

### 3.3.3 Neutron chopper. Realization of measurement by time of flight method

The wavelength of neutrons, irradiating the investigated sample, was selected by using the TOF method. In a TOF measurement, the release time of neutrons from the source and the time when neutrons reach the detector are registered. The neutron speed, energy and wavelength can be determined by measuring the distance between the detector and the source.

Mephisto neutron guide provides a continuous neutron beam with a maximum intensity at 5 Å, see Fig. 3.28. A pulsed neutron beam is needed for realization of a time of flight measurement.

For the generation of a pulsed neutron beam we used the mechanical chopper. This is rotating device which transmits neutrons for the short time (tens of microseconds

<sup>7</sup>From [http //www.mlz-garching.de/mephisto](http://www.mlz-garching.de/mephisto)

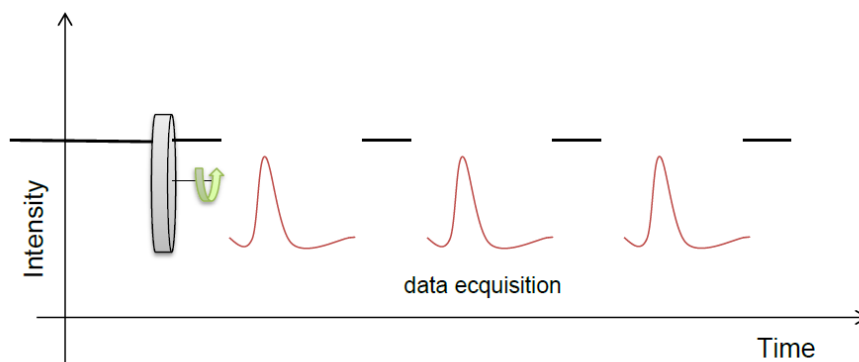


Figure 3.29: Illustration of work of neutron chopper.

in present experiment) and blocks for the rest of the time (tens of millisecond). The neutron TOF spectrum (number of neutron counts depending on time of flight of the fixed distance from the chopper to the detector) is recorded between the pulses. The scheme in Fig. 3.29 illustrates work of a chopper. The neutron pulse of a few microseconds duration (immediately after copper) expands to the millisecond interval by time of flight. The neutron chopper was built by group from Mainz University [49]. The chopper consists of three basis parts. First is the aluminum housing of 40 *cm* diameter and of 3.5 *cm* thickness with two holes for neutrons transmission. The second is the rotating aluminum disk of 30 *cm* diameter and of 2 *mm* thickness. The one side of the disk is covered with 0.1 *mm* of gadolinium, neutron absorbing material. There are two symmetric slits on the disk. The third part is the brushless DC (direct current) electric motor for neutron chopper operation. The motor can support the chopper rotating frequency up to 100 *Hz*.

The work of the neutron detector is synchronized with the chopper. The TTL (transistor-transistor logic) starting signal from the chopper starts the time of flight measurement, which is interrupted in fixed time (sweep time). The photo diode (sensor element), placed on the housing, registers the light from the light-emitting diode (LED-light source), placed on the disk, when slits appears and generates the TTL starting signal for detection. One of the two slits on the chopper disk is broken, so for analysis we used the neutrons from the first burst of a chopper cycle (region of 5 – 10 *ms* in Fig. 3.30). Connection between the neutron time of flight of its pass

and neutron pass is  $t = 72.3 \cdot L\sqrt{1/E}$ , where  $E$  is neutron energy in mega electron volts,  $t$  is in nanoseconds,  $L$  is in meters. The expression for neutron wavelength is  $v[m/s] = 3955/\lambda [\text{\AA}]$ , where  $v$  is neutron speed. To control the stability of chopper frequency, the detector was operated in “brake mode”. At each chopper cycle the data acquisition stopped in a certain time interval, which is less than whole sweep time of detector. If the chopper frequency is stable the last few channels on the sweep time are empty.

The neutron chopper has an offset,  $\theta_{offset}$ , because the slit position on the chopper disk for the neutron transmission (real neutron source) does not coincide with the LED position (LED produces light signal, indicating that the neutron pulse has been emitted). Thus the TOF spectrum has a time offset,  $t_{offset}$ , which depends on the chopper frequency  $\nu$  in a given measurement. The time of flight of a neutron,  $t_{exp}$ , determined from the spectrum is composed of a real flight time,  $t_{real}$ , (same for any chopper frequency) and the offset time,  $t_{offset}$ , required for the rotation of the chopper on the  $\theta_{offset}$  angle between the LED and the chopper slit:

$$t_{offset} + t_{real} = t_{exp}. \quad (3.13)$$

To determine the chopper offset we perform TOF measurements at three different chopper frequencies: 33  $Hz$ , 36  $Hz$ , 40  $Hz$  (see Fig. 3.30). For instance, let’s consider the measurements with 40  $Hz$  and 36  $Hz$  and solve the system of equations Eq. 3.13 for them:

$$\begin{cases} \theta_{offset}/40.098 + t_{real} = 4.71 \cdot 10^{-3} \\ \theta_{offset}/36.11 + t_{real} = 5.16 \cdot 10^{-3}. \end{cases} \quad (3.14)$$

The values of the experimental time of flight,  $t_{exp}$ , in Eq. 3.14 are taken from the spectra in Fig. 3.30 a) (the fastest neutrons of the chopper pulse are at left edge of the TOF spectrum). The chopper offset is  $60^\circ$ . The value of the current chopper frequency is contained in each TOF file, so the stability of the chopper frequency can be checked. For example, in the depolarization measurement of the Cu/Ti sample with  $m = 1.55$ , 140 TOF files were written. Fig. 3.30 b) shows the chopper frequencies for the 140 TOF files. It is seen from the data, that the chopper frequency fluctuates within 0.2 % in a daily measurement. It corresponds to a tiny shift of the 0.3 time channel (per 52  $\mu s$  length) for TOF spectrum.

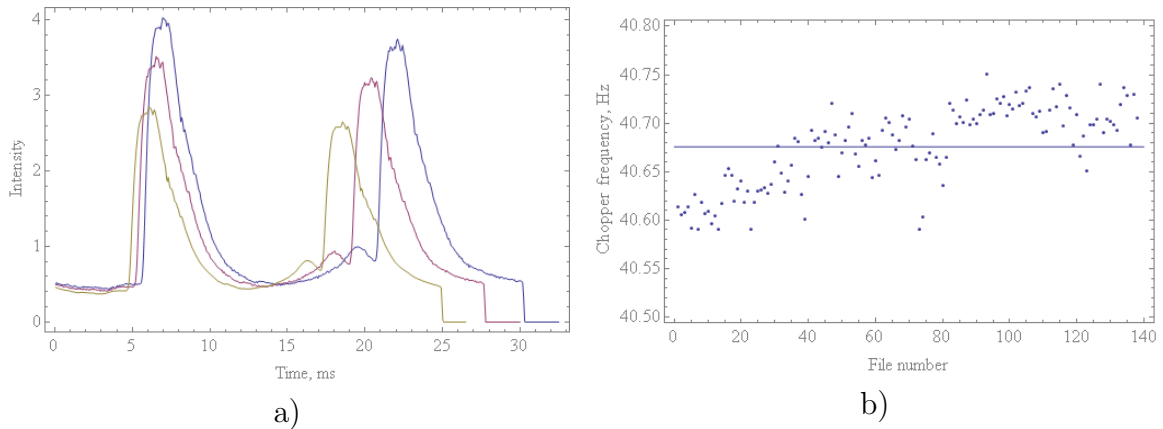


Figure 3.30: a) Time of flight spectra obtained at three chopper frequencies: 33  $Hz$  (blue), 36  $Hz$  (red), 40  $Hz$  (yellow); b) chopper frequency fluctuations during the depolarization measurement of Cu/Ti sample with  $m = 1.55$ .

### 3.3.4 Wavelength copper filter

The principle of operation of a ferromagnetic supermirror polarizer is based on the reflection of neutrons with spins parallel (“right” spin component) to the external magnetic field and transmission of neutrons with spins antiparallel (“wrong” spin component) to the magnetic field. But neutrons (mostly long wavelength) with “wrong” spin component have a nonzero probability to be reflected from the ferromagnetic surface therefore decreasing the polarizing efficiency of the mirror for long wavelengths. Fig 3.31 shows example of the calculated reflectivity curves of a Fe/Si supermirror with  $m = 2$  for spin-up neutrons as well as polarization as a function of angle for wavelengths between 5  $\text{\AA}$  and 10  $\text{\AA}$ . It is seen that for fixed incident angle (for example  $1^\circ$ ) the polarization of neutrons with wavelength a of 5  $\text{\AA}$  is better than for neutrons with a wavelength of 10  $\text{\AA}$ . The copper filter which removes neutrons with a wavelength above 10  $\text{\AA}$  was used to filter out the long wavelength neutrons. A Cu layer with a thickness of 200 nm was deposited by radio frequency magnetron sputtering method onto a Si wafer of 1 mm in thickness and covered with 5 nm of Ti to prevent oxidation. The sputtering conditions were: generator power of 500 W, argon pressure of  $1.0 \cdot 10^{-3}$  mbar. It was supposed to install the Cu filter at the angle of  $0.8^\circ$  to the neutron beam in front of the chopper so that the neutrons with wavelength greater than 10  $\text{\AA}$  are reflected from the Cu filter and are removed from the beam while the remaining neutrons are transmitted through the filter. Fig. 3.32 shows the calculated

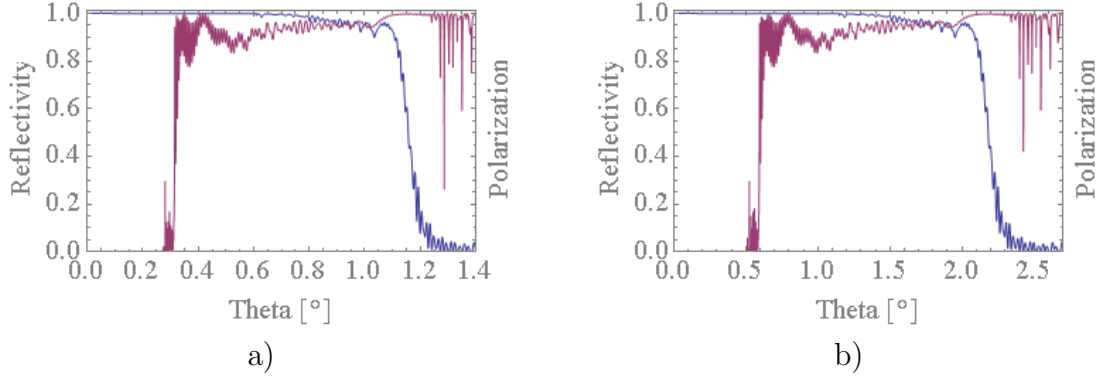


Figure 3.31: Calculated reflectivity curve (blue) for spin-up neutrons and polarization curve (red) for Fe/Si supermirror with  $m = 2$  as function of angle, neutron wavelengths: a) 5 Å and b) 10 Å.

reflectivity curve of the Cu mirror as a function of neutron wavelength for a fixed angle of  $0.8^\circ$ . Time of flight measurement of neutrons reflected from the Cu filter, fixed at  $0.88^\circ$  to the incident beam, in Fig. 3.33 a) shows the intensity in the region of 11 – 12 Å. The time of flight spectrum of neutrons transmitted through the Cu filter fixed at  $0.80^\circ$  to the incident beam is in Fig. 3.33 b). The cut of wavelength (around 10 – 12 Å) is not visible in this measurement because the neutron beam intensity is low for long wavelengths and there is contribution of the fast neutrons coming during the second neutron pulse per period (second slit on the chopper).

### 3.3.5 Supermirror Co/Ti polarizer and analyzer

Two methods have been used to obtain polarized neutrons in both of our experiments. The method of polarization via transmission of unpolarized neutrons through a polarized  $^3\text{He}$  gas is described in section 3.2. In this section we will consider polarization of neutrons via reflection from a magnetized ferromagnetic mirror. The interaction between a neutron and a medium is described by an effective potential  $V + \vec{\mu}_n \vec{B}$ , which contains nuclear ( $V = \frac{\hbar^2}{2m} 4\pi b N$ ) and magnetic ( $\vec{\mu}_n \cdot \vec{B}$ ) parts. The potential is higher for the neutrons polarized along the magnetic field ( $V + \mu_n B$ ) than for neutrons polarized against the magnetic field ( $V - \mu_n B$ ) [4]. Corresponding to the two optical potentials ( $V \pm \mu_n B$ ) for unpolarized neutrons in the magnetized ferromagnetic mirror, there will be two critical glancing angles for total reflection:

$$\theta_{cr} = \lambda \sqrt{\frac{N}{\pi} b \pm \frac{m}{2\pi^2 \hbar^2} \mu_n B}, \quad (3.15)$$

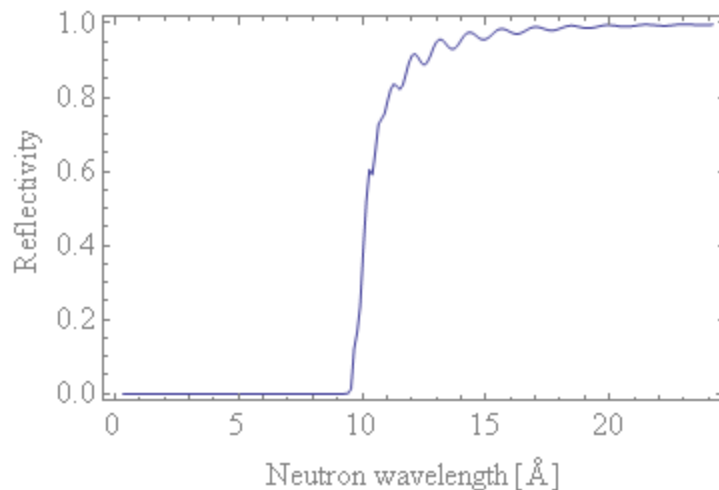


Figure 3.32: Calculated reflectivity curve of the Cu monolayer on Si wafer as a function of wavelength for fixed angle  $0.8^\circ$ .

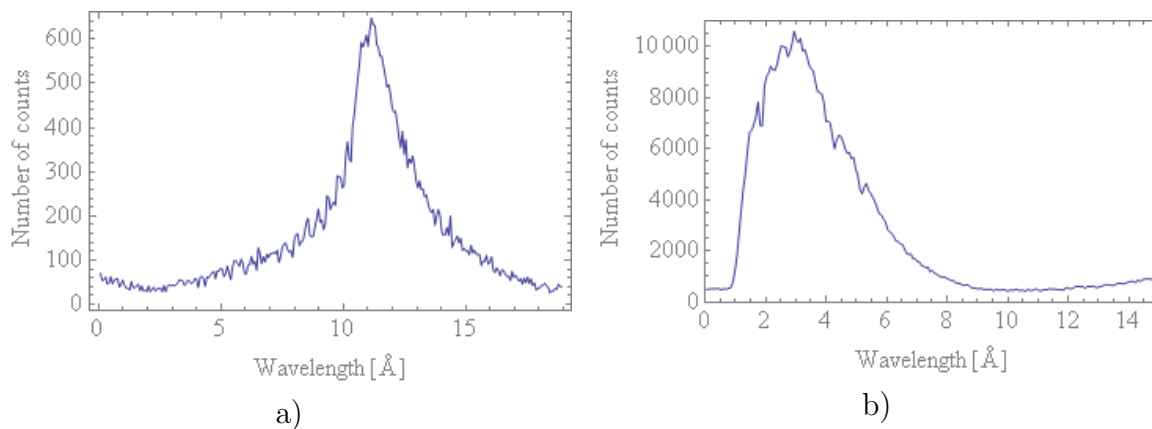


Figure 3.33: Experimental spectra obtained during the time of flight measurement of the neutrons: a) reflected from the Cu filter, placed at  $0.88^\circ$  with respect to the neutron beam; b) transmitted through the Cu filter, placed at  $0.80^\circ$  with respect to the neutron beam.

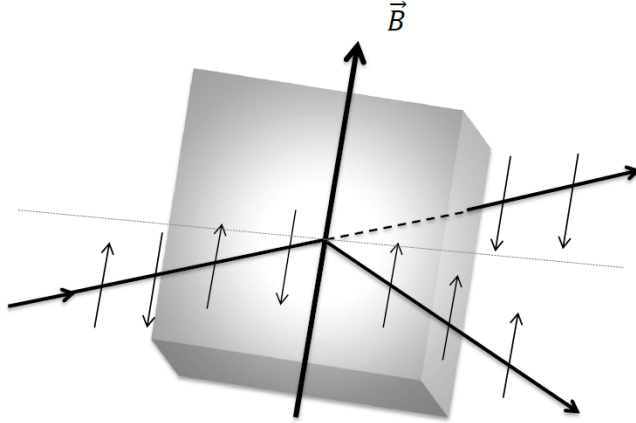


Figure 3.34: Reflection of unpolarized neutrons from a magnetized mirror.

where  $m$ ,  $\lambda$ ,  $\mu$  are the neutron mass, the wavelength and the magnetic moment.  $B$  is the magnetic induction,  $N$  is the number of atoms per unit volume in the medium and  $b$  is the coherent scattering length of a nucleus. The “+” sign in the formula 3.15 corresponds to the critical angle of neutrons polarized along the magnetic field, while the “-” sign corresponds to the critical angle of the neutrons polarized against the magnetic field. The neutron beam with a given wavelength is reflected at incident angles within the interval:

$$\lambda\sqrt{\frac{N}{\pi}b - \frac{m}{2\pi^2\hbar^2}\mu_n B} \leq \theta_{cr} \leq \lambda\sqrt{\frac{N}{\pi}b + \frac{m}{2\pi^2\hbar^2}\mu_n B} \quad (3.16)$$

and will be polarized along the external magnetic field. The transmitted beam will be polarized against the external magnetic field, see Fig. 3.34. In the figure, the magnetic induction  $\vec{B}$  is parallel to the reflecting surface. The small arrows indicate the direction of neutron spins. Reflection off magnetized cobalt and iron mirrors was studied in detail in [50]. To increase the critical angle of total reflection for the desired spin state, in polarizers are used as supermirrors. A supermirror polarizer consists of alternate layers of ferromagnetic and nonmagnetic materials that are sputtered on a substrate. The materials are chosen so that the optical potential of the ferromagnetic layer and of the nonmagnetic layer (optical potential is the same for both neutron spin states) for one spin state (the “spin-down” state) are matched. The neutrons in the “spin-down” state pass through the sequence of the layers and are absorbed in the bottom gadolinium layer. For the neutrons in the “spin-up” state (the desired state)

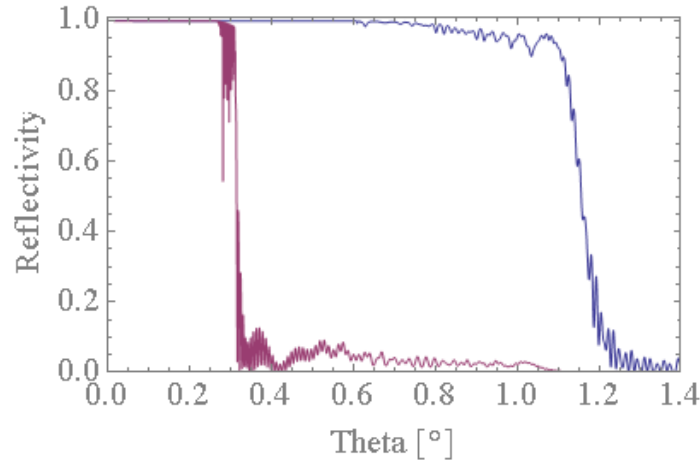


Figure 3.35: Calculated reflectivity curves for “spin-up” (blue) and “spin-down” (red) neutrons for Fe/Si polarizing supermirror with  $m=2$ .

a contrast between the optical potentials of the ferromagnetic and nonmagnetic layers is kept and these neutrons will be reflected from the magnetized supermirror surface as in a common supermirror. In Fig. 3.35 one can see an example of the calculated reflectivity curve for Fe/Si polarizing supermirror with  $m=2$ . As this figure shows, the “spin-down” critical angle  $\theta_{cr}^-$  is about one fourth of the “spin-up” critical angle  $\theta_{cr}^+$ . Between  $\theta_{cr}^-$  and  $\theta_{cr}^+$  the reflectivity curve for the “spin-up” state is close to unity but the reflectivity of the “spin-down” state is not zero. Therefore for a such distribution of Fe/Si layer thicknesses, a polarization 90% to 98% of the reflected neutrons can be achieved depending on the neutron incident angle. The first polarizing supermirror was produced by F. Mezei and P. A. Dagleish from Fe and Ag [25].

In our experiment we used a Co/Ti polarizing supermirror,  $m=2$ , developed and produced by O. Schaerpf more than twenty years ago. A system of Co/Ti bilayers of various thickness is deposited onto an absorbing anti-reflecting layer from a sequence of Gd and Ti to suppress the reflection of the wrong spin component by a substrate [38]. The neutron polarization for this supermirror is supposed to be at 98%.

The operating principle of the analyzers is the same as for the polarizers. An analyzer transmits neutrons polarized against the external magnetic field, and reflects neutrons polarized along the field. In the experiment we used Co/Ti analyzing supermirror which is identical to the polarizer.

At the beginning the polarizer and the analyzer were placed for a short time in the field of the main magnet (field strength  $190 \text{ mT}$ ) for the uniform magnetization of the layers. During the measurement the mirrors were kept in a magnetic field of  $19 \text{ mT}$  see Fig. 3.27 a).

### 3.3.6 Adiabatic spin flipper

In the experiment for reversing the neutron spin relative to the guiding magnetic field, we used the adiabatic spin flipper. A neutron passing this device slowly changes the spin direction from parallel to the guiding field at the entrance of the flipper to antiparallel at the exit. The magnetic system of the adiabatic spin flipper consists of two mutually perpendicular magnetic fields. One of them is a guiding magnetic field with a gradient, stationary in time. The other one is oscillating. A neutron spin with the magnetic moment  $\vec{\mu}_n$  precesses in the external magnetic field  $\vec{B}$  with Larmor frequency  $\omega_L = \vec{\mu}_n \vec{B} / 2\hbar$  around the direction of the magnetic field. The following consideration of the behavior of a neutron spin in the adiabatic spin flipper can be found in [51] in detail.

Fig. 3.36 a) illustrates the working principles of the adiabatic spin flipper. Polarized neutron beam ( $\vec{P} = \vec{P}_x$ ) with velocity  $v$  enters the magnetic field of the flipper from the left. The particle trajectory is parallel to the  $z$ -axis. The static guiding field has a gradient along  $z$ -axis,  $H_0(0, 0, z)$ , collinear to the  $x$ -axis, and perpendicular to it an oscillating field,  $\vec{H}_1(z, t) = H_1(z) \text{Sin}(\omega_0 t) \vec{e}_z$ , where  $\omega_0$  is the frequency and  $H_1(z)$  is the amplitude of the field. This model is called sine-cosine modulation of the effective field for the resonance spin flipping. Thus the amplitude of the oscillating field,  $H_1(z)$ , distributed along the neutron path is described by the sine function:

$$H_1(z) = A \text{sin}(\pi z / L), \quad z = [0, L], \quad (3.17)$$

where  $L$  is the length of the flipper. The coordinate dependence of the guiding field  $H_0(z)$  can be expressed by the cosine function:

$$H_0(z) = H_0 + A \text{cos}(\pi z / L), \quad (3.18)$$

where  $H_0$  is the magnitude of the field at the point  $z_0 = L/2$ , and  $A = H_0(0) - H_0(z_0)$  is the amplitude of the modulation.

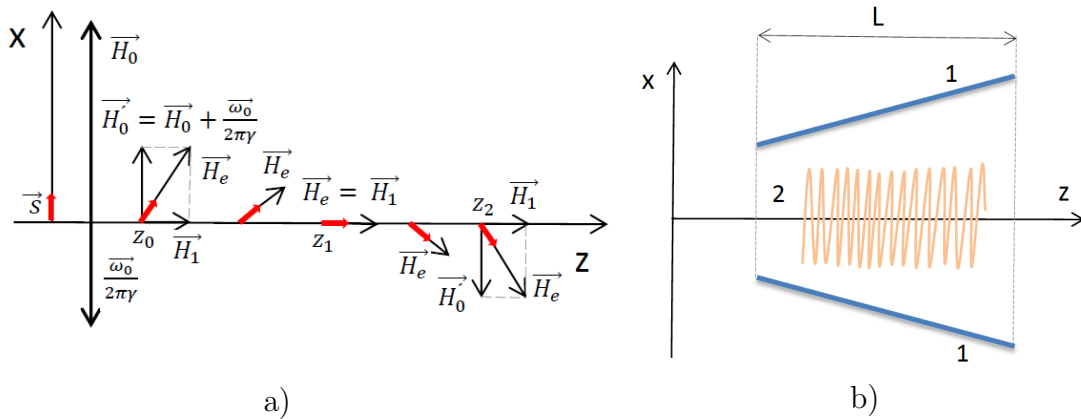


Figure 3.36: Adiabatic spin flipper: a) adiabatic spin flip in the rotating frame of the neutron; b) scheme of the standard design of the flipper.

It will be easier to imagine the motion of the neutron spin in the magnetic system of the spin flipper if we introduce the rotating frame with the same frequency  $\omega_0$  as the oscillating field around axis in direction of the static guiding field. In the rotating frame the neutron will precesses around the resulting field  $\vec{H}_{eff} = \vec{H}_0 + \vec{H}_1$  with components:

$$\vec{H}_{eff} = \{ H_0(z) - \omega_0/\gamma, 0, H_1(z) \}. \quad (3.19)$$

In Fig. 3.36 a) the red arrows indicate the direction of the effective field  $\vec{H}_{eff}$  along the flipper followed by neutron spin.

In Fig. 3.36 b) the standard design of the adiabatic spin flipper is presented. A pair of coils (1) inclined to the  $z$ -axis creates the gradient of the guiding field  $H_0(0,0,z)$  collinear to the  $x$ -axis. The solenoidal coil (2) produces the oscillating field  $H_1(z)$ . For the generation of the transverse guiding field with a gradient we used two plates from steel inclined to the  $z$ -axis with magnetic rods in between. For the generation of the oscillating longitudinal field we used the solenoidal coil, see Fig. 3.27 a). The amplitude of the RF field must be close to zero at the entrance and at the exit of the flipper, and must be maximum at the center. Therefore the density of the winding is maximum in the middle of the solenoid. The parameter  $\omega_0/2\pi$  of our flipper is  $63 \text{ kHz}$ . The modulation field  $A$  (the difference between the values of guiding field at the entrance and at the middle of the flipper) is about  $2.7 \text{ mT}$ .

The advantages of a flipper of this type are:

- the spin flip probability is close to unity for wide range of neutron spectrum

and limited only by the minimum wavelength;

- the adiabatic flipper has a high flipping stability from external influences;
- there is possibility to flip polarization of the neutron beams with the large cross section;
- there are no neutron absorbing and scattering materials along the flight pass in the flipper.

### 3.3.7 Guiding magnetic field

The neutron beam on its way from the polarizer to the analyzer must keep direction of the polarization. The adiabatic conditions for neutrons have to be fulfilled. For this purpose the change of the guiding field  $\vec{B}$  direction should be sufficiently slow. It means that the angular velocity of changing the guiding field direction has to be much smaller than frequency of precession (Larmor frequency  $\omega_L$ ) of a neutron in this guide field. In the for rotating frame, this condition is expressed as:

$$\frac{1}{|\vec{B}|} \cdot \left| \frac{d\vec{B}}{dt} \right| \ll \omega_L. \quad (3.20)$$

The magnitude of the guiding field to maintain the initial parallel or antiparallel to the external field polarization is about  $1 \text{ mT}$ . For the creation of a guiding field we used two parallel steel plates with dimensions  $300 \times 100 \times 1 \text{ mm}$  and magnetic rods in between. On all neutron way in the reflectometer must not be a zero crossing of a guiding field.

Fig. 3.37 shows the magnetic field strength at certain points on the way from the chopper to the detector. At all positions, the magnetic field is parallel to the figure surface. During measuring time the polarizer and the analyzer were placed in relatively large magnetic field of about  $18 \text{ mT}$ . The samples were magnetized in the field of the main magnet  $1.3 \text{ T}$ .

### 3.3.8 Electromagnet, sample holder

As mentioned above, the depolarization effect of a non-magnetic multilayer covering, placed in the strong magnetic field, was investigated in the reflection of polarized

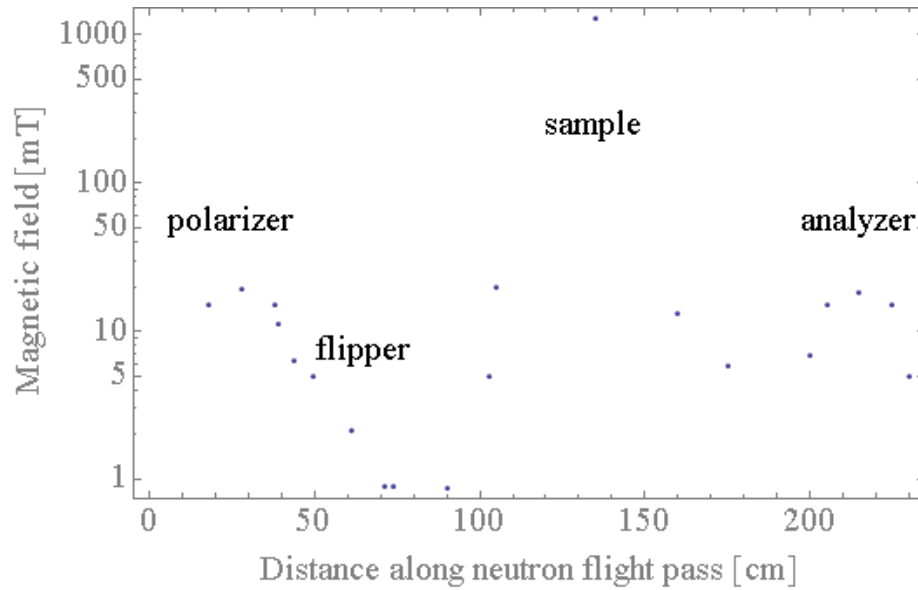


Figure 3.37: Magnetic field map of the TOF reflectometer.

neutrons from Cu/Ti and Ni(Mo)/Ti samples. Samples are plates from the float glass with size of  $200 \text{ mm} \times 40 \text{ mm} \times 10 \text{ mm}$ . The glass is covered with the studied material composition of around  $1 \mu\text{m}$  thick. The large thickness of the glass substrate prevents the sample from bending. The sample was mounted upon the sample holder via a vacuum table. The position of the sample in the neutron beam was adjusted by the two linear stages. The first linear stage regulates the linear position of the whole holder in the beam. The second linear stage linearly moves one edge of the sample relative to the other edge that is fixed. Thus changing the incident angle of the neutron beam. For position adjustment the sample was first moved linearly to the beam in order to find the center of the beam (half of the full beam intensity), and then by changing the angle of the sample (from  $0^\circ$  to a slightly more than  $\theta_{cr}$ ) to find optimal incident angle. At the beginning, the intensity of the reflected peak increases with  $\theta$  because the mirror covers more of incident neutron beam with  $\theta$  increasing. After passing  $\theta_{cr}$  the intensity of the reflected peak drops. The adjusted incident angle,  $\theta$ , was determined with precision  $0.03^\circ$  by measuring the angle  $2\theta$  between the direct polarized beam and the beam, reflected from the sample. Positions of these neutron beams were measured by the position sensitive detector. All samples were measured at  $0.75^\circ$  with respect to the incident polarized beam. Reflection of polarized

neutrons from the sample took place in the transverse magnetic field of 1.3  $T$ . The lines of the magnetic induction  $\vec{B}$  were parallel to the surface of the studied sample.

### 3.3.9 Neutron detector

A position sensitive CASCADE detector was used for neutron detection. This detector is designed for high intensity thermal and cold neutron applications. It allows the detection of high count rates, up to  $10^7 Hz/cm^2$ . The detector consists of several GEM-foils (GEM-gas electron multiplier) coated with a thin boron layer. The GEMs are stacked (“cascaded”) one behind the other, see Fig. 3.39 a).<sup>8</sup> These GEM-foils are used as charge transparent and amplify the substrate to carry a solid neutron converter, the boron layer. One of the charged fragments from neutron absorption inside the boron layer  $^{10}B(n, \alpha)^7Li$  reaches the gas volume and generates the charge which is channeled through the GEM-foils to one common readout structure. Charges are collected by electrodes corresponding to both dimensions  $x$  and  $y$ . We operated the CASCADE detector with  $200\text{ mm} \times 200\text{ mm}$  sensitive area at the ambient pressure of counting gas, see Fig. 3.39 b).<sup>9</sup> The detector consists of four layers that is covered with around  $1\ \mu m$  of boron. A voltage of 2500 V was applied. The lateral position resolution at the used pressure of the counting gas is  $(2.6 \pm 0.1\text{ mm})$ . The sensitive area is read out on 128 independent channels for each coordinate, resulting in an overall image of  $2^7 \times 2^7 = 16384$  pixel in two-dimensional-coincident correlation mode [52]. Fig. 3.39 a) shows a typical two-dimensional spectrum of CASCADE detector on a logarithmic scale. There is collimated polarized neutron beam reflected from the polarizer (channels 40-48) in the figure. Also we measured the high time of light resolution spectrum for each pixel of the readout structure, see Fig. 3.39 b). The width of the time channel varies and a multiple of 100  $ns$ .

## 3.4 Data analysis

### 3.4.1 Neutron beam divergence

The horizontal divergence of the neutron beam kept from the  $^2D$  cold neutron source by the supermirror neutron guide of the Mephisto was measured at the distance of

<sup>8</sup>Picture is taken from M. Klein, C. J. Schmidt, Nucl. Instr. and Meth.

<sup>9</sup>Picture is taken from M. Klein, C. J. Schmidt, Nucl. Instr. and Meth.

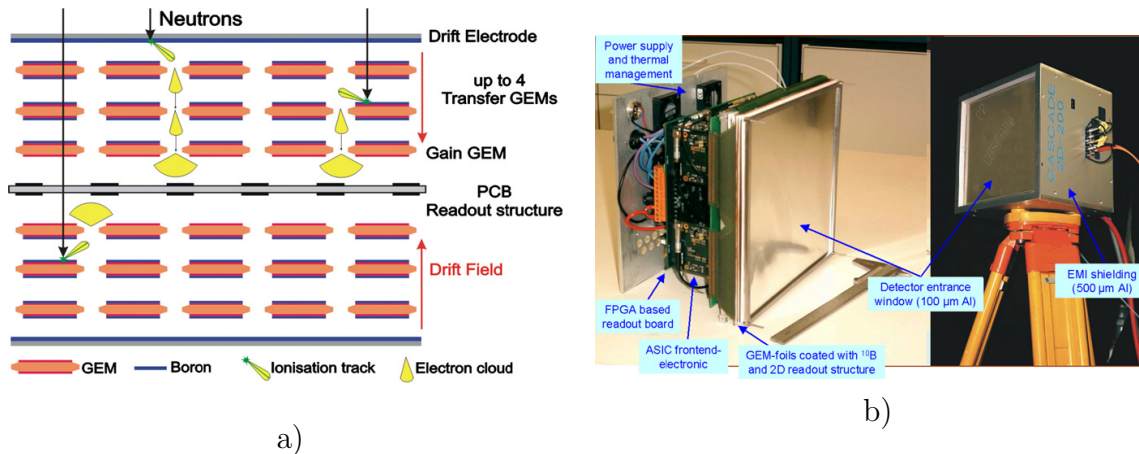


Figure 3.38: a) GEM-foils stacked one behind the other inside CASCADE detector; b) CASCADE detector of size  $200\text{ mm} \times 200\text{ mm}$ .

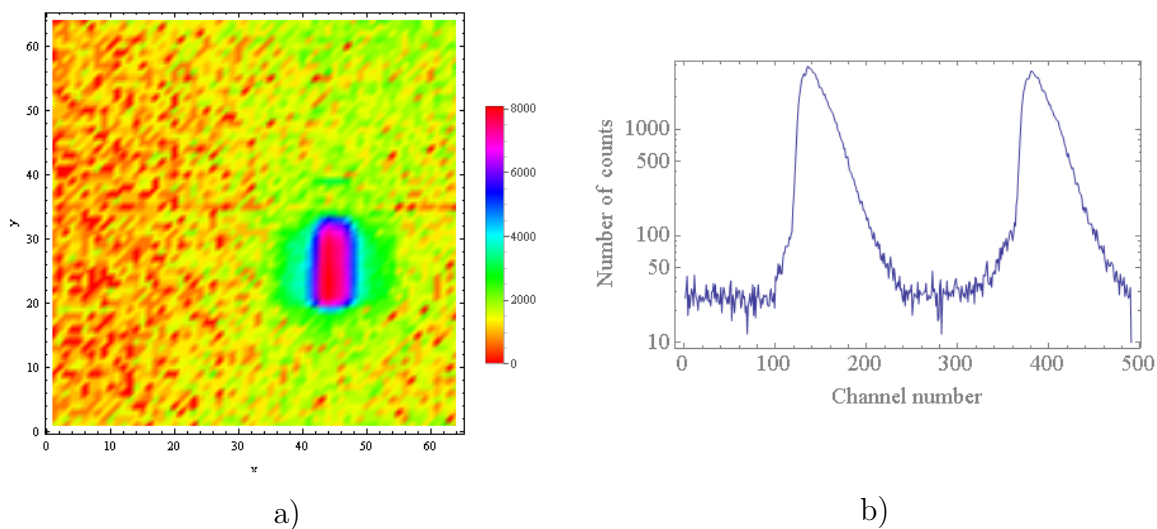


Figure 3.39: a) Two-dimensional spectrum of CASCADE detector; b) TOF spectrum of CASCADE detector.

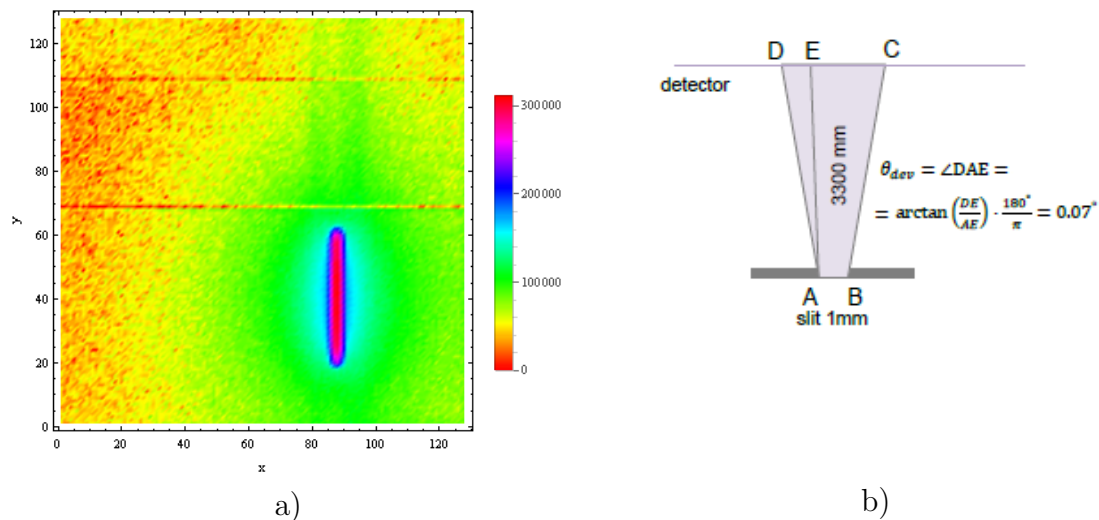


Figure 3.40: a) Two-dimensional neutron spectrum measured at the distance of the 330 cm from the slit of 1 mm wide; b) measurement scheme of the neutron beam divergence, top view.

330 cm from the vertical slit of the 1 mm wide. The two-dimensional spectrum of neutrons that passed the distance from the slit to the detector is shown in Fig. 3.40 a). The angle of the beam divergence with respect to the beam axis can be determined from the geometry, see Fig. 3.40 b), the  $\theta_{dev}$  is  $0.07^\circ$ . Due to the neutron beam divergence on the angle  $\theta_{div}$  the neutron incident angle,  $\theta_{in}$ , at the mirror fixed at the certain angle,  $\theta$ , changes within the following range  $\theta - \theta_{div} \leq \theta_{in} \leq \theta + \theta_{div}$ .

### 3.4.2 Neutron polarization

The neutron beam polarization after one reflection from the Co/Ti polarizing supermirror was measured at the reflectometer of polarized neutrons (Fig. 3.26) in a slightly different geometry. Instead of the adiabatic spin flipper and the supermirror Co/Ti analyzer, the “Magic box” (section 3.2) was used for the analysis of the neutron beam polarization. The polarizer and analyzer used in the main experiment are identical. Therefore the characteristics obtained in the measurement with the polarizer at modified reflectometer are valid for the analyzer.

The Co/Ti polarizer was magnetized in the main magnet at 190 mT and placed in the transverse magnetic field of 19 mT on the precise rotation stage. The incident angle of the neutron beam was adjusted to  $0.65^\circ$  with precision  $0.02^\circ$ . The incident angle can be checked by the position of the polarized beam reflected from the polarizer.

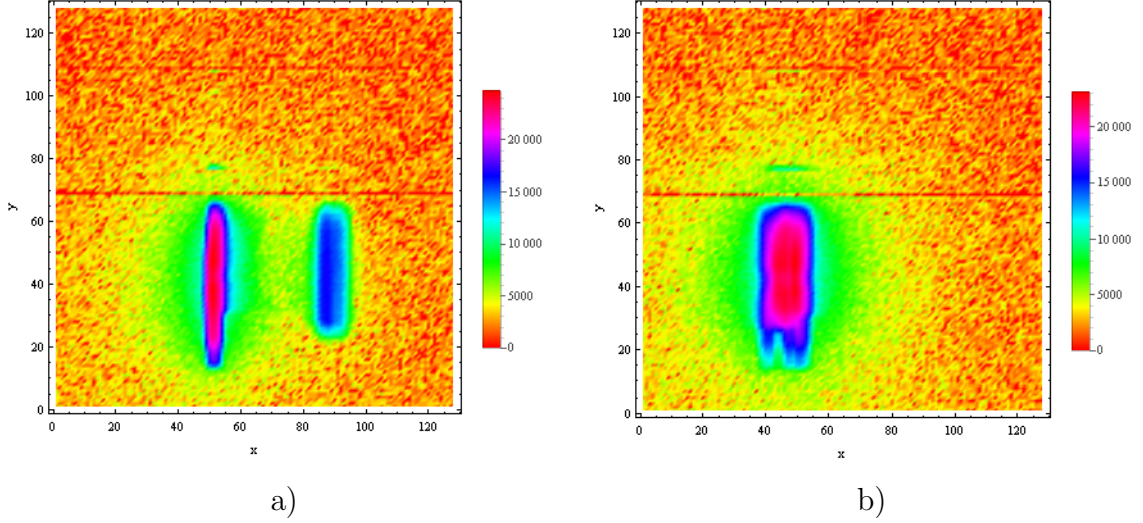


Figure 3.41: Two-dimensional spectra, obtained in the polarization measurement: a) with Co/Ti polarizer, channels 48 – 54 - part of the direct nonpolarized neutron beam and channel 86 - polarized beam; b) channel 46 - full direct beam.

The doubled incident angle  $2\theta_p$  is:

$$2\theta_p = \arctan(D_{dp}/L_{pd}) \cdot \frac{180^\circ}{\pi}, \quad (3.21)$$

were  $D_{dp}$  is the distance between the polarized and the direct neutron beam on the two-dimensional spectrum, and  $L_{pd}$  is the distance between the polarizer and the detector at the beam station. On Fig. 3.41 a) one can see part of the direct beam ( $x$  channels 48 – 54) and the polarized beam with center on the channel 86. The full nonpolarized direct beam is shown in Fig. 3.41 b). The center of the beam is at channel 46. By knowing  $D_{dp} = (86 - 46) \times 0.156 \text{ cm} = 6.24 \text{ cm}$  and  $L_{pd} = 272 \text{ cm}$  we can find  $\theta_p = 0.66^\circ$ . The number of neutrons polarized along the external magnetic field and reflected from the polarizing mirror,  $N_+$ , were registered during the “flipper off” mode. The neutrons polarized opposite to the external magnetic field but also reflected from the polarizing mirror,  $N_-$ , were registered during the “flipper on” mode. The TOF spectra of neutrons in the “spin up” and “spin down” states are presented in Fig. 3.42 a). The experimental neutron beam polarization is defined by:

$$P = \frac{(N_+ - N_+^{bgr}) - (N_- - N_-^{bgr})}{(N_+ - N_+^{bgr}) + (N_- - N_-^{bgr})}. \quad (3.22)$$

The number of the background neutrons  $N_+^{bgr}$  and  $N_-^{bgr}$  were extracted from the region of the time channels 40 – 90 of the TOF spectra. This is the time interval

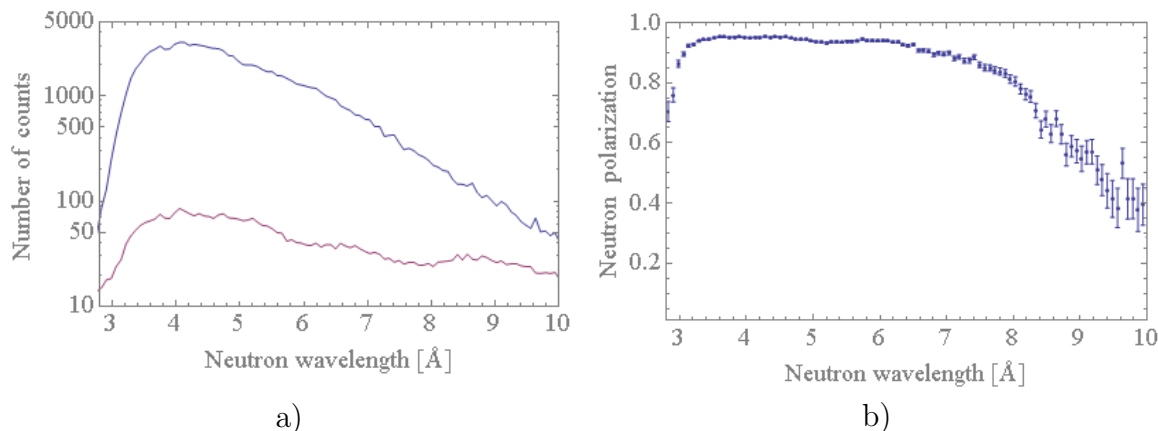


Figure 3.42: a) TOF spectra of the “spin up” (blue) and the “spin down” (red) neutrons reflected from the Co/Ti polarizer; b) the experimental polarization of neutrons obtained with the Co/Ti polarizer.

when the second neutron pulse from the chopper interrupted, and the first chopper pulse did not come. The number of counts in this region is determined only by background neutrons. The simultaneous measurement of the effect with background allows us to avoid the influence of the neutron beam fluctuations, the instability of the experimental equipment onto the measurement. The experimental polarization obtained using Eq. 3.22 depending on the neutron wavelength is shown in Fig. 3.42 b). The given errors include the statistical uncertainty of the measurements.

### 3.4.3 Neutron polarization of the direct beam

The polarization of the neutrons passed the reflectometer of the polarized neutron (Fig. 3.26) without reflection from the investigated sample (the direct beam polarization) was measured two times, on June 4 and June 8 (“direct beam polarization 04.06.13” and “direct beam polarization 08.06.13”). The neutron incident angles of the Co/Ti polarizer and analyzer were adjusted to  $0.75^\circ \pm 0.02^\circ$ . Figure 3.43 a) shows the two-dimensional spectrum of the neutrons reflected from the analyzer (37–39 channels) and the polarized neutrons that passed above the analyzer (45–48 channels). The neutron incident angle on the polarizer can be determined from this two-dimensional picture using formula 3.21. The distance  $D_{dp}$  between the polarized and the direct neutron beam on the two-dimensional spectrum with  $64 \times 64$  pixel is 7.19 cm, the distance between the polarizer and the detector is  $L_{pd} = 272$  cm. So the

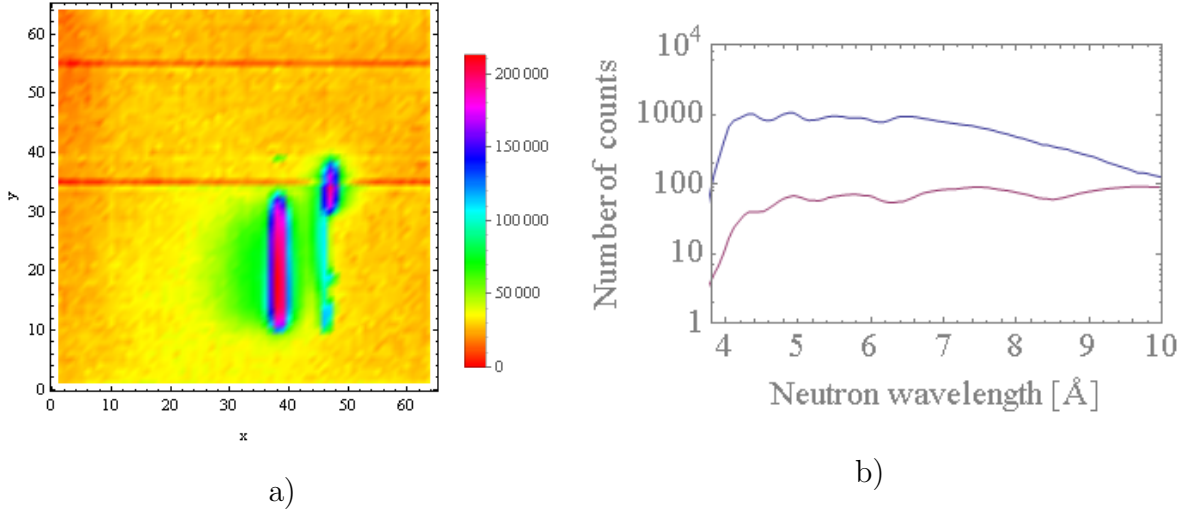


Figure 3.43: a) Two-dimensional spectrum, obtained in the polarization measurement of the direct beam on June 4 with the Co/Ti polarizer and analyzer : horizontal channels (45 – 48) - the part of the collimated polarized neutron beam, which has passed above the analyzing mirror, channels (37 – 39) - the neutron beam reflected from the analyzer; b) TOF spectra of the “spin up” (blue) and the “spin down” (red) neutrons reflected from the Co/Ti analyzer.

polarizer incident angle is  $\theta_p = 0.76^\circ$ . During all measurements, the polarizer position was not changed. The analyzer incident angle in the “direct beam polarization 04.06.13” measurement can also be found from Fig. 3.43 a) using the formula for the doubled analyzer incident angle:

$$2\theta_a = \arctan(D_{pa}/L_{ad}) \cdot \frac{180^\circ}{\pi}, \quad (3.23)$$

were  $D_{pa}$  is the distance between the part of the polarized beam passed above the analyzer and the analyzed neutron beam on the two-dimensional spectrum,  $D_{pa} = (46.9 - 38.3) \times 0.3125 \text{ cm} = 2.69 \text{ cm}$ , and  $L_{ad} = 101 \text{ cm}$  is the distance between the analyzer and the detector at the beam station. The analyzer incident angle in the “direct beam polarization 04.06.13” measurement is  $0.76^\circ$ . The analyzer incident angle in the “direct beam polarization 08.06.13” measurement was found in a similar way: it is  $0.77^\circ$ . The TOF spectra of the “spin up” and the “spin down” neutrons obtained in the measurement of the direct beam polarization on June 4 are shown in Fig. 3.43 b).

The experimental polarizations of the both measurements obtained with Eq. 3.22 are presented in the Fig. 3.44 a). The number of  $N_+$  and  $N_-$  were extracted from

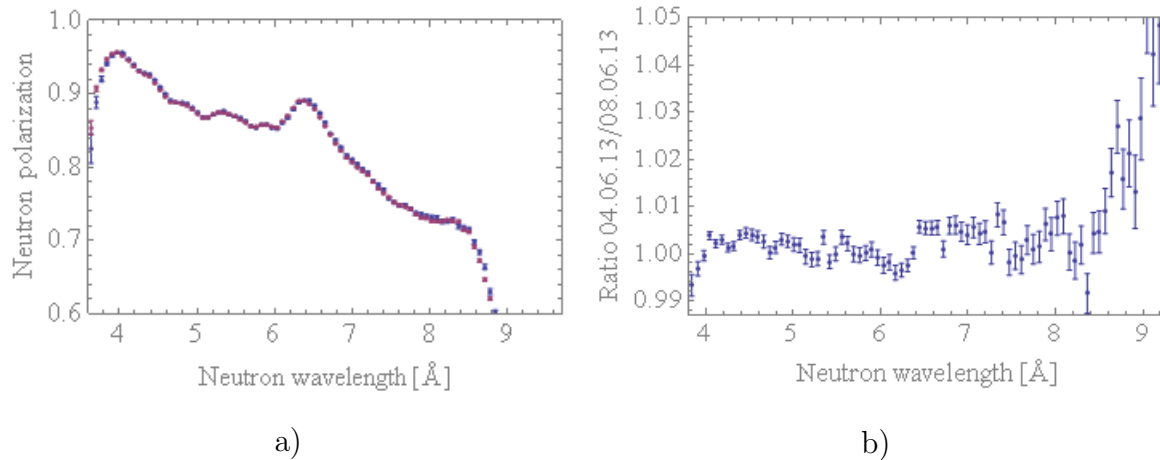


Figure 3.44: a) The experimental polarization of the direct beam: blue - measurement taken on 04.06.2013, red - measurement taken on 08.06.2013; b) the ratio between the two direct beam measurements.

the region of the horizontal channels 37 – 39 and from the region of the vertical channels 14 – 25 (Fig. 3.43 a)). The given statistical errors of the polarizations are on the level  $7 \cdot 10^{-4} - 1 \cdot 10^{-3}$ . As seen in section 3.4.1 the incident angle of neutrons at the polarizer and the analyzer varies within some range because of the angle divergence of the neutron beam. This variation of incident angles causes the polarization to change for different parts of the incident beam (polarization of the neutrons reflected from the polarizing or analyzing mirror strongly depend on the neutron incident angle and the neutron wavelength, see 3.3.5). So we observed the different polarization values for the different parts of the direct beam which passes the Co/Ti polarizer and analyzer in the direct beam measurements, see Fig. 3.45 a) and b). As it is seen from the pictures, the difference in the incident angles between of the three parts of the direct beam neutrons, is registered in various horizontal channels of the CASCADE detector expressed in the “shift” of the polarization curves. Thus in the same way each combination of the angular positions of the polarizer and the analyzer provides a unique shape of the polarization curve. For our system of the polarizer-analyzer, the change of the incident angle by  $0.07^\circ$  causes the change of the polarization of 0.1% for short wavelengths and by a few percent for long wavelengths. The ratio of the two direct beam polarization measurements (Fig. 3.44 a)) is presented in the Fig. 3.44 b). The polarization values are calculated for the neutrons from the horizontal channels 37 – 39. The ratios of the two direct beams polarization

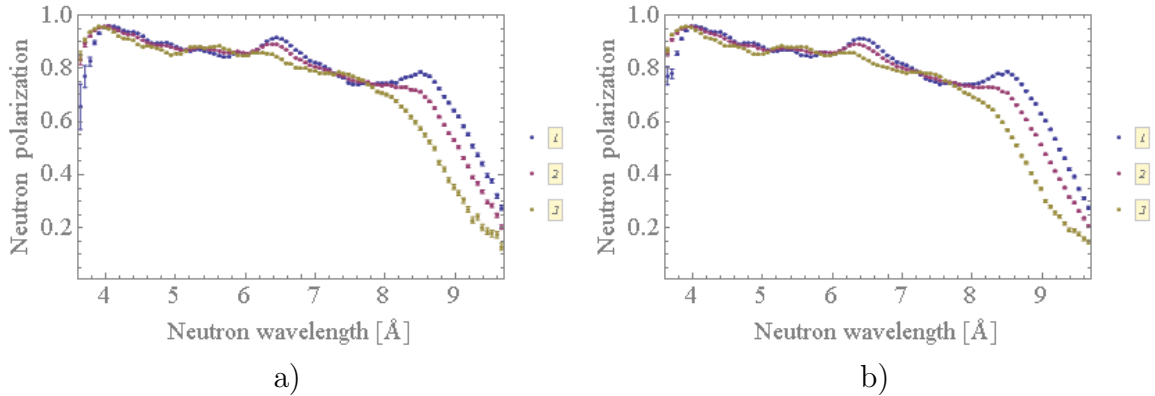


Figure 3.45: a) The experimental polarization of the direct beam, measurement taken on 04.06.2013. The polarization curves marked with “1” corresponds to the polarization of neutrons registered in the horizontal channel 37 – 38 of the two-dimensional spectrum in Fig. 3.43 a, curve “2” - for neutrons registered in the channel 38 – 39, curve “3” - for neutrons registered in the channel 39 – 40; b) the experimental polarizations for the three different parts of the direct beam (same as for direct beam measurement 04.06.13), measurement taken on 08.06.2013.

measurements for the three different parts of the direct beam are not shown here because within the statistical error they do not differ from the polarization ratios for the full channel interval. The possible reason for the deviation of the ratio between the two direct beam polarizations from unity in Fig. 3.44 b) can be the slightly different position of the analyzing mirror in the neutron beam for the two direct beam polarization measurements. The uncertainty of the angular position of the analyzing mirror ( $m = 2$ ) in  $0.02^\circ$  leads to the wavelength uncertainty of  $0.14 \text{ \AA}$  in the TOF spectrum. The length of the time channel of TOF spectrum in the wavelength is  $0.06 \text{ \AA}$ , so a shift of the polarization curve (Fig. 3.42 b) by the 1 – 2 time channels causes a change of the resulting polarization curve (Fig. 3.44 a). The regions of deviation of the two direct beam polarization ratio from unity (Fig. 3.44 b)) coincide with the regions of the largest differences between the polarization curves for the different parts, Fig. 3.45 a) and b). The influence of the such factors as the detector dead time and the background correction which could change the polarization values from measurement to measurement was not revealed.

### 3.4.4 Depolarization measurements with Cu/Ti samples

To determine the depolarization of neutrons in the reflection on the magnetized Cu/Ti multilayer samples we performed measurement on the reflectometer, Fig. 3.25, with reflection from the sample and we compared this measurement with the direct beam polarization measurement. The Cu/Ti samples with  $m = 1.55$  and  $m = 1.7$  were placed in the transverse magnetic field of  $1.3 T$ . If magnetized Cu/Ti samples do not depolarize neutrons, the polarization obtained with the polarizer “have to be transferred” by the investigated sample to the analyzer. The polarizer angle was not changed since the direct beam measurements, so it is  $\theta_p = 0.76^\circ$ , see section 3.4.3. The incidence angles of the analyzer and sample were adjusted to  $0.75^\circ \pm 0.02^\circ$  and  $0.63^\circ \pm 0.03^\circ$  respectively. We can obtain these angles from the two-dimensional picture of the neutrons that passed the reflectometer with the reflection from the sample, Fig. 3.46. The intensity in the region of the horizontal channels 45 – 47 corresponds to the polarized neutrons that passed the side of the sample without reflection from it. The intensity in the region of 33 – 36 horizontal channels corresponds to the neutrons that reflected from the sample and passed above the analyzer. The 25 – 28 channels - neutrons reflected from the analyzer. According to the formula 3.23, the analyzer incident angle,  $\theta_a$ , in measurement of the Cu/Ti samples with  $m=1.55$  and  $m=1.7$  was set to  $0.74^\circ$ . The sample incident angles can be checked in a similar manner. For both of our measurements with the Cu/Ti samples, the sample incident angles were found to be identical:  $0.60^\circ$ . As well as in the direct beam polarization measurements with the Cu/Ti samples we observed the change in the polarization values for the three different parts of the neutron beam, see Fig. 3.47. These polarization “shifts” caused by the small difference in the neutron incident angles at the polarizing (analyzing) mirrors. The polarization spectra of different parts of the neutron beam for the measurements with and without sample are shown in the Appendix H. To prevent a contribution of the neutrons with the maximum polarization variation for the analysis I used the only neutrons registered in the central channel of the beam (in the direct beam measurement x channel 38, see Fig. 3.43 a), in the measurements with Cu/Ti samples x channel 26, see Fig. 3.46 a) and b)). The Fig. 3.48 a) and b) shows TOF spectra of the “spin up” and “spin down” neutrons registered in the measurements with the Cu/Ti samples. The experimental polarizations measured with

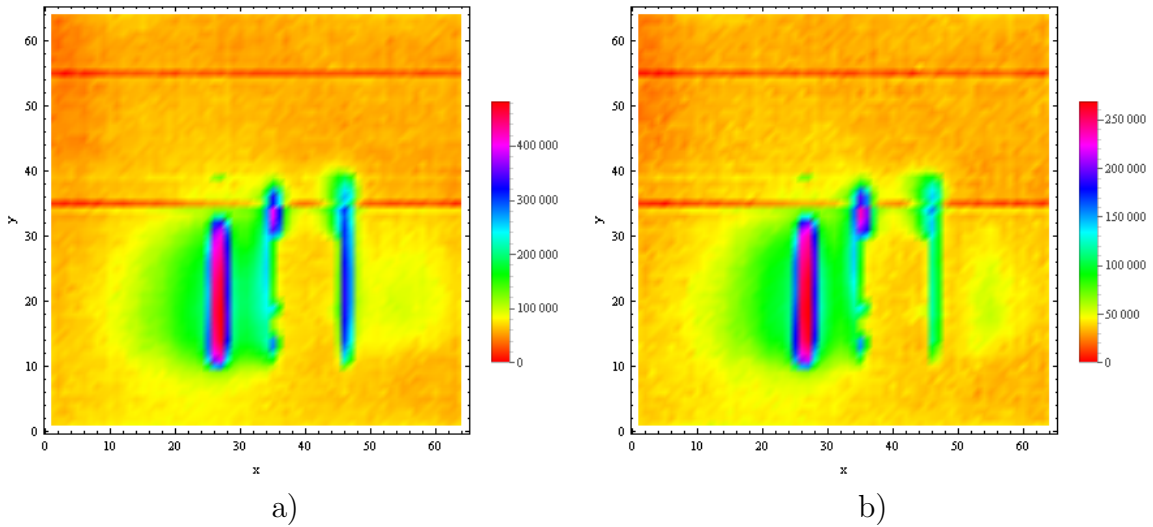


Figure 3.46: Two-dimensional spectra, obtained in the polarization measurement of the a) Cu/Ti multilayer sample with  $m = 1.55$ ; b) Cu/Ti multilayer sample with  $m = 1.7$ .

Cu/Ti samples and without sample are shown in Fig. 3.49. As one can see from the picture there is a characteristic “shift” of the polarization curves with and without a sample indicating about the difference of the analyzer angles in the measurements. The ratios between the Cu/Ti and the direct beam measurements are in Fig. 3.50.

### 3.4.5 Depolarization measurement with Ni(Mo)/Ti sample

We carried out the polarization measurement with Ni(Mo)/Ti ( $m=1.5$ ) sample. The Ni(Mo)/Ti supermirror coating is traditionally considered as non-magnetic. The sample was produced by Thorsten Lauer, Technical University of Munich.

During measurement the polarizer and the analyzer incident angles were adjusted to  $0.75^\circ \pm 0.02^\circ$ , and the sample incident angle adjusted to  $0.63^\circ \pm 0.03^\circ$ . The two-dimensional spectrum, and the TOF spectra of the “spin up” and “spin down” neutrons measured with Ni(Mo)/Ti sample are given in Fig. 3.51. The experimental polarization curves of the Ni(Mo)/Ti sample and the direct beam, and the ratio between these measurements are shown in the Fig. 3.52.

The deviation from unity of the ratios between the polarization curves obtained in the measurements with and without samples was found for all samples (see Fig. 3.53). The maximum deviations in the region of our interest, around  $5 \text{ \AA}$ , are at the level  $5 \cdot 10^{-3}$ . All “depolarization curves” display the similar behavior: the polarization

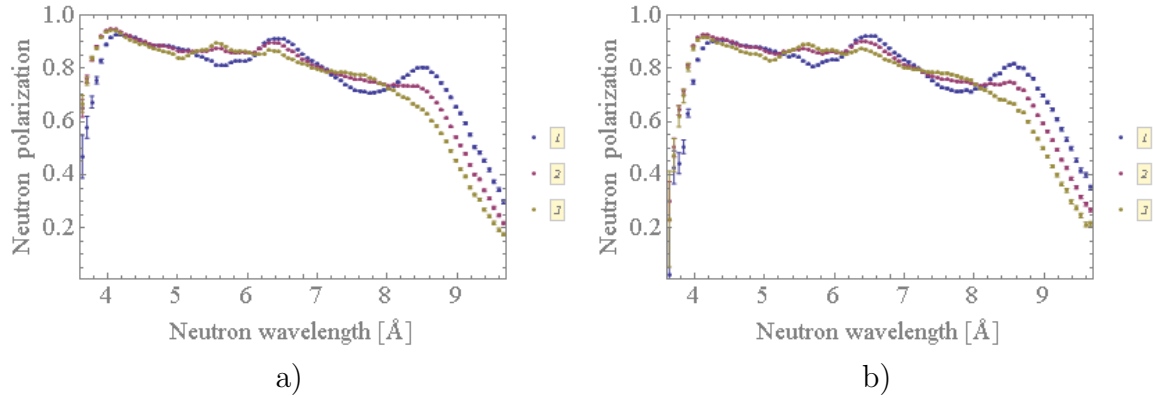


Figure 3.47: The experimental polarizations obtained with the a) Cu/Ti sample,  $m=1.55$ ; b) Cu/Ti sample,  $m=1.7$ ; The polarization curves marked with “1” corresponds to the polarization of neutrons registered in the horizontal channel 25 – 26 of the two-dimensional spectrum in Fig. 3.46, curve “2” - for neutrons registered in the channel 26 – 27, curve “3” - for neutrons registered in the channel 27 – 28.

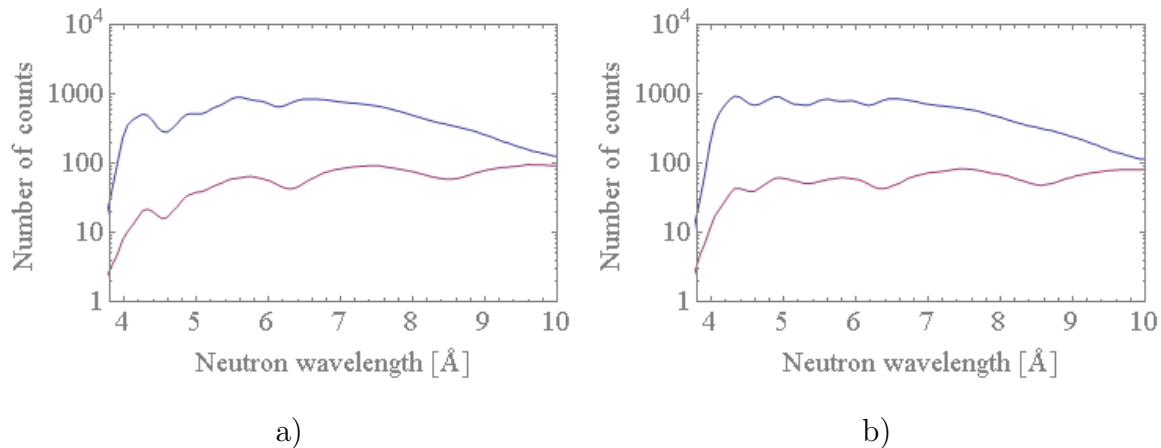


Figure 3.48: TOF spectra of the “spin up” (blue) and the “spin down” (red) neutrons passed the reflectometer with reflection from the a) Cu/Ti multilayer sample,  $m = 1.55$ ; b) Cu/Ti multilayer sample,  $m = 1.7$ .

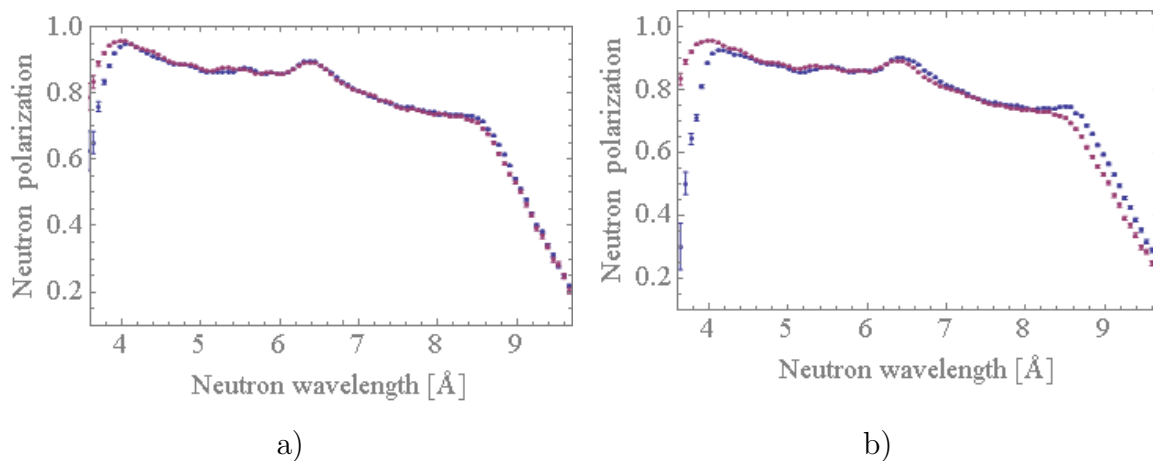


Figure 3.49: a) The experimental polarizations of the Cu/Ti sample,  $m=1.55$ , (blue) and the direct beam (red); b) the experimental polarizations of the Cu/Ti sample,  $m=1.7$ , (blue) and the direct beam (red);

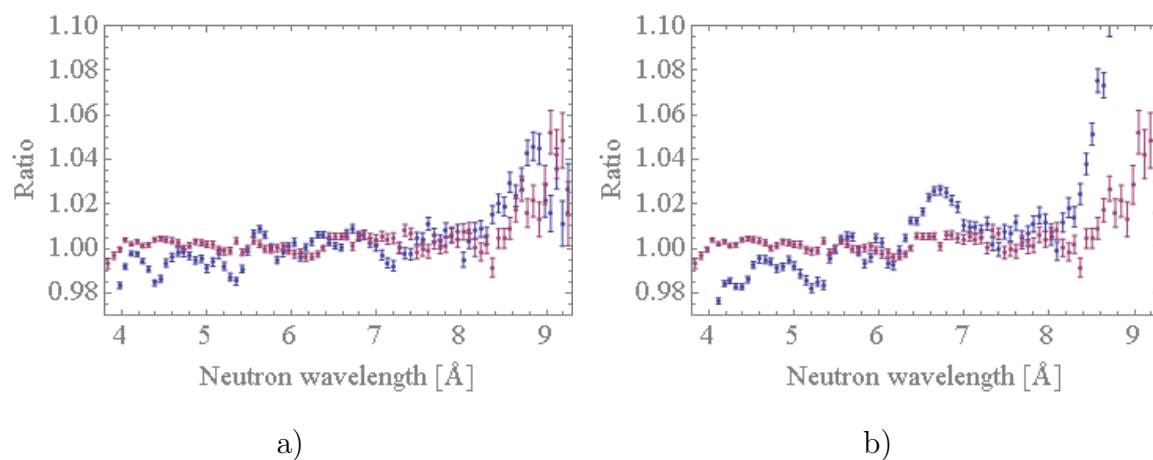


Figure 3.50: a) The ratio between the Cu/Ti sample,  $m=1.55$ , measurement and the direct beam measurement (blue), the ratio between the two direct beam measurements (red); b) the ratio between the Cu/Ti sample,  $m=1.7$ , measurement and the direct beam measurement (blue), the ratio between the two direct beam measurements (red).

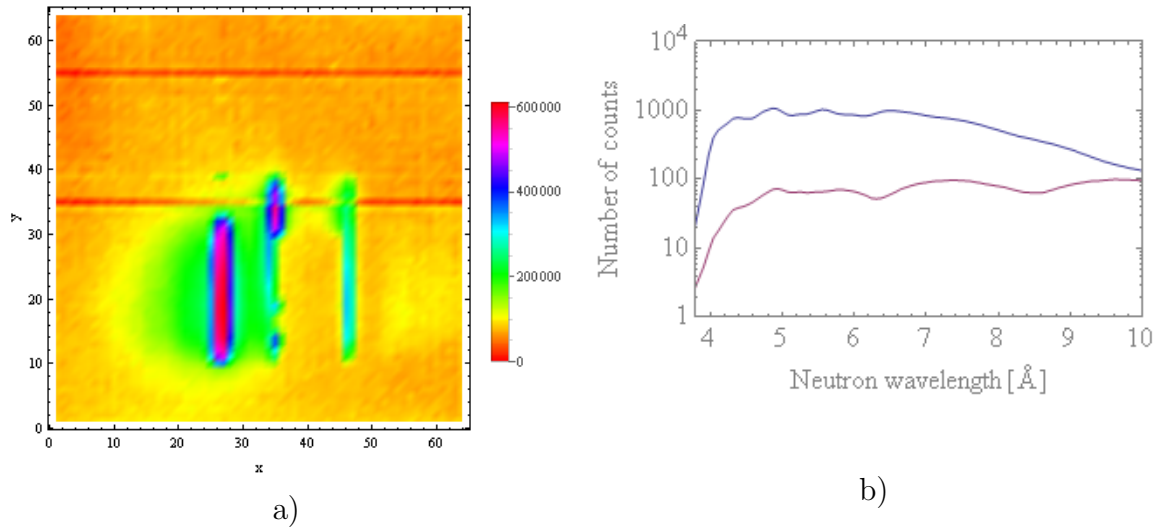


Figure 3.51: a) Two-dimensional spectrum, obtained in the polarization measurement of the Ni(Mo)/Ti sample; b) TOF spectra of the “spin up” (blue) and the “spin down” (red) neutrons passed the reflectometer with reflection from the Ni(Mo)/Ti sample.

ratio is smaller for the shortwave region and is larger (that can not be because we can not polarize neutrons by reflection from non-magnetic covering) for the long wave region. The peak positions of the “depolarization curves” match the areas where the polarizing efficiency of the polarizing mirrors strongly varies from the neutron incident angle and its wavelength, for example see Fig. 3.47. Thus the artificial neutron depolarization caused by the slightly different angular acceptance of the analyzer in the measurements with and without sample allows us to determine the depolarization in the reflection from the magnetized sample at the level  $5 \cdot 10^{-3}$ .

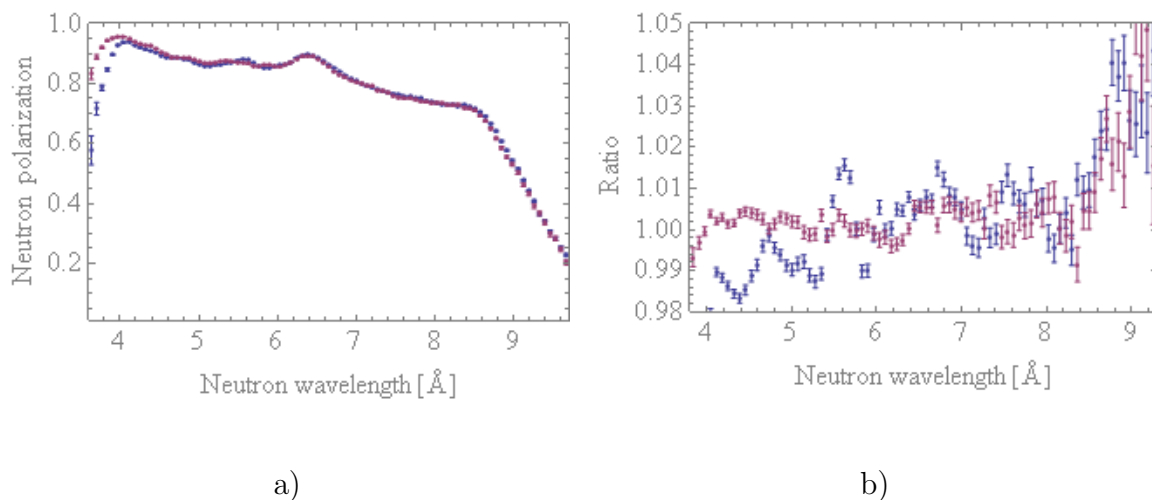


Figure 3.52: a) The experimental polarizations of the Ni(Mo)/Ti sample (blue) and the direct beam (red); b) the ratio between the Ni(Mo)/Ti sample measurement and the direct beam measurement (blue), the ratio between the two direct beam measurements (red).

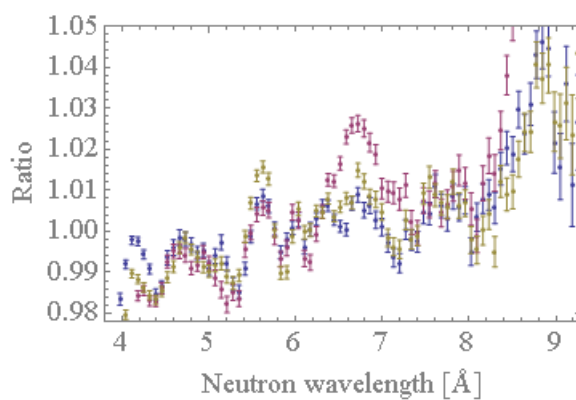


Figure 3.53: The ratios of the polarization measurement with sample and the direct beam measurement: blue - Cu/Ti,  $m=1.55$ ; red - Cu/Ti,  $m=1.7$ ; green - Ni(Mo)/Ti,  $m=1.5$ .

## Chapter 4

### Summary

Within this thesis Cu/Ti non-depolarizing supermirrors with  $m=1.2$ ,  $m=1.55$  and  $m=1.7$  has been developed and produced. The optimization algorithm for a layer sequence to get maximum reflectivity for the desired  $m$ -value has been proposed and implemented. The calculated reflectivity curves using the optimization procedure for the Cu/Ti multilayers with  $m=1.8$  (119 of Cu and Ti layers) and  $m=1.6$  (73 of Cu and Ti layers) are presented in Fig. 3.12. The reflectivity curves show high reflectivity: more than 95 % at the critical angle of the supermirrors for the extremely large roughness of layers (around 4 nm for the top layer). The optimization procedure was also applied for the Fe/Si multilayer sample with  $m=2$  (129 of Fe and Si layers). This pair of materials is the most probable candidate for the production of neutron polarizers for the PERC project. The calculated reflectivity curves for the two spin components are shown in Fig. 3.9. The reflectivity and the polarization that can be achieved with given Fe/Si layer design are also high: more than 96 %. The experimental reflectivity curves for Cu/Ti samples with  $m=1.55$  and  $m=1.7$  are shown in Fig. 3.15 a) and Fig. 3.16 a), respectively. During deposition of both samples, the thickness of all Cu layers was increased by 20 % due to the error in the calibration of the sputtering machine. This led to the decrease of the  $m$ -values (from  $m=1.6$  to  $m=1.55$  for the Cu/Ti sample with 73 layers and from  $m=1.8$  to  $m=1.7$  for the Cu/Ti sample with 119 layers) and increase of the reflectivity of the samples. Comparing the calculated and experimental reflectivity curves for Cu/Ti sample with  $m=1.7$  in Fig. 3.16 a), it is visible that  $m$ -values coincide. However reflectivity of the experimental curve is about 20 % less than calculated one for the Bragg reflection region. This can be explained by deviations from the roughness growth law layer to layer. In the development we assumed that for Cu/Ti pair, the roughness grows according to the “0.8 power law”:  $r_j = par_1 + par_2 \cdot (\frac{d_j}{d_{tot}})^{0.8}$ , where  $r_j$  is the roughness of the  $j$ th layer,  $par_1$  is the roughness of substrate,  $par_2$  is the accretion of roughness,  $d_j$  and

$d_{tot}$  are the thicknesses of the  $j$ th layer and the all layers below  $j$ th layer respectively. It is clear that to improve agreement between the calculated and experimental curves it is needed to perform more studies of Cu/Ti multilayer structures. But already now we can speak about feasibility of the supermirror reflection with Cu/Ti pair. Fe/Si samples with  $m=2$  were produced by Thorsten Laure in Munich. Measured reflectivity curves of these samples give good agreement with the calculated curves. In Heidelberg we produced the soft iron and silicon monolayers and Fe/Si multilayers with small  $m$ -value. The parameters of the sputtering machine were determined for the production of the soft iron (the magnetic field strength of 2.5 mT is required to get magnetic saturation of the soft iron layers, produced at the Heidelberg sputtering machine).

The ability to prevent neutrons from depolarizing during reflection from the Cu/Ti and Ni(Mo)/Ti multilayers placed in the strong magnetic fields, 0.8 T and 1.3 T, were investigated in Grenoble and Munich. The reflectometer of polarized neutrons in Grenoble, based on the Opaque Test Bench, provided neutron polarization analysis with precision higher than  $10^{-4}$ . The measurements were performed for the neutrons with the energy of 5.3 Å. The direct beam polarization values, the polarizations which were measured with the Cu/Ti sample ( $m=1.2$ ) at different magnetic field and the ratios between these measurements are shown in the Table 3.1 and Table 3.2. We observed no depolarization effect (with a limit below  $10^{-4}$ ) during neutron reflection from the Cu/Ti sample with  $m=1.2$  placed to the magnetic field of 0.8 T. The neutron depolarization measurements of the Cu/Ti samples with  $m=1.55$ ,  $m=1.7$  and Ni(Mo)/Ti sample with  $m=1.5$  were done in Munich at the reflectometer of polarized neutrons for the neutrons with energy from 4 Å to 8 Å. The investigated samples were placed in the magnetic field of 1.3 T. The result of this experiment, the deviation of the ratios from unity between the polarization curves obtained in the measurements with and without samples are shown in Fig. 3.53. The accuracy of this measurement was limited to  $5 \cdot 10^{-3}$  at the region of our interest, 5.3 Å, because the neutron depolarization caused by slightly different angular acceptance of the analyzer (Co/Ti supermirror) in the measurements with and without sample. The achieved accuracy in these polarization measurement of  $5 \cdot 10^{-3}$  does not satisfy the requirements of the

PERC spectrometer, so an additional depolarization test is required. Manufacturing of the alternative non-depolarizing Cu/Ti supermirror neutron guide for PERC, instead of commonly used Ni(Mo)/Ti, in a private company is an expensive and difficult task, so such decision should be made after one more depolarization test of non-magnetic coverings with a higher accuracy.

## Bibliography

- [1] D. Dubbers, H. Abele, S. Baeßler, B. Märkisch, M. Schumann, T. Soldner, O. Zimmer, Nucl. Instr. and Meth., A 596, 238, (2008).
- [2] C. Klauser, J. Chastagnier, D. Julien, A. Petoukhov and T. Soldner, Journal of Physics: Conference series 340, 012011, (2012).
- [3] W.-M. Yao et al., J. Phys. G: Nucl. Part. Phys. 33, 1, (2006).
- [4] M. Utsuro and V. K. Ignatovich (2010), Handbook of Neutron Optics, WILEY-VCH Verlag GmbH & Co. KGaA, Weinheim.
- [5] I. I. Gurevich, L. V. Tarasov, (1965), Physics of Low Energy Neutrons, Nauka, Moscow.
- [6] R. Golub, D. Richardson, S. K. Lamoreaux, (1991), Ultra-Cold Neutrons, Adam Hilger, Bristol, Philadelphia, New York.
- [7] L. D. Landau, E. M. Lifshitz, (1989), Quantum Mechanics (Nonrelativistic Theory), 4rd edn, Nauka, Moscow.
- [8] <http://physics.nist.gov/cuu/Constants/Table/allascii.txt>
- [9] V. V. Nesvizhesky, H. Börner, A. M. Gagarski, G. A. Petrov, A. K. Petukhov, H. Abele, S. Baeßler, T. Stöferle, S. M. Soloviev, Nucl. Instr. and Meth., A 440, 754, (2000).
- [10] T. Jenke, P. Geltenbort, H. Lemmel & H. Abele, Nature Physics, 7, 468, (2011).
- [11] <http://pdg.lbl.gov/2013/tables/rpp2013-tab-baryons-N.pdf>.
- [12] T. D. Lee and C. N. Yang, Phys. Rev., 104.1, 254, (1956).
- [13] C. S. Wu and E. Ambler, R. W. Hayward, D. D. Hoppes and R. P. Hudson, Phys. Rev., 105.4, 1413, (1957).
- [14] H. Abele, M. Astruc Hoffmann, S. Baeßler<sup>1</sup>, D. Dubbers, F. Glück, U. Müller, V. Nesvizhevsky, J. Reich, and O. Zimmer, Phys. Rev. Lett. 88, 211801, (2002).
- [15] M. Schumann, T. Soldner, M. Deissenroth, F. Glück, J. Krempel, M. Kreuz, B. Märkisch, D. Mund, A. Petoukhov, and H. Abele, Phys. Rev. Lett. 99, 191803, (2007).
- [16] M. Schumann, M. Kreuz, M. Deissenroth, F. Glück, J. Krempel, B. Märkisch, D. Mund, A. Petoukhov, T. Soldner and H. Abele, Phys. Rev. Lett. 100, 151801, (2008).

- [17] D. Mund, B. Märkisch, M. Deissenroth, J. Krempel, M. Schumann, A. Petoukhov, T. Soldner and H. Abele, *Phys. Rev. Lett.* 110, 172502, (2013).
- [18] F. Glück, S. Baeßler, J. Byrne, M. G. D. van der Grinten, F. J. Hartmann, W. Heil, I. Konorov, G. Petzoldt, Yu. Sobolev and O. Zimmer, *Eur. Phys. J. A* 23, 135 (2005).
- [19] E. Fermi and L. Marshall, *Phys. Rev.* 71, 666 (1947).
- [20] Neutron Data Booklet, 2nd edn, Institut Laue-Langevin, OCP Science imprint, (2003).
- [21] E. Fermi and W. H. Zinn, *Phys. Rev.*, 70, 103, (1946).
- [22] Yu. G. Abov, Neutron optics. Collection of lectures. VII School on neutron physics, (1998).
- [23] B. P. Schoenborn, D. L. D. Caspar and O. F. Kammerer, *J. Appl. Cryst.*, 7, 508, (1974).
- [24] D. Marx, *Nucl. Instr. and Meth.*, 94, 533 (1971).
- [25] F. Mezei, *Commun. Phys.* 1, 81 (1976); F. Mezei and P. A. Dagleish, *ibid.* 2 41, (1977).
- [26] O. Halpern and T. Holstein, *Phys. Rev.*, 59, 960 (1941).
- [27] S. V. Maleev and V. A. Ruban, *Sov. Phys. JETP*, 31, 111 (1970).
- [28] A. Schebetov, A. Kovalev, B. Peskov, N. Pleshanov, V. Pusenkov, P. Schubert-Bischoff, G. Shmelev, Z. Soroko, V. Syromyatnikov, V. Ul'yanov, A. Zaitsev, *Nucl. Instr. and Meth.*, A 432, 214 (1999).
- [29] N. K. Pleshanov, V. M. Pusenkov, A. F. Shebetov, B. G. Peskov, G. E. Shmelev, E. V. Siber, Z. N. Soroko, *Physica B*, 198, 27 (1994).
- [30] Stephen M. Rossnagel, *Thin Solid Films*, 171, 125 (1989).
- [31] P. J. Kelly, R. D. Arnell, *Vacuum*, 56, 159 (2000).
- [32] <http://www.arl.psu.edu>.
- [33] H. Kiessig, *Ann. Phys.*, 10, 769 (1931).
- [34] John B. Hayter and H. A. Mook, *J. Appl. Cryst.*, 22, 35 (1989).
- [35] J. Schelten and K. Mika, *Nucl. Instr. and Meth.*, 287, 35 (1979).
- [36] I. Carron, V. Ignatovich, Communication of the Joint Institute for Nuclear Research, E4-2002-264, (2002).

- [37] S. Masalovich, Nucl. Instr. and Meth., A 722, 71 (2013).
- [38] O. Schaerpf, Physica B, 156-157, 631 (1989).
- [39] A. Meschede, H. Krebs, Appl. Phys. A 102, 137 (2011).
- [40] O. Elsenhans, P. Böni, H. P. Friedli, H. Grimmer, P. Buffat, K. Leifer, J. Söchtig, I. S. Anderson, Thin Solid Films, 246, 110 (1994).
- [41] P. Böni, Physica B 234-236, 1038 (1997).
- [42] C. F. Majkrzak and J. F. Ankner, SPIE 1738, 150 (1992); C.F. Majkrzak, Physica B 213&214, 904 (1994).
- [43] B. Ballot, F. Samuel and B. Famoux, SPIE 1738, 159 (1992).
- [44] O. Elsenhans, P. Böni, H. P. Friedli, H. Grimmer, P. Buffat, K. Leifer and I. S. Anderson, SPIE 1738, 130 (1992).
- [45] C. Klauser, T. Bigault, N. Rebrova, T. Soldner, Physics Procedia, 42(2013) 99-105.
- [46] H. Abele, D. Dubbers, H. Hase, M. Klein, A. Knopfler, M. Kreuz, T. Lauer, B. Markisch, D. Mund, V. Nesvizhevsky, A. Petoukhov, C. Schmidt, M. Schumann, T. Soldner, Nucl. Instr. and Meth., A 562, 407 (2006).
- [47] W. Heil, J. Dreyer, D. Hofmann, H. Humblot, E. Lelievre-Berna, F. Tasset, Physica B 267-268 (1999) 328-335.
- [48] A. K. Petoukhov, V. Guillard, K. H. Andersen, E. Bourgeat-Lami, R. Chung, H. Humblot, D. Jullien, E. Lelievre-Berna, T. Soldner, F. Tasset, M. Thomas, Nucl. Instr. and Meth., A 560, 480 (2006).
- [49] A. Weinand, "Geschwindigkeitsmessung thermischer Neutronen am TRIGA Mainz im Rahmen des Fortgeschrittenen-Praktikums der Physik". Master thesis. Mainz University, 2011.
- [50] D. Hughes and M. Burgy, Phys. Rev., 81 (1951).
- [51] S.V. Grigoriev, V. V. Runov, A.I. Okorokov, A. D. Tretyakov, O.A. Gubin, G.P. Kopitsa, M.K. Runova, Nucl. Instr. and Meth., 384 (1997), 451.
- [52] M. Klein, C. J. Schmidt, Nucl. Instr. and Meth., A 628, 9 (2011).

## Appendix A

### Method for the reflectivity and transmittivity calculation of neutrons and x-rays passing multilayer structures.

The method for the calculation of reflectivity and transmittivity of neutrons and x-rays passing multilayer structures are described in this Appendix. The program Supermref used this method for the calculation multilayer structures. That is written following is according to an internal report by Ulrich Schmidt.

In the method a multilayer structure is represented as one-dimensional square-well potentials. The optical potential of layer  $i$  is  $P_i$ , a distance  $(x_{i+1} - x_i)$  corresponds to the thickness of the layer  $i + 1$ , Fig. A.1, the rows in the figure indicate the neutron waves (x-rays) propagating in a multilayer. The neutron (plane wave  $\psi(x) = e^{ikx}$ , where  $k$ , the  $x$ -component of wave vector  $|\vec{k}| = 2\pi/\lambda$ ) is incident from the left side of the potential. Inside the  $n$ th layer the neutron wave function  $\psi_n(x)$  satisfies the Schrödinger equation  $\{-\partial_x^2 + \frac{2m}{\hbar^2}P(x)\}\psi(x) = \frac{2m}{\hbar^2}E\psi(x) = k^2\psi(x)$  with solutions:

$$\psi_n(x) = a_n e^{ik_n x} + b_n e^{-ik_n x}, k_n = \sqrt{k^2 - \frac{2m}{\hbar^2} \text{Re}(P_n) + i \frac{2m}{\hbar^2} \text{Im}(P_n)}, \quad (\text{A.1})$$

where  $a_n$  and  $b_n$  are the amplitudes of waves going forward and backward in the  $n$ th layer. Neutron wave function and its derivative at the boundary of two potentials has to be continuous. This condition leads to the equations for determination of the amplitudes of the reflected wave from and the transmitted wave through boundary at  $x = x_n$ :

$$a_n e^{ik_n x_n} + b_n e^{-k_n x_n} = a_{n+1} e^{ik_{n+1} x_n} + b_{n+1} e^{-k_{n+1} x_n}, \quad (\text{A.2})$$

$$ik_n a_n e^{ik_n x_n} - ik_n b_n e^{-k_n x_n} = ik_{n+1} a_{n+1} e^{ik_{n+1} x_n} - ik_{n+1} b_{n+1} e^{-k_{n+1} x_n}. \quad (\text{A.3})$$

The equations for the determination of the amplitudes  $a_n$  and  $b_n$  in matrix form are:

$$\begin{pmatrix} a_n \\ b_n \end{pmatrix} = T_{n,n+1} D_n \begin{pmatrix} a_{n+1} \\ b_{n+1} \end{pmatrix}, \quad (\text{A.4})$$

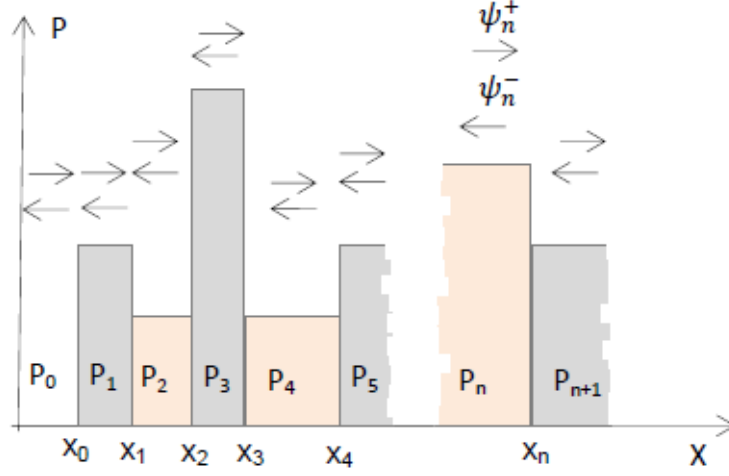


Figure A.1: Wave propagating through multilayer structure represented by one-dimensional square-well potentials.

where

$$T_{n,n+1} = \begin{pmatrix} \frac{k_n+k_{n+1}}{2k_n} & \frac{k_n-k_{n+1}}{2k_n} \\ \frac{k_n-k_{n+1}}{2k_n} & \frac{k_n+k_{n+1}}{2k_n} \end{pmatrix}, \quad D_n = \begin{pmatrix} e^{-ik_n(x_{n+1}-x_n)} & 0 \\ 0 & e^{ik_n(x_{n+1}-x_n)} \end{pmatrix}. \quad (\text{A.5})$$

Fulfilling the continuity conditions on the wave function and its derivative at all boundaries, we obtain amplitudes  $a_0$ ,  $b_0$  and expression for the reflectivity and transmittivity for a multilayer structure:

$$\begin{pmatrix} a_0 \\ b_0 \end{pmatrix} = (T_{0,1} \prod_{n=0}^{n+1} D_n T_{n,n+1}) \begin{pmatrix} 1 \\ 0 \end{pmatrix}, \quad (\text{A.6})$$

$$Ref = \frac{|b_0^2|}{|a_0^2|}, \quad Trans = \frac{1}{a_0^2} \frac{Re(k_{n+1})}{Re(k_0)}. \quad (\text{A.7})$$

The potential of interaction of neutron with matter is represented by real part,  $Pot_{re} = nb_c$  (Fermi potential), and imaginary part  $Pot_{im} = n \frac{\sigma_{abs} + \sigma_{inc}}{2\lambda_{th}}$  (absorption plus incoherent scattering), where  $n$  is the nuclei density of the layer material,  $b_n$  is the coherent scattering length,  $\sigma_{abs}$  and  $\sigma_{inc}$  are absorption and incoherent cross sections respectively,  $\lambda_{th}$  is the wavelength of thermal neutrons.

The roughness of boundaries reduces the reflectivity. The empirical factor  $e^{-k\sigma}$  was used to correct the reflectivity amplitude on roughness,  $\sigma$  is the root mean squared roughness  $\sigma = \sqrt{\frac{1}{n} \sum_{i=1}^n y_i^2}$ , where  $y_i$  is the vertical distance from the mean line of rough surface at the  $i$ th point.

It is similar for x-rays: the perpendicular component  $k$  of the wave vector inside a layer is described by expressions:

$$k^2 = k_0^2 - 4\pi Pot_{re} + i4\pi Pot_{im}, \quad (\text{A.8})$$

$$Pot_{re} = nr_e(z + fp), \quad (\text{A.9})$$

$$Pot_{im} = nr_e fpp, \quad (\text{A.10})$$

where  $n$  - the electron density of the layer material;  $z$  - the material atomic number;  $r_e = 2.818 \cdot 10^{-15}$ , classical electron radius;  $fp$  - correction for the forward scattering and  $fpp$  characterizes the absorption of x-rays.

## Appendix B

### Sputtering conditions for the Cu/Ti multilayer samples.

Table B.1: Sputtering of the Cu/Ti 5 layers sample. Thickness of the glass substrate is  $1 \cdot 10^{-3}$  m. 1) Cu layer: generator power - 500 W, working pressure  $2.7 \cdot 10^{-3}$  mbar. 2) Ti layer: generator power - 500 W, working pressure  $2.7 \cdot 10^{-3}$  mbar.

Layer number (from glass substrate)	1	2	3	4	5
Layer material	Ti	Cu	Ti	Cu	Ti
Number of rounds of the substrate-holder	4	2	4	2	4
Speed of the substrate-holder	613	563	613	563	613
Layer thickness, nm	20	20	20	20	20

Table B.2: Sputtering of the Cu/Ti 3 layers sample. Thickness of the glass substrate is  $1 \cdot 10^{-3}$  m. 1) Cu layer: generator power - 500 W, working pressure  $2.7 \cdot 10^{-3}$  mbar. 2) Ti layer: generator power - 500 W, working pressure  $2.7 \cdot 10^{-3}$  mbar.

Layer number (from glass substrate)	1	2	3
Layer material	Ti	Cu	Ti
Number of rounds of the substrate-holder	4	4	4
Speed of the substrate-holder	613	563	613
Layer thickness, nm	20	40	20

## Appendix C

The optimization procedure of the layer thicknesses.

```
(*Calculation for multilayer Cu/Ti sample (119 layers),
Ti on the top, thickness of glass substrate is 8.*10(-3) m*)
reflistCuop = Join[{{0, 0, 1. * 10(-6), rough[[1]]}},
  {{-0.98 * (1.945 * 1014), 0.98 * (1.410 * 1011), t1 + t2 * Exp[-t3 * 1], rough[[2]]}},
  {{0.99 * 6.322 * 1014, 0.99 * 9.861 * 1010, c4, rough[[3]]}},
  {{-0.98 * (1.945 * 1014), 0.98 * (1.410 * 1011), t1 + t2 * Exp[-t3 * 2], rough[[4]]}},
  {{0.99 * 6.322 * 1014, 0.99 * 9.861 * 1010, c5, rough[[5]]}},
  Flatten[Table[{{-0.98 * (1.945 * 1014), 0.98 * (1.410 * 1011),
    t1 + t2 * Exp[-t3 * i], rough[[2 * i]]}, {0.99 * 6.322 * 1014, 0.99 * 9.861 * 1010,
    c1 + c2 * Exp[-c3 * (i - 1)], rough[[2 * i + 1]]}}, {i, 2, 57, 1}], 1],
  {{-0.9813 * (1.945 * 1014), 0.9813 * (1.410 * 1011), t1 + t2 * Exp[-t3 * 119],
    rough[[119]]}}, {{3.3 * 1014, 1.1 * 1011, 8. * 10(-3), rough[[119]]}}];
ofuneCu[t1_Real, t2_Real, t3_Real, c1_Real, c2_Real, c3_Real, c4_Real, c5_Real] :=
  Sum[ref[x, reflistCuop], {x, 0.4, 0.9, 0.006}]
FindMaximum[ofuneCu[t1, t2, t3, c1, c2, c3, c4],
  {{t1, 7.77529 * 10(-9), 7.87529 * 10(-9)},
  {t2, 7.61606 * 10(-9), 7.71606 * 10(-9)}, {t3, 0.072225, 0.082225},
  {c1, 9.47174 * 10(-9), 9.57174 * 10(-9)}, {c2, 1.78335 * 10(-8), 1.88335 * 10(-8)},
  {c3, 0.113655, 0.213655}, {c4, 8.92 * (10(-8)), 9.02 * (10(-8))},
  {c5, 3.68 * (10(-8)), 3.78 * (10(-8))}}, MaxIterations → 150]
{81.5176, {t1 → 9.02616 × 10(-9), t2 → 1.14722 × 10(-8), t3 → 0.0996829, c1 → 1.32628 × 10(-9),
  c2 → 1.77948 × 10(-8), c3 → 0.0166803, c4 → 3.46377 × 10(-8), c5 → 3.02613 × 10(-8)}}
```

## Appendix D

**The optimal layer sequence to get the maximum reflectivity for the Fe/Si supermirror with  $m=2$ , 129 layers.**

Thicknesses of the Fe layers in meter, starting from the top:

{ $9.53118 \times 10^{-8}$ ,  $2.74591 \times 10^{-8}$ ,  $1.99553 \times 10^{-8}$ ,  $1.86936 \times 10^{-8}$ ,  
 $1.75635 \times 10^{-8}$ ,  $1.65512 \times 10^{-8}$ ,  $1.56444 \times 10^{-8}$ ,  $1.48321 \times 10^{-8}$ ,  $1.41045 \times 10^{-8}$ ,  
 $1.34527 \times 10^{-8}$ ,  $1.28689 \times 10^{-8}$ ,  $1.2346 \times 10^{-8}$ ,  $1.18775 \times 10^{-8}$ ,  $1.14579 \times 10^{-8}$ ,  
 $1.1082 \times 10^{-8}$ ,  $1.07453 \times 10^{-8}$ ,  $1.04437 \times 10^{-8}$ ,  $1.01736 \times 10^{-8}$ ,  $9.93159 \times 10^{-9}$ ,  
 $9.71482 \times 10^{-9}$ ,  $9.52064 \times 10^{-9}$ ,  $9.34671 \times 10^{-9}$ ,  $9.19091 \times 10^{-9}$ ,  $9.05134 \times 10^{-9}$ ,  
 $8.92633 \times 10^{-9}$ ,  $8.81435 \times 10^{-9}$ ,  $8.71404 \times 10^{-9}$ ,  $8.62418 \times 10^{-9}$ ,  $8.5437 \times 10^{-9}$ ,  
 $8.4716 \times 10^{-9}$ ,  $8.40702 \times 10^{-9}$ ,  $8.34917 \times 10^{-9}$ ,  $8.29735 \times 10^{-9}$ ,  $8.25093 \times 10^{-9}$ ,  
 $8.20935 \times 10^{-9}$ ,  $8.17211 \times 10^{-9}$ ,  $8.13874 \times 10^{-9}$ ,  $8.10886 \times 10^{-9}$ ,  $8.08209 \times 10^{-9}$ ,  
 $8.05811 \times 10^{-9}$ ,  $8.03663 \times 10^{-9}$ ,  $8.01739 \times 10^{-9}$ ,  $8.00015 \times 10^{-9}$ ,  $7.98472 \times 10^{-9}$ ,  
 $7.97089 \times 10^{-9}$ ,  $7.9585 \times 10^{-9}$ ,  $7.9474 \times 10^{-9}$ ,  $7.93746 \times 10^{-9}$ ,  $7.92856 \times 10^{-9}$ ,  
 $7.92058 \times 10^{-9}$ ,  $7.91344 \times 10^{-9}$ ,  $7.90704 \times 10^{-9}$ ,  $7.90131 \times 10^{-9}$ ,  $7.89617 \times 10^{-9}$ ,  
 $7.89157 \times 10^{-9}$ ,  $7.88745 \times 10^{-9}$ ,  $7.88376 \times 10^{-9}$ ,  $7.88046 \times 10^{-9}$ ,  $7.8775 \times 10^{-9}$ ,  
 $7.87484 \times 10^{-9}$ ,  $7.87247 \times 10^{-9}$ ,  $7.87034 \times 10^{-9}$ ,  $7.86843 \times 10^{-9}$ ,  $7.86673 \times 10^{-9}$ }

Thicknesses of the Si layers in meter, starting from the top:

{ $1.63327 \times 10^{-8}$ ,  $1.61209 \times 10^{-8}$ ,  $1.59113 \times 10^{-8}$ ,  $1.57041 \times 10^{-8}$ ,  $1.54992 \times 10^{-8}$ ,  
 $1.52965 \times 10^{-8}$ ,  $1.5096 \times 10^{-8}$ ,  $1.48978 \times 10^{-8}$ ,  $1.47017 \times 10^{-8}$ ,  $1.45077 \times 10^{-8}$ ,  
 $1.43159 \times 10^{-8}$ ,  $1.41262 \times 10^{-8}$ ,  $1.39386 \times 10^{-8}$ ,  $1.3753 \times 10^{-8}$ ,  $1.35695 \times 10^{-8}$ ,  
 $1.3388 \times 10^{-8}$ ,  $1.32085 \times 10^{-8}$ ,  $1.30309 \times 10^{-8}$ ,  $1.28553 \times 10^{-8}$ ,  $1.26817 \times 10^{-8}$ ,  
 $1.25099 \times 10^{-8}$ ,  $1.234 \times 10^{-8}$ ,  $1.2172 \times 10^{-8}$ ,  $1.20059 \times 10^{-8}$ ,  $1.18415 \times 10^{-8}$ ,  
 $1.1679 \times 10^{-8}$ ,  $1.15182 \times 10^{-8}$ ,  $1.13592 \times 10^{-8}$ ,  $1.1202 \times 10^{-8}$ ,  $1.10465 \times 10^{-8}$ ,  
 $1.08927 \times 10^{-8}$ ,  $1.07405 \times 10^{-8}$ ,  $1.05901 \times 10^{-8}$ ,  $1.04413 \times 10^{-8}$ ,  $1.02941 \times 10^{-8}$ ,  
 $1.01486 \times 10^{-8}$ ,  $1.00046 \times 10^{-8}$ ,  $9.86225 \times 10^{-9}$ ,  $9.72144 \times 10^{-9}$ ,  $9.58218 \times 10^{-9}$ ,  
 $9.44445 \times 10^{-9}$ ,  $9.30822 \times 10^{-9}$ ,  $9.1735 \times 10^{-9}$ ,  $9.04025 \times 10^{-9}$ ,  $8.90846 \times 10^{-9}$ ,  
 $8.77813 \times 10^{-9}$ ,  $8.64922 \times 10^{-9}$ ,  $8.52173 \times 10^{-9}$ ,  $8.39563 \times 10^{-9}$ ,  $8.27093 \times 10^{-9}$ ,  
 $8.14759 \times 10^{-9}$ ,  $8.0256 \times 10^{-9}$ ,  $7.90496 \times 10^{-9}$ ,  $7.78564 \times 10^{-9}$ ,  $7.66762 \times 10^{-9}$ ,  
 $7.55091 \times 10^{-9}$ ,  $7.43547 \times 10^{-9}$ ,  $7.32131 \times 10^{-9}$ ,  $7.20839 \times 10^{-9}$ ,  $7.09672 \times 10^{-9}$ ,  
 $6.98627 \times 10^{-9}$ ,  $6.87704 \times 10^{-9}$ ,  $6.769 \times 10^{-9}$ ,  $6.66215 \times 10^{-9}$ ,  $6.55647 \times 10^{-9}$ }

## Appendix E

**The optimal layer sequence to get the maximum reflectivity for the Fe/Si supermirror with  $m=2$ , 109 layers.**

Thicknesses of the Fe layers in meter, starting from the top:

{ $1.59123 \times 10^{-7}$ ,  $4.75127 \times 10^{-8}$ ,  $1.7699 \times 10^{-8}$ ,  $1.6526 \times 10^{-8}$ ,  
 $1.54931 \times 10^{-8}$ ,  $1.45836 \times 10^{-8}$ ,  $1.37828 \times 10^{-8}$ ,  $1.30776 \times 10^{-8}$ ,  $1.24568 \times 10^{-8}$ ,  
 $1.19101 \times 10^{-8}$ ,  $1.14287 \times 10^{-8}$ ,  $1.10049 \times 10^{-8}$ ,  $1.06317 \times 10^{-8}$ ,  $1.0303 \times 10^{-8}$ ,  
 $1.00137 \times 10^{-8}$ ,  $9.75892 \times 10^{-9}$ ,  $9.53458 \times 10^{-9}$ ,  $9.33705 \times 10^{-9}$ ,  $9.16313 \times 10^{-9}$ ,  
 $9.00998 \times 10^{-9}$ ,  $8.87513 \times 10^{-9}$ ,  $8.7564 \times 10^{-9}$ ,  $8.65185 \times 10^{-9}$ ,  $8.55979 \times 10^{-9}$ ,  
 $8.47874 \times 10^{-9}$ ,  $8.40736 \times 10^{-9}$ ,  $8.34452 \times 10^{-9}$ ,  $8.28919 \times 10^{-9}$ ,  $8.24046 \times 10^{-9}$ ,  
 $8.19756 \times 10^{-9}$ ,  $8.15979 \times 10^{-9}$ ,  $8.12652 \times 10^{-9}$ ,  $8.09724 \times 10^{-9}$ ,  $8.07145 \times 10^{-9}$ ,  
 $8.04874 \times 10^{-9}$ ,  $8.02875 \times 10^{-9}$ ,  $8.01114 \times 10^{-9}$ ,  $7.99564 \times 10^{-9}$ ,  $7.98199 \times 10^{-9}$ ,  
 $7.96998 \times 10^{-9}$ ,  $7.95939 \times 10^{-9}$ ,  $7.95008 \times 10^{-9}$ ,  $7.94187 \times 10^{-9}$ ,  $7.93465 \times 10^{-9}$ ,  
 $7.92829 \times 10^{-9}$ ,  $7.92268 \times 10^{-9}$ ,  $7.91775 \times 10^{-9}$ ,  $7.91341 \times 10^{-9}$ ,  $7.90959 \times 10^{-9}$ ,  
 $7.90622 \times 10^{-9}$ ,  $7.90326 \times 10^{-9}$ ,  $7.90065 \times 10^{-9}$ ,  $7.89835 \times 10^{-9}$ ,  $7.89632 \times 10^{-9}$ }

Thicknesses of the Si layers in meter, starting from the top:

$$\{1.86242 \times 10^{-8}, 1.82003 \times 10^{-8}, 1.77882 \times 10^{-8}, 1.73876 \times 10^{-8}, 1.69982 \times 10^{-8}, \\ 1.66197 \times 10^{-8}, 1.62517 \times 10^{-8}, 1.58941 \times 10^{-8}, 1.55464 \times 10^{-8}, 1.52085 \times 10^{-8}, \\ 1.48799 \times 10^{-8}, 1.45606 \times 10^{-8}, 1.42502 \times 10^{-8}, 1.39485 \times 10^{-8}, 1.36552 \times 10^{-8}, \\ 1.33701 \times 10^{-8}, 1.30929 \times 10^{-8}, 1.28235 \times 10^{-8}, 1.25617 \times 10^{-8}, 1.23071 \times 10^{-8}, \\ 1.20597 \times 10^{-8}, 1.18192 \times 10^{-8}, 1.15854 \times 10^{-8}, 1.13581 \times 10^{-8}, 1.11372 \times 10^{-8}, \\ 1.09224 \times 10^{-8}, 1.07137 \times 10^{-8}, 1.05108 \times 10^{-8}, 1.03135 \times 10^{-8}, 1.01218 \times 10^{-8}, \\ 9.93542 \times 10^{-9}, 9.75425 \times 10^{-9}, 9.57815 \times 10^{-9}, 9.40696 \times 10^{-9}, 9.24056 \times 10^{-9}, \\ 9.07881 \times 10^{-9}, 8.92158 \times 10^{-9}, 8.76874 \times 10^{-9}, 8.62017 \times 10^{-9}, 8.47576 \times 10^{-9}, \\ 8.33538 \times 10^{-9}, 8.19892 \times 10^{-9}, 8.06628 \times 10^{-9}, 7.93734 \times 10^{-9}, 7.812 \times 10^{-9}, \\ 7.69017 \times 10^{-9}, 7.57174 \times 10^{-9}, 7.45662 \times 10^{-9}, 7.34472 \times 10^{-9}, 7.23594 \times 10^{-9}, \\ 7.1302 \times 10^{-9}, 7.02742 \times 10^{-9}, 6.92751 \times 10^{-9}, 6.83039 \times 10^{-9}, 6.73599 \times 10^{-9}\}$$

## Appendix F

### Sputtering conditions for the Cu/Ti multilayer samples with $m=1.2$ .

Table F.1: Sputtering of the Cu/Ti 11 layers sample ( $m=1.2$ ). Thickness of the glass substrate is  $3 \cdot 10^{-4}$  m. 1) Cu layer: generator power - 500 W, working pressure  $2.7 \cdot 10^{-3}$  mbar. 2) Ti layer: generator power - 500 W, working pressure  $2.7 \cdot 10^{-3}$  mbar.

Layer number (from glass substrate)	Layer material	Number of rounds	Speed	Layer thickness, nm	Comments
1	Ti	2	488	12.56	
2	Cu	2	586	19.21	
3	Ti	2	464	13.22	
4	Cu	2	610	18.46	
5	Ti	2	460	13.34	
6	Cu	2	602	18.71	
7	Ti	2	476	12.87	
8	Cu	5	575	48.96	
9	Ti	2	482	12.71	
10	Cu	7	482	81.85	
11	Ti	2	499	12.29	

## Appendix G

### Sputtering conditions for the Cu/Ti multilayer samples with $m=1.8$ and $m=1.6$ .

Table G.1: Sputtering of the Cu/Ti 119 layers sample ( $m=1.7$ ). Thickness of the glass substrate is  $8 \cdot 10^{-3}$  m. 1) Cu layer: generator power - 500 W, working pressure  $1 \cdot 10^{-3}$  mbar. 2) Ti layer: generator power - 500 W, working pressure  $1 \cdot 10^{-3}$  mbar.

Layer number (from glass substrate)	Layer material	Number of rounds	Speed	Layer thickness, nm	Comments
1	Ti	2	675	7.56	
2	Cu	2	862	8.7	
3	Ti	2	672	7.59	
4	Cu	2	858	8.74	
5	Ti	2	669	7.62	
6	Cu	2	853	8.79	
7	Ti	2	667	7.65	
8	Cu	2	848	8.84	
9	Ti	2	663	7.69	
10	Cu	2	845	8.88	
11	Ti	2	661	7.72	
12	Cu	2	840	8.93	
13	Ti	2	658	7.75	
14	Cu	2	835	8.98	
15	Ti	2	656	7.78	

Layer number (from glass substrate)	Layer material	Number of rounds	Speed	Layer thickness, nm	Comments
16	Cu	2	830	9.04	
17	Ti	2	652	7.82	
18	Cu	2	825	9.09	
19	Ti	2	650	7.85	
20	Cu	2	820	9.15	
21	Ti	2	646	7.89	
22	Cu	2	815	9.2	
23	Ti	2	643	7.93	
24	Cu	2	810	9.26	
25	Ti	2	641	7.96	
26	Cu	2	805	9.32	
27	Ti	2	638	8	
28	Cu	2	799	9.39	
29	Ti	2	634	8.04	
30	Cu	2	794	9.45	
31	Ti	2	631	8.08	
32	Cu	2	787	9.52	
33	Ti	2	628	8.12	
34	Cu	2	783	9.58	
35	Ti	2	624	8.17	
36	Cu	2	776	9.66	
37	Ti	2	621	8.21	
38	Cu	2	771	9.73	
39	Ti	2	617	8.26	
40	Cu	2	765	9.81	
41	Ti	2	614	8.3	
42	Cu	2	759	9.88	
43	Ti	2	611	8.35	
44	Cu	2	752	9.97	
45	Ti	2	607	8.4	
46	Cu	2	746	10.05	
47	Ti	2	604	8.45	
48	Cu	2	740	10.14	
49	Ti	2	600	8.5	
50	Cu	2	733	10.23	
51	Ti	2	596	8.56	
52	Cu	2	727	10.32	
53	Ti	2	592	8.61	
54	Cu	2	719	10.43	
55	Ti	2	588	8.67	

Layer number (from glass substrate)	Layer material	Number of rounds	Speed	Layer thickness, nm	Comments
56	Cu	2	712	10.53	
57	Ti	2	584	8.73	
58	Cu	2	705	10.64	
59	Ti	2	580	8.79	
60	Cu	2	698	10.75	
61	Ti	2	576	8.86	
62	Cu	2	690	10.87	
63	Ti	2	571	8.93	
64	Cu	2	682	11	
65	Ti	2	567	9	
66	Cu	2	674	11.13	
67	Ti	2	562	9.07	
68	Cu	2	665	11.27	
69	Ti	2	557	9.15	
70	Cu	2	657	11.42	
71	Ti	2	553	9.23	
72	Cu	2	648	11.58	
73	Ti	2	548	9.31	
74	Cu	2	638	11.75	
75	Ti	2	543	9.4	
76	Cu	2	629	11.93	
77	Ti	2	537	9.49	
78	Cu	2	619	12.12	
79	Ti	2	532	9.58	
80	Cu	2	609	12.32	
81	Ti	2	526	9.69	
82	Cu	2	598	12.54	
83	Ti	2	521	9.79	
84	Cu	2	587	12.78	
85	Ti	2	515	9.91	
86	Cu	2	574	13.05	
87	Ti	2	508	10.03	
88	Cu	2	563	13.33	
89	Ti	2	502	10.16	
90	Cu	2	549	13.65	
91	Ti	2	495	10.3	
92	Cu	2	536	13.99	
93	Ti	2	489	10.43	
94	Cu	2	522	14.38	
95	Ti	3	721	10.61	

Layer number (from glass substrate)	Layer material	Number of rounds	Speed	Layer thickness, nm	Comments
96	Cu	2	506	14.82	
97	Ti	3	709	10.79	
98	Cu	2	489	15.33	
99	Ti	3	697	10.98	
100	Cu	2	471	15.91	
101	Ti	3	684	11.19	
102	Cu	3	678	16.59	
103	Ti	3	669	11.43	
104	Cu	3	646	17.41	
105	Ti	3	654	11.69	
106	Cu	3	611	18.42	
107	Ti	3	638	11.99	
108	Cu	3	570	19.72	
109	Ti	3	620	12.34	
110	Cu	3	524	21.45	
111	Ti	3	600	12.75	
112	Cu	3	469	23.97	
113	Ti	3	577	13.25	
114	Cu	4	534	28.08	
115	Ti	3	552	13.87	
116	Cu	5	509	36.81	
117	Ti	3	521	14.69	
118	Cu	15	631	89.16	
119	Ti	3	481	15.89	

Table G.2: Sputtering of the Cu/Ti 73 layers sample ( $m=1.55$ ). Thickness of the glass substrate is  $8 \cdot 10^{-3}$  m. 1) Cu layer: generator power - 500 W, working pressure  $1 \cdot 10^{-3}$  mbar. 2) Ti layer: generator power - 500 W, working pressure  $1 \cdot 10^{-3}$  mbar.

Layer number (from glass substrate)	Layer material	Number of rounds	Speed	Layer thickness, nm	Comments
1	Ti	2	604	8.45	
2	Cu	2	740	10.14	
3	Ti	2	600	8.5	
4	Cu	2	733	10.23	
5	Ti	2	596	8.56	
6	Cu	2	726	10.33	
7	Ti	2	592	8.61	
8	Cu	2	719	10.43	
9	Ti	2	588	8.67	
10	Cu	2	712	10.53	
11	Ti	2	584	8.73	
12	Cu	2	705	10.64	
13	Ti	2	580	8.79	
14	Cu	2	698	10.75	
15	Ti	2	576	8.86	
16	Cu	2	690	10.87	
17	Ti	2	571	8.93	
18	Cu	2	682	11	
19	Ti	2	567	9	
20	Cu	2	664	11.12	
21	Ti	2	562	9.07	
22	Cu	2	665	11.27	
23	Ti	2	557	9.15	
24	Cu	2	657	11.42	
25	Ti	2	553	9.23	
26	Cu	2	648	11.58	
27	Ti	2	548	9.31	
28	Cu	2	638	11.75	
29	Ti	2	543	9.4	
30	Cu	2	629	11.93	
31	Ti	2	537	9.49	
32	Cu	2	619	12.12	
33	Ti	2	532	9.58	
34	Cu	2	609	12.32	
35	Ti	2	526	9.69	
36	Cu	2	598	12.54	

Layer number (from glass substrate)	Layer material	Number of rounds	Speed	Layer thickness, nm	Comments
37	Ti	2	521	9.79	
38	Cu	2	586	12.78	
39	Ti	2	515	9.91	
40	Cu	2	575	13.05	
41	Ti	2	508	10.03	
42	Cu	2	563	13.33	
43	Ti	2	502	10.16	
44	Cu	2	549	13.65	
45	Ti	2	495	10.3	Ti target was not opened completely
46	Cu	2	536	13.99	
47	Ti	3	732	10.45	
48	Cu	2	522	14.38	
49	Ti	3	721	10.61	
50	Cu	2	506	14.82	
51	Ti	3	709	10.79	
52	Cu	2	489	15.33	
53	Ti	3	697	10.98	
54	Cu	3	707	15.91	
55	Ti	3	684	11.19	
56	Cu	3	678	16.59	
57	Ti	3	669	11.43	
58	Cu	3	646	17.41	
59	Ti	3	654	11.69	
60	Cu	3	611	18.42	
61	Ti	3	638	11.99	
62	Cu	3	570	19.72	
63	Ti	3	620	12.34	
64	Cu	3	524	21.45	
65	Ti	3	600	12.75	
66	Cu	4	626	23.97	
67	Ti	3	577	13.25	
68	Cu	4	534	28.09	
69	Ti	3	552	13.87	
70	Cu	5	509	36.81	
71	Ti	3	521	14.69	
72	Cu	15	631	89.16	
73	Ti	3	481	15.89	

## Appendix H

Experimental polarization spectra obtained during beam time at Mephisto station, FRM II

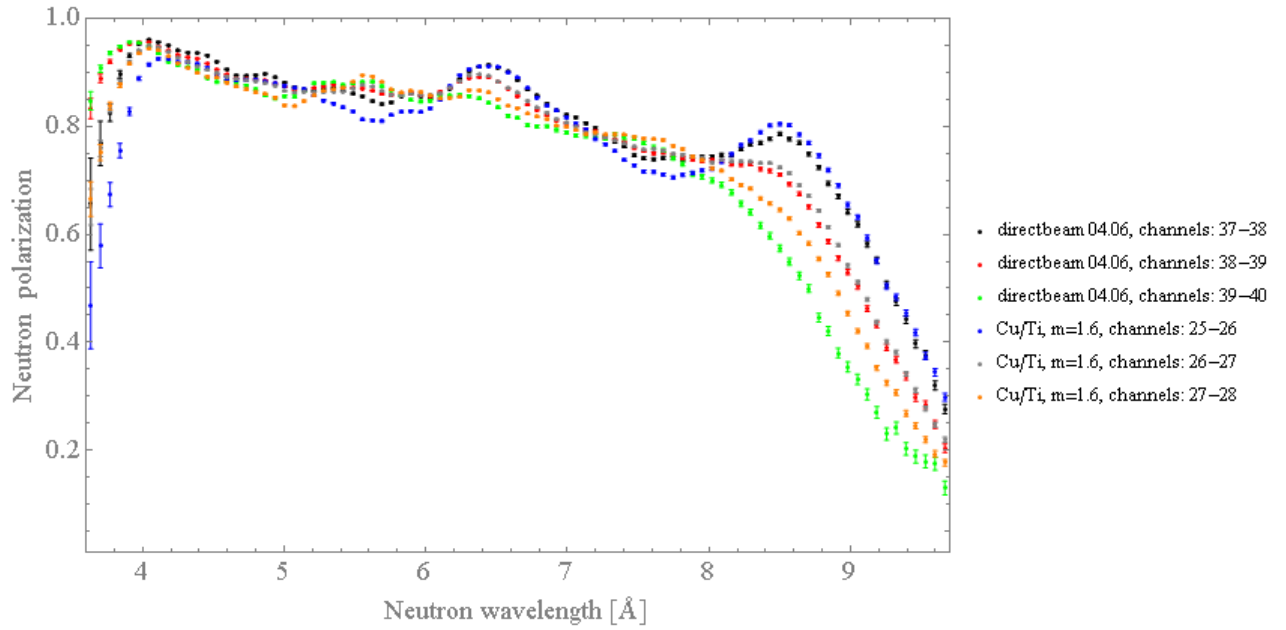


Figure H.1: Experimental polarizations of different parts of the neutron beams obtained with the direct beam on June 4 and with the Cu/Ti sample,  $m=1.55$ .

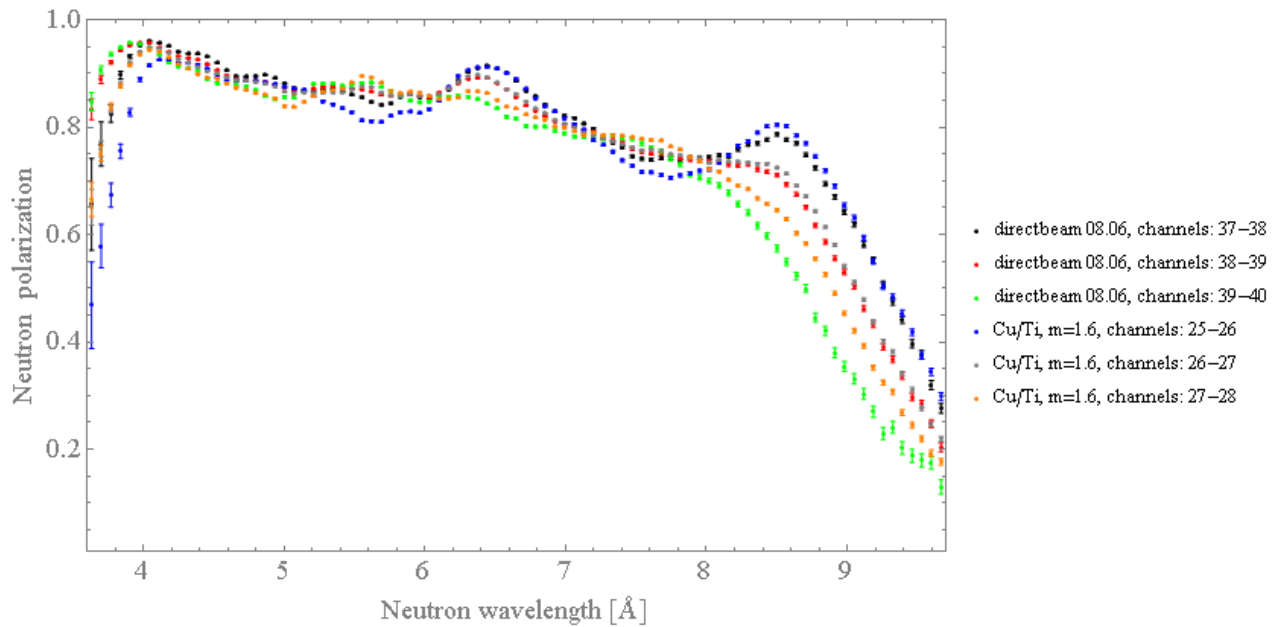


Figure H.2: Experimental polarizations of different parts of the neutron beams obtained with the direct beam on June 8 and with the Cu/Ti sample,  $m=1.55$ .

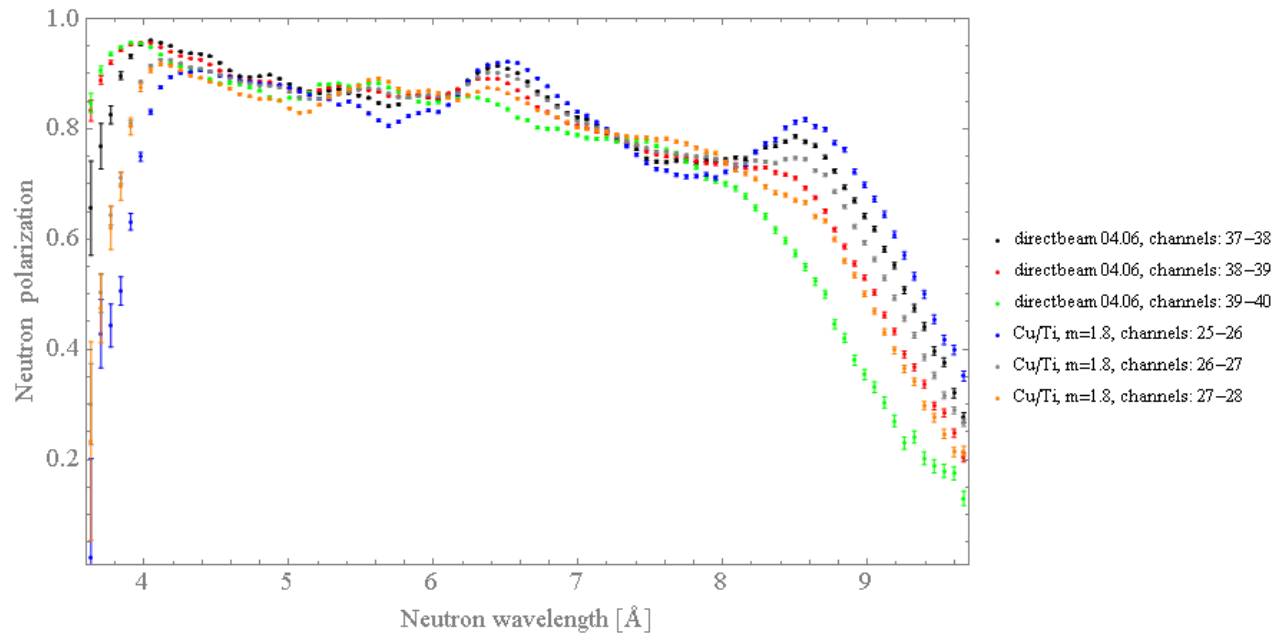


Figure H.3: Experimental polarizations of different parts of the neutron beams obtained with the direct beam on June 4 and with the Cu/Ti sample,  $m=1.7$ .

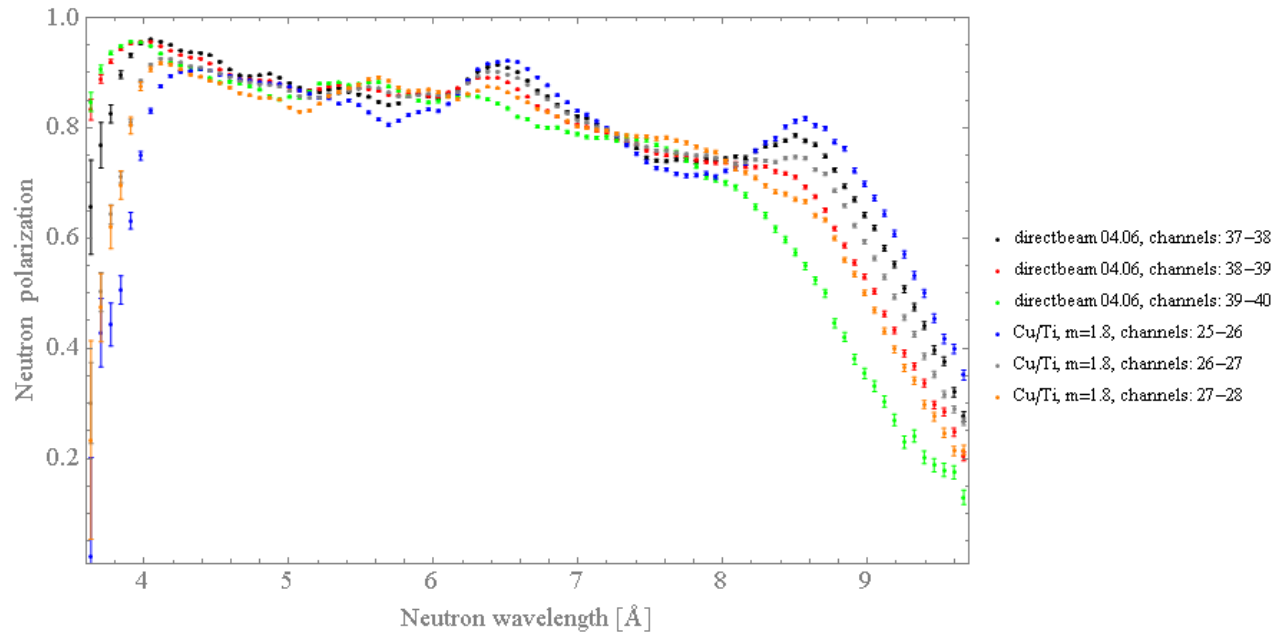
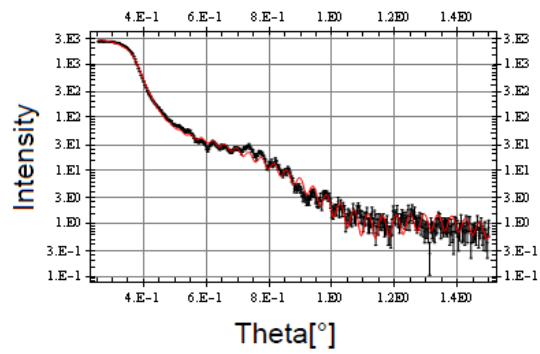


Figure H.4: Experimental polarizations of different parts of the neutron beams obtained with the direct beam on June 4 and with the Ni(Mo)/Ti,  $m=1.5$ .

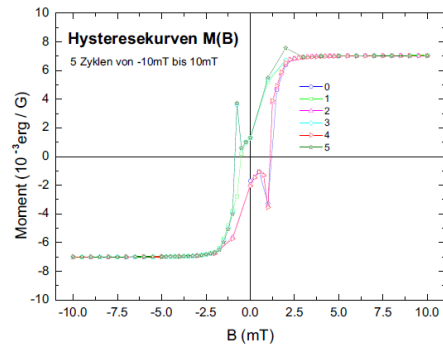
## Appendix I

### Sputtering conditions for deposition of soft iron layers

The monolayers produced from magnetically soft iron and multilayers based on soft iron and silicon can be used for polarization of slow neutrons. The soft iron is easily magnetized and demagnetized. It remains magnetized just as long as it is exposed to a magnetic field. Neutron polarization achievable with polarizers produced from soft iron is larger than for polarizers from hard iron and cobalt [45]. The soft iron monolayers with good magnetic characteristics were produced at Heidelberg University. The soft iron is obtained by the working pressure lowering in the chamber. The Fe layer was deposited at the generator power of 250  $W$ , at the working pressure of  $2.55 \cdot 10^{-3}$   $mbar$ . The top Si layers were deposited at the generator power of 500  $W$  at the working pressures of  $2.65 \cdot 10^{-3}$   $mbar$ . The Fe layers were sputtered onto Al foil which was underwent to back sputtering at the generator power of 200  $W$  and at the working pressure  $5.9 \cdot 10^{-3}$   $mbar$  during 10 minutes (the back sputtering is necessarily otherwise the deposited covering is peeled off). The x-ray reflectivity spectrum obtained with Fe sample (the thickness of the Fe layer is 96 nm, the thickness of the top Si layer is 6 nm) and the hysteresis curve measured for this sample are presented in Fig. I.1. As one can see from the hysteresis curve, the magnetic field strength of 2.5  $mT$  is required to get magnetic saturation of the soft iron layers. The magnetic field of 20  $mT$  is needed to completely magnetize a hard iron. Presence of such “big” field on the neutron pass is undesirable, the value of the polarized guiding field is about 2  $mT$ .



a)



b)

Figure I.1: a) X-ray reflectivity spectra obtained with Fe monolayer; b) hysteresis curve for Fe monolayer.

## Acknowledgment

It is a great pleasure to thank all those people who contributed to this work. First of all I am grateful to my supervisor Ulrich Schmidt for the opportunity to work in an interesting area of neutron physics. His guidance and support helped me at all stages of the research: scientific ideas and discussions, experimental work, calculations. I thank for his experience, patience, kindness. Ulrich Schmidt is a man without whom this work would not have been performed.

I thank Bastian Märkisch, the leader of PERC, for giving me the opportunity to participate in the project. I am grateful to Norbert Herrmann for accepting to be my second referee.

I wish to thank Peter Lennert for his help in repairing the sputtering machine. I am grateful to Thorsten Lauer and Mira Krüger for assisting me in the first test of the sputtering machine and for helping me during the measurements at x-ray reflectometer in Mainz. I acknowledge the man from SD-H company who did the x-ray measurements of the Cu/Ti multilayer samples.

I appreciate Torsten Soldner and Christine Klauser for the opportunity to participate in the experiment on testing the neutron polarizers for PERC and for the first depolarization measurement of the Cu/Ti sample. I would like to thank the large group who participated in the second depolarization test of the Cu/Ti and Ni(Mo)/Ti samples at the reflectometer of polarized neutrons in Munich: Jens Klenke, Thorsten Lauer, Kathrin Lehmann, Bastian Märkisch, Heiko Saul, Ulrich Schmidt, Thorsten Zechlau.

And of course my special gratitude to the former and current members of the ANP group, who helps and supports me: Carmen Ziener, Fabian Allmendinger, Peter Augenstein, Marcus Henske, Matthias Janke, Martin Klein, Markus Köhli, Holger Mest, Gerd Modzel, Lukas Raffelt, Christoph Roick. A big thank to my husband, Alexey Lubashevskiy, and to Hiren Patel for reading of my thesis.

Thank You.